International Journal of Computational Methods
Vol. 10, No. 6 (2013) 1350037 (91 pages)
© World Scientific Publishing Company
DOI: 10.1142/S0219876213500370

World Scientific
www.worldscientific.com

THE BOUNDARY ELEMENT METHOD

SUBRATA MUKHERJEE*
Sibley School of Mechanical and Aerospace Engineering
Kimball Hall, Cornell University
Ithaca, NY 14853, USA
sm85@cornell.edu

YIJUN LIU
Department of Mechanical Engineering
University of Cincinnati
Cincinnati, OH 45221, USA

Received 15 September 2010
Accepted 25 September 2011
Published 9 April 2013

The boundary element method (BEM), along with the finite element and finite difference methods, is commonly used to carry out numerical simulations in a wide variety of subjects in science and engineering. The BEM, rooted in classical mathematics of integral equations, started becoming a useful computational tool around 50 years ago. Many researchers have worked on computational aspects of this method during this time.

This paper presents an overview of the BEM and related methods. It has three sections. The first, relatively short section, presents the governing equations for classical applications of the BEM in potential theory, linear elasticity and acoustics. The second describes specialized applications in bodies with thin features including micro-electro-mechanical systems (MEMS). The final section addresses current research. It has three subsections that present the boundary contour, boundary node and fast multipole methods (BCM, BNM and FMM), respectively. Several numerical examples are included in the second and third sections of this paper.

Keywords: Boundary integral equation; boundary element method; boundary contour method; boundary node method; fast multipole method; potential theory; elasticity; acoustics.

Contents

1 Introduction **3**

2 Classical Applications **3**
2.1 Potential theory 3
2.1.1 Singular integral equations 4

*Corresponding author.

2.1.2 Hypersingular boundary integral equations (HBIE) 5
2.1.3 Potential gradient on the bounding surface 5
2.2 Linear elasticity 6
2.2.1 Singular integral equations 6
2.2.2 Hypersingular integral equations 7
2.2.3 Displacement gradient on the bounding surface 8
2.2.4 Nearly singular integrals 10
2.3 Acoustics 12
2.3.1 Singular integral equations 12
2.3.2 Hypersingular integral equations 13

3 Specialized Applications **14**
3.1 Thin bodies 14
3.1.1 BIEs in infinite region containing two thin conducting beams — Sum of charges approach 15
3.1.2 BIEs in infinite region containing two thin conducting beams — Dual BIE approach 18
3.2 Micro-electro-mechanical systems 19
3.2.1 Numerical results from the sum of charges approach 20
3.2.2 Numerical results from the dual BIE approach 21

4 Recent Research **27**
4.1 Boundary contour method 27
4.1.1 Basic equations 28
4.1.2 Interpolation functions 29
4.1.3 Boundary elements 30
4.1.4 Vector potentials 33
4.1.5 Final BCM equations 34
4.1.6 Global equations and unknowns 35
4.1.7 Surface displacements, stresses and curvatures 36
4.1.8 Regularized hypersingular BIE 37
4.1.9 Regularized hypersingular BCE 38
4.1.10 Collocation of the HBCE at an irregular surface point 40
4.1.11 Displacements and stresses at internal points 40
4.1.12 Numerical results 43
4.1.13 Appendices 47
4.2 Boundary node method 51
4.2.1 Boundary and domain based meshfree methods 51
4.2.2 Boundary node method 51
4.2.3 The boundary node method with Cartesian coordinates . . . 52
4.2.4 Numerical results 63
4.2.5 Discussion 68

4.3 Fast multipole BEM 71
4.3.1 Basic ideas in the fast multipole method 71
4.3.2 Fast multipole BEM for 2D problems 73
4.3.3 Fast multipole formulation for 3D problems 79
4.3.4 Numerical examples 80

Acknowledgments **85**

References **85**

1. Introduction

The subject of this paper is the boundary element method (BEM). The BEM is, today, a well-established method for carrying out numerical simulations of initial/boundary value problems in a wide variety of subjects in science and engineering. Ten books on the subject, published during the last three decades, are referenced here [Mukherjee (1982); Brebbia *et al.* (1984); Becker (1992); Banerjee (1994); Chandra and Mukherjee (1997); París and Cañas (1997); Bonnet (1999); Mukherjee and Mukherjee (2005); Sutradhar *et al.* (2008); Liu (2009)].

This paper presents an overview of the BEM and related methods. It is divided into three main sections. The first presents classical applications of the method — in potential theory, linear elasticity and acoustics. The second presents specialized applications in bodies with thin features — primarily 2D potential theory in a region exterior to thin beams — and in micro-electro-mechanical systems (MEMS). The last section on recent research addresses three important topics related to the BEM — the boundary contour, boundary node and fast multipole methods (BCM, BNM and FMM).

2. Classical Applications

Integral equations, singular as well as hypersingular, for points inside or on the boundary of a body, for potential theory in three dimensions, are first presented in this section. This is followed by their linear elasticity counterparts. The last part of this section concerns integral equations in acoustics.

2.1. *Potential theory*

The starting point is Laplace's equation in three dimensions (3D) governing a potential function u defined for $(x_1, x_2, x_3) \in B$, where B is a bounded region (also called the body):

$$\nabla^2 u(x_1, x_2, x_3) \equiv \frac{\partial^2 u}{\partial x_1^2} + \frac{\partial^2 u}{\partial x_2^2} + \frac{\partial^2 u}{\partial x_3^2} = 0, \tag{1}$$

along with prescribed boundary conditions on the bounding surface ∂B of B.

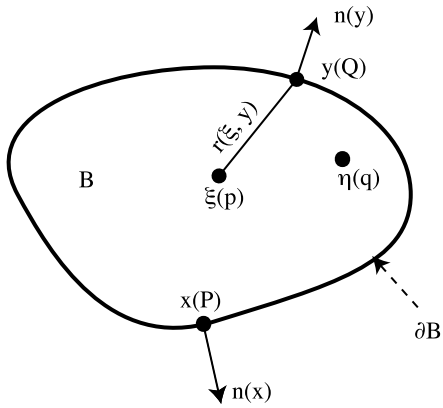

Fig. 1. Notation used in integral equations (from Mukherjee and Mukherjee [2005]).

2.1.1. *Singular integral equations*

Referring to Fig. 1, let $\boldsymbol{\xi}$ and $\boldsymbol{\eta}$ be (interior) source and field points $\in B$ and $\mathbf{x}$ and $\mathbf{y}$ be (boundary) source and field points $\in \partial B$, respectively. (Source and field points are also referred to as p and q (for interior points) and as P and Q (for boundary points), respectively, in this paper.)

The well-known integral representation for (1) at an internal point $\boldsymbol{\xi} \in B$ is:

$$u(\boldsymbol{\xi}) = \int_{\partial B} [G(\boldsymbol{\xi}, \mathbf{y})\tau(\mathbf{y}) - F(\boldsymbol{\xi}, \mathbf{y})u(\mathbf{y})]dS(\mathbf{y}). \tag{2}$$

An infinitesimal surface area on ∂B is $d\mathbf{S} = dS\mathbf{n}$, where $\mathbf{n}$ is the unit outward normal to ∂B at a point on it, and $\tau = \partial u/\partial n$. The kernels are written in terms of source and field points $\boldsymbol{\xi} \in B$ and $\mathbf{y} \in \partial B$. These are:

$$G(\boldsymbol{\xi}, \mathbf{y}) = \frac{1}{4\pi r(\boldsymbol{\xi}, \mathbf{y})}, \tag{3}$$

$$F(\boldsymbol{\xi}, \mathbf{y}) = \frac{\partial G(\boldsymbol{\xi}, \mathbf{y})}{\partial n(\mathbf{y})} = -\frac{r_{,i}(\boldsymbol{\xi}, \mathbf{y})n_i(\mathbf{y})}{4\pi r^2(\boldsymbol{\xi}, \mathbf{y})} = \frac{(\xi_i - y_i)n_i(\mathbf{y})}{4\pi r^3(\boldsymbol{\xi}, \mathbf{y})}, \tag{4}$$

in terms of $r(\boldsymbol{\xi}, \mathbf{y})$, the Euclidean distance between the source and field points $\boldsymbol{\xi}$ and $\mathbf{y}$. A comma denotes a derivative with respect to a field point, i.e.,

$$r_{,i} = \frac{\partial r}{\partial y_i} = \frac{y_i - \xi_i}{r}. \tag{5}$$

Unless specified otherwise, the range of indices in these and all other equations in this paper is $1, 2, 3$.

An alternative form of Eq. (2) is:

$$u(\boldsymbol{\xi}) = \int_{\partial B} [G(\boldsymbol{\xi}, \mathbf{y})u_{,k}(\mathbf{y}) - H_k(\boldsymbol{\xi}, \mathbf{y})u(\mathbf{y})]\mathbf{e}_k \cdot d\mathbf{S}(\mathbf{y}), \tag{6}$$

where $\mathbf{e_k}$ are the usual Cartesian unit vectors, $\mathbf{e}_k \cdot d\mathbf{S}(\mathbf{y}) = n_k(\mathbf{y})dS(\mathbf{y})$, and:

$$H_k(\boldsymbol{\xi}, \mathbf{y}) = \frac{(\xi_k - y_k)}{4\pi r^3(\boldsymbol{\xi}, \mathbf{y})}. \tag{7}$$

The boundary integral equation (BIE) corresponding to (2) is obtained by taking the limit $\boldsymbol{\xi} \to \mathbf{x}$. A regularized form of the resulting equation is [Liu and Rudolphi (1991); Liu (2009)]:

$$0 = \int_{\partial B} [G(\mathbf{x}, \mathbf{y})\tau(\mathbf{y}) - F(\mathbf{x}, \mathbf{y})\{u(\mathbf{y}) - u(\mathbf{x})\}]dS(\mathbf{y}) \tag{8}$$

with an alternate form (from (6)):

$$0 = \int_{\partial B} [G(\mathbf{x}, \mathbf{y})u_{,k}(\mathbf{y}) - H_k(\mathbf{x}, \mathbf{y})\{u(\mathbf{y}) - u(\mathbf{x})\}]\mathbf{e}_k \cdot d\mathbf{S}(\mathbf{y}). \tag{9}$$

2.1.2. *Hypersingular boundary integral equations (HBIE)*

Equation (2) can be differentiated at an internal source point $\boldsymbol{\xi}$ to obtain the gradient $\partial u/\partial \xi_m$ of the potential u. The result is:

$$\frac{\partial u(\boldsymbol{\xi})}{\partial \xi_m} = \int_{\partial B} \left[\frac{\partial G(\boldsymbol{\xi}, \mathbf{y})}{\partial \xi_m} \tau(\mathbf{y}) - \frac{\partial F(\boldsymbol{\xi}, \mathbf{y})}{\partial \xi_m} u(\mathbf{y}) \right] dS(\mathbf{y}). \tag{10}$$

An interesting situation arises when one takes the limit $\boldsymbol{\xi} \to \mathbf{x}$ ($\mathbf{x}$ can even be an irregular point on ∂B but one must have $u(\mathbf{y}) \in C^{1,\alpha}$ at $\mathbf{y} = \mathbf{x}$) in Eq. (10). As discussed in detail in Mukherjee and Mukherjee [2005], one obtains:

$$\frac{\partial u(\mathbf{x})}{\partial x_m} = \text{⨍}_{\partial B} \left[\frac{\partial G(\mathbf{x}, \mathbf{y})}{\partial x_m} \tau(\mathbf{y}) - \frac{\partial F(\mathbf{x}, \mathbf{y})}{\partial x_m} u(\mathbf{y}) \right] dS(\mathbf{y}), \tag{11}$$

where the symbol ⨍ denotes the finite part (FP) of the integral [Mukherjee (2000)]. Equation (11) must be regularized before computations are carried out. The regularized version given below is applicable even at an irregular boundary point $\mathbf{x}$ provided that $u(\mathbf{y}) \in C^{1,\alpha}$ at $\mathbf{y} = \mathbf{x}$. This is:

$$\begin{aligned} 0 = &\int_{\partial B} \frac{\partial G(\mathbf{x}, \mathbf{y})}{\partial x_m} [u_{,p}(\mathbf{y}) - u_{,p}(\mathbf{x})] n_p(\mathbf{y}) dS(\mathbf{y}) \\ &- \int_{\partial B} \frac{\partial F(\mathbf{x}, \mathbf{y})}{\partial x_m} [u(\mathbf{y}) - u(\mathbf{x}) - u_{,p}(\mathbf{x})(y_p - x_p)] dS(\mathbf{y}). \end{aligned} \tag{12}$$

2.1.3. *Potential gradient on the bounding surface*

The gradient of the potential function is required in the regularized HBIE (12). For potential problems, the gradient (at a regular boundary point) can be written as:

$$\boldsymbol{\nabla} u = \tau \mathbf{n} + \frac{\partial u}{\partial s_1} \mathbf{t}_1 + \frac{\partial u}{\partial s_2} \mathbf{t}_2, \tag{13}$$

where $\mathbf{t}_1, \mathbf{t}_2$ are the appropriately chosen unit vectors in two orthogonal tangential directions on the surface of the body, and $\partial u/\partial s_\alpha, \alpha = 1, 2$ are the tangential derivatives of u (along $\mathbf{t}_1$ and $\mathbf{t}_2$) on the surface of the body.

2.2. *Linear elasticity*

The starting point is the Navier–Cauchy equation governing the displacement $\mathbf{u}(x_1, x_2, x_3)$ in a homogeneous, compressible, isotropic, linear elastic solid occupying the bounded 3D region B with boundary ∂B; in the absence of body forces:

$$0 = u_{i,jj} + \frac{1}{1-2\nu} u_{k,ki} \tag{14}$$

along with prescribed boundary conditions that involve the displacement and the traction $\boldsymbol{\tau}$ on ∂B. The components τ_i of the traction vector are:

$$\tau_i = \lambda u_{k,k} n_i + \mu(u_{i,j} + u_{j,i}) n_j. \tag{15}$$

In Eqs. (14) and (15), ν is Poisson's ratio and λ and μ are Lamé constants. As is well known, μ is the shear modulus of the material. Finally, the Young's modulus is denoted as E.

It is noted here that the BIE also applies to exterior problems (typically in infinite domains) but only bounded domains are addressed below.

2.2.1. *Singular integral equations*

The well-known integral representation for (14), at an internal point $\boldsymbol{\xi} \in B$ [Rizzo (1967)] is:

$$u_k(\boldsymbol{\xi}) = \int_{\partial B} [U_{ik}(\boldsymbol{\xi}, \mathbf{y}) \tau_i(\mathbf{y}) - T_{ik}(\boldsymbol{\xi}, \mathbf{y}) u_i(\mathbf{y})] dS(\mathbf{y}), \tag{16}$$

where u_k and τ_k are components of the displacement and the traction respectively, and the well-known Kelvin kernels are:

$$U_{ik} = \frac{1}{16\pi(1-\nu)\mu r} [(3-4\nu)\delta_{ik} + r_{,i} r_{,k}], \tag{17}$$

$$T_{ik} = -\frac{1}{8\pi(1-\nu) r^2} \left[\{(1-2\nu)\delta_{ik} + 3 r_{,i} r_{,k}\} \frac{\partial r}{\partial n} + (1-2\nu)(r_{,i} n_k - r_{,k} n_i) \right]. \tag{18}$$

In Eqs. (17) and (18), δ_{ik} denotes the Kronecker delta and, as before, $n_i \equiv n_i(\mathbf{y})$.

An alternative form of Eq. (16) is:

$$u_k(\boldsymbol{\xi}) = \int_{\partial B} [U_{ik}(\boldsymbol{\xi}, \mathbf{y}) \sigma_{ij}(\mathbf{y}) - \Sigma_{ijk}(\boldsymbol{\xi}, \mathbf{y}) u_i(\mathbf{y})] \mathbf{e}_j \cdot d\mathbf{S}(\mathbf{y}), \tag{19}$$

where $\boldsymbol{\sigma}$ is the stress tensor defined below in Eq. (27), $\tau_i = \sigma_{ij} n_j$ and $T_{ik} = \Sigma_{ijk} n_j$. The explicit form of the kernel $\boldsymbol{\Sigma}$ is:

$$\begin{aligned} \Sigma_{ijk} &= E_{ijmn} \frac{\partial U_{km}}{\partial y_n} \\ &= -\frac{1}{8\pi(1-\nu) r^2} [(1-2\nu)(r_{,i}\delta_{jk} + r_{,j}\delta_{ik} - r_{,k}\delta_{ij}) + 3 r_{,i} r_{,j} r_{,k}], \end{aligned} \tag{20}$$

where $\mathbf{E}$ is the elasticity tensor:

$$E_{ijmn} = \lambda \delta_{ij} \delta_{mn} + \mu[\delta_{im}\delta_{jn} + \delta_{in}\delta_{jm}]. \tag{21}$$

The BIE corresponding to (16) is obtained by taking the limit $\boldsymbol{\xi} \to \mathbf{x}$. The result is:

$$u_k(\mathbf{x}) = \lim_{\boldsymbol{\xi}\to\mathbf{x}} \int_{\partial B} [U_{ik}(\boldsymbol{\xi},\mathbf{y})\tau_i(\mathbf{y}) - T_{ik}(\boldsymbol{\xi},\mathbf{y})u_i(\mathbf{y})]dS(\mathbf{y})$$

$$= \text{⨍}_{\partial B} [U_{ik}(\mathbf{x},\mathbf{y})\tau_i(\mathbf{y}) - T_{ik}(\mathbf{x},\mathbf{y})u_i(\mathbf{y})]dS(\mathbf{y}). \tag{22}$$

A regularized form of Eq. (22) is:

$$0 = \int_{\partial B} [U_{ik}(\mathbf{x},\mathbf{y})\tau_i(\mathbf{y}) - T_{ik}(\mathbf{x},\mathbf{y})\{u_i(\mathbf{y}) - u_i(\mathbf{x})\}]dS(\mathbf{y}) \tag{23}$$

with an alternate form (from (19)):

$$0 = \int_{\partial B} [U_{ik}(\mathbf{x},\mathbf{y})\sigma_{ij}(\mathbf{y}) - \Sigma_{ijk}(\mathbf{x},\mathbf{y})\{u_i(\mathbf{y}) - u_i(\mathbf{x})\}]\mathbf{e}_j \cdot d\mathbf{S}(\mathbf{y}). \tag{24}$$

2.2.2. *Hypersingular integral equations*

Equation (16) can be differentiated at an internal source point $\boldsymbol{\xi}$ to obtain the displacement gradient at this point:

$$\frac{\partial u_k(\boldsymbol{\xi})}{\partial \xi_m} = \int_{\partial B} \left[\frac{\partial U_{ik}}{\partial \xi_m}(\boldsymbol{\xi},\mathbf{y})\tau_i(\mathbf{y}) - \frac{\partial T_{ik}}{\partial \xi_m}(\boldsymbol{\xi},\mathbf{y})u_i(\mathbf{y})\right] dS(\mathbf{y}). \tag{25}$$

An alternative form of Eq. (25) is:

$$\frac{\partial u_k(\boldsymbol{\xi})}{\partial \xi_m} = \int_{\partial B} \left[\frac{\partial U_{ik}}{\partial \xi_m}(\boldsymbol{\xi},\mathbf{y})\sigma_{ij}(\mathbf{y}) - \frac{\partial \Sigma_{ijk}}{\partial \xi_m}(\boldsymbol{\xi},\mathbf{y})u_i(\mathbf{y})\right] \mathbf{e}_j \cdot d\mathbf{S}(\mathbf{y}). \tag{26}$$

Stress components at an internal point $\boldsymbol{\xi}$ can be obtained from either Eqs. (25) or (26) by using Hooke's law:

$$\sigma_{ij} = \lambda u_{k,k}\delta_{ij} + \mu(u_{i,j} + u_{j,i}). \tag{27}$$

It is sometimes convenient, however, to write stresses directly at an interior point. This equation, corresponding (for example) to (25) is:

$$\sigma_{ij}(\boldsymbol{\xi}) = \int_{\partial B} [D_{ijk}(\boldsymbol{\xi},\mathbf{y})\tau_k(\mathbf{y}) - S_{ijk}(\boldsymbol{\xi},\mathbf{y})u_k(\mathbf{y})]dS(\mathbf{y}), \tag{28}$$

where the new kernels $\mathbf{D}$ and $\mathbf{S}$ are:

$$D_{ijk} = E_{ijmn}\frac{\partial U_{km}}{\partial \xi_n} = \lambda\frac{\partial U_{km}}{\partial \xi_m}\delta_{ij} + \mu\left(\frac{\partial U_{ki}}{\partial \xi_j} + \frac{\partial U_{kj}}{\partial \xi_i}\right) = -\Sigma_{ijk}, \tag{29}$$

$$S_{ijk} = E_{ijmn}\frac{\partial \Sigma_{kpm}}{\partial \xi_n}n_p = \lambda\frac{\partial \Sigma_{kpm}}{\partial \xi_m}n_p\delta_{ij} + \mu\left(\frac{\partial \Sigma_{kpi}}{\partial \xi_j} + \frac{\partial \Sigma_{kpj}}{\partial \xi_i}\right)n_p$$

$$= \frac{G}{4\pi(1-\nu)r^3}\left[3\frac{\partial r}{\partial n}[(1-2\nu)\delta_{ij}r_{,k} + \nu(\delta_{ik}r_{,j} + \delta_{jk}r_{,i}) - 5r_{,i}r_{,j}r_{,k}]\right]$$

$$+ \frac{G}{4\pi(1-\nu)r^3}[3\nu(n_i r_{,j}r_{,k} + n_j r_{,i}r_{,k})$$

$$+ (1-2\nu)(3n_k r_{,i}r_{,j} + n_j\delta_{ik} + n_i\delta_{jk}) - (1-4\nu)n_k\delta_{ij}]. \tag{30}$$

Please note that:

$$\frac{\partial U_{ik}}{\partial \xi_m}(\boldsymbol{\xi}, \mathbf{y}) = -U_{ik,m}, \quad \frac{\partial \Sigma_{ijk}}{\partial \xi_m}(\boldsymbol{\xi}, \mathbf{y}) = -\Sigma_{ijk,m}. \tag{31}$$

It is important to note that $\mathbf{D}$ becomes strongly singular, and $\mathbf{S}$ hypersingular as a source point approaches a field point (i.e., as $r \to 0$).

It is sometimes useful to rewrite (26) using (31). This equation is:

$$u_{k,m}(\boldsymbol{\xi}) = -\int_{\partial B} [U_{ik,m}(\boldsymbol{\xi}, \mathbf{y})\sigma_{ij}(\mathbf{y}) - \Sigma_{ijk,m}(\boldsymbol{\xi}, \mathbf{y})u_i(\mathbf{y})]n_j(\mathbf{y})dS(\mathbf{y}). \tag{32}$$

Again, as one takes the limit $\boldsymbol{\xi} \to \mathbf{x}$ in any of the Eqs. (25), (26) or (28), one must take the finite part of the corresponding right hand side. For example, (26) and (28) become, respectively:

$$\begin{aligned}\frac{\partial u_k(\mathbf{x})}{\partial x_m} &= \lim_{\boldsymbol{\xi}\to\mathbf{x}} \int_{\partial B} \left[\frac{\partial U_{ik}}{\partial \xi_m}(\boldsymbol{\xi}, \mathbf{y})\sigma_{ij}(\mathbf{y}) - \frac{\partial \Sigma_{ijk}}{\partial \xi_m}(\boldsymbol{\xi}, \mathbf{y})u_i(\mathbf{y})\right] n_j(\mathbf{y})dS(\mathbf{y}) \\ &= \text{⨍}_{\partial B} \left[\frac{\partial U_{ik}}{\partial x_m}(\mathbf{x}, \mathbf{y})\sigma_{ij}(\mathbf{y}) - \frac{\partial \Sigma_{ijk}}{\partial x_m}(\mathbf{x}, \mathbf{y})u_i(\mathbf{y})\right] n_j(\mathbf{y})dS(\mathbf{y}), \end{aligned} \tag{33}$$

$$\begin{aligned}\sigma_{ij}(\mathbf{x}) &= \lim_{\boldsymbol{\xi}\to\mathbf{x}} \int_{\partial B} [D_{ijk}(\boldsymbol{\xi}, \mathbf{y})\tau_k(\mathbf{y}) - S_{ijk}(\boldsymbol{\xi}, \mathbf{y})u_k(\mathbf{y})]dS(\mathbf{y}) \\ &= \text{⨍}_{\partial B} [D_{ijk}(\mathbf{x}, \mathbf{y})\tau_k(\mathbf{y}) - S_{ijk}(\mathbf{x}, \mathbf{y})u_k(\mathbf{y})]dS(\mathbf{y}). \end{aligned} \tag{34}$$

Fully regularized forms of Eqs. (33) and (34), that only contain weakly singular integrals, are available in the literature [Cruse and Richardson (1996)]. These equations, that can be collocated at an irregular point $\mathbf{x} \in \partial B$ provided that the stress and displacement fields in (35) and (36) satisfy certain smoothness requirements [Martin *et al.* (1998)], are:

$$\begin{aligned} 0 &= \int_{\partial B} U_{ik,m}(\mathbf{x}, \mathbf{y})[\sigma_{ij}(\mathbf{y}) - \sigma_{ij}(\mathbf{x})]n_j(\mathbf{y})dS(\mathbf{y}) \\ &\quad - \int_{\partial B} \Sigma_{ijk,m}(\mathbf{x}, \mathbf{y})[u_i(\mathbf{y}) - u_i(\mathbf{x}) - u_{i,\ell}(\mathbf{x})(y_\ell - x_\ell)]n_j(\mathbf{y})dS(\mathbf{y}), \end{aligned} \tag{35}$$

$$\begin{aligned} 0 &= \int_{\partial B} D_{ijk}(\mathbf{x}, \mathbf{y})[\sigma_{kp}(\mathbf{y}) - \sigma_{kp}(\mathbf{x})]n_p(\mathbf{y})dS(\mathbf{y}) \\ &\quad - \int_{\partial B} S_{ijk}(\mathbf{x}, \mathbf{y})[u_k(\mathbf{y}) - u_k(\mathbf{x}) - u_{k,p}(\mathbf{x})(y_p - x_p)]dS(\mathbf{y}). \end{aligned} \tag{36}$$

2.2.3. *Displacement gradient on the bounding surface*

The gradient of the displacement $\mathbf{u}$ is required for the regularized HBIEs (35) and (36). Lutz *et al.* [1992] have proposed a scheme for carrying this out. Details of this procedure are available in Chati *et al.* [2001b] and are given below.

The (right-handed) global Cartesian coordinates, as before, are (x_1, x_2, x_3). Consider (right-handed) local Cartesian coordinates (x'_1, x'_2, x'_3) at a regular point P on

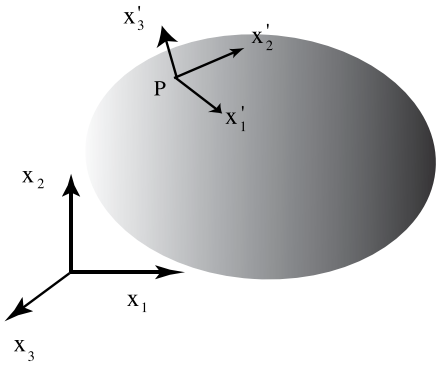

Fig. 2. Local coordinate system on the surface of a body (from Chati *et al.* [2001b]).

∂B as shown in Fig. 2. The local coordinate system is oriented such that the x_1' and the x_2' coordinates lie along the tangential unit vectors $\mathbf{t}_1$ and $\mathbf{t}_2$ while x_3' is measured along the outward normal unit vector $\mathbf{n}$ to ∂B as defined in Eq. (13).

Therefore, one has:

$$\mathbf{x}' = \mathbf{Q}\mathbf{x}, \tag{37}$$

$$\mathbf{u}' = \mathbf{Q}\mathbf{u}, \tag{38}$$

where u_k' are components of the displacement vector $\mathbf{u}$ in the local coordinate frame, and the orthogonal transformation matrix $\mathbf{Q}$ has the components:

$$\mathbf{Q} = \begin{bmatrix} t_{11} & t_{12} & t_{13} \\ t_{21} & t_{22} & t_{23} \\ n_1 & n_2 & n_3 \end{bmatrix}, \tag{39}$$

with t_{ij} the jth component of the ith unit tangent vector $\mathbf{t}_i$ in global coordinates (x_1, x_2, x_3). The tangential derivatives of the displacement, in local coordinates, are $u_{i,\alpha'}'$. These quantities are obtained as follows:

$$u_{i,\alpha'}' \equiv \frac{\partial u_i'}{\partial s_\alpha} = Q_{ij}\frac{\partial u_j}{\partial s_\alpha}, \tag{40}$$

where $\partial u_i'/\partial s_\alpha$ are tangential derivatives of u_i' at P with $s_1 = x_1'$ and $s_2 = x_2'$.

The remaining components of $\boldsymbol{\nabla}\mathbf{u}$ in local coordinates are obtained from Hooke's law [Lutz *et al.* (1992)] as:

$$\begin{aligned} \frac{\partial u_1'}{\partial x_3'} &= \frac{\tau_1'}{\mu} - \frac{\partial u_3'}{\partial x_1'}, \\ \frac{\partial u_2'}{\partial x_3'} &= \frac{\tau_2'}{\mu} - \frac{\partial u_3'}{\partial x_2'}, \\ \frac{\partial u_3'}{\partial x_3'} &= \frac{(1-2\nu)\tau_3'}{2\mu(1-\nu)} - \frac{\nu}{1-\nu}\left[\frac{\partial u_1'}{\partial x_1'} + \frac{\partial u_2'}{\partial x_2'}\right], \end{aligned} \tag{41}$$

where $\tau_k' = \sigma_{k3}'$ are components of the traction vector in local coordinates.

The components of the displacement gradient tensor $\mathbf{A}'$, in the local coordinate system, are now known.

Finally, the components of $\boldsymbol{\nabla}\mathbf{u}$ in the global coordinate frame are obtained from those in the local coordinate frame by using the tensor transformation rule:

$$(\boldsymbol{\nabla}\mathbf{u})_{\text{global}} \equiv \mathbf{A} = \mathbf{Q}^T\mathbf{A}'\mathbf{Q} = \begin{bmatrix} u_{1,1} & u_{1,2} & u_{1,3} \\ u_{2,1} & u_{2,2} & u_{2,3} \\ u_{3,1} & u_{3,2} & u_{3,3} \end{bmatrix}. \tag{42}$$

The gradient of the displacement field in global coordinates is now ready for use in Eqs. (35) and (36).

2.2.4. *Nearly singular integrals*

It is well known that the first step in the BEM is to solve the primary problem on the bounding surface of a body (e.g., Eq. (23)) and obtain all the displacements and tractions on this surface. The next steps are to obtain the displacements and stresses at selected points inside a body, from equations such as (16) and (28). It has been known in the BEM community for many years, dating back to Cruse [1969], that one experiences difficulties when trying to numerically evaluate displacements and stresses at points inside a body that are close to its bounding surface (the so-called near-singular or boundary layer problem). Various authors have addressed this issue over the last three decades. This section describes a method proposed in Mukherjee *et al.* [2000b].

Displacements at internal points close to the boundary. The displacement at a point inside an elastic body can be determined from either (equivalent) Eqs. (16) or (19). A continuous version of (19), from Cruse and Richardson [1996], is:

$$u_k(\boldsymbol{\xi}) = u_k(\hat{\mathbf{x}}) + \int_{\partial B} [U_{ik}(\boldsymbol{\xi}, \mathbf{y})\sigma_{ij}(\mathbf{y}) - \Sigma_{ijk}(\boldsymbol{\xi}, \mathbf{y})\{u_i(\mathbf{y}) - u_i(\hat{\mathbf{x}})\}] \times n_j(\mathbf{y}) dS(\mathbf{y}), \tag{43}$$

where $\boldsymbol{\xi} \in B$ is an internal point *close* to ∂B and a target point $\hat{\mathbf{x}} \in \partial B$ is *close* to the point $\boldsymbol{\xi}$ (see Fig. 3). An alternative form of (43) is:

$$u_k(\boldsymbol{\xi}) = u_k(\hat{\mathbf{x}}) + \int_{\partial B} [U_{ik}(\boldsymbol{\xi}, \mathbf{y})\tau_i(\mathbf{y}) - T_{ik}(\boldsymbol{\xi}, \mathbf{y})\{u_i(\mathbf{y}) - u_i(\hat{\mathbf{x}})\}] dS(\mathbf{y}). \tag{44}$$

Equation (43) (or (44)) is called "continuous" since it has a continuous limit to the boundary (LTB as $\boldsymbol{\xi} \to \hat{\mathbf{x}} \in \partial B$) provided that $u_i(\mathbf{y}) \in C^{0,\alpha}$ (i.e., Hölder continuous). Taking this limit is the standard approach for obtaining the well-known regularized form (24) (or (23)).

In this work, however, Eq. (43) (or (44)) is put to a different, and novel use. It is first observed that T_{ik} in Eq. (44) is $\mathcal{O}(1/r^2(\boldsymbol{\xi}, \mathbf{y}))$ as $\boldsymbol{\xi} \to \mathbf{y}$, whereas $\{u_i(\mathbf{y}) - u_i(\hat{\mathbf{x}})\}$ is $\mathcal{O}(r(\hat{\mathbf{x}}, \mathbf{y}))$ as $\mathbf{y} \to \hat{\mathbf{x}}$. Therefore, as $\mathbf{y} \to \hat{\mathbf{x}}$, the product $T_{ik}(\boldsymbol{\xi}, \mathbf{y})\{u_i(\mathbf{y}) - u_i(\hat{\mathbf{x}})\}$,

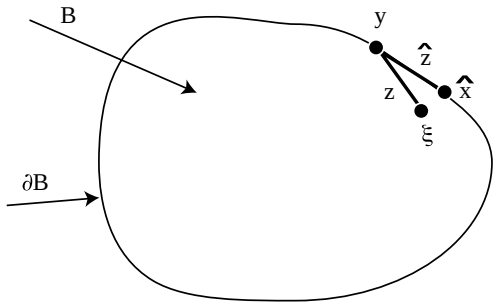

Fig. 3. A body with source point $\boldsymbol{\xi}$, field point $\mathbf{y}$ and target point $\hat{\mathbf{x}}$ (from Mukherjee *et al.* [2000b]).

which is $\mathcal{O}(r(\hat{\mathbf{x}},\mathbf{y})/r^2(\boldsymbol{\xi},\mathbf{y}))$, $\to 0$! As a result, Eq. (44) (or (43)) can be used to easily and accurately evaluate the displacement components $u_k(\boldsymbol{\xi})$ for $\boldsymbol{\xi} \in B$ close to ∂B. This idea is the main contribution of Mukherjee *et al.* [2000b].

It is noted here that while it is usual to use (16) (or (19)) to evaluate $u_k(\boldsymbol{\xi})$ when $\boldsymbol{\xi}$ is *far* from ∂B, Eq. (43) (or (44)) is also valid in this case. (The target point $\hat{\mathbf{x}}$ can be chosen as *any* point on ∂B when $\boldsymbol{\xi}$ is far from ∂B.) Therefore, it is advisable to use the continuous Eq. (43) (or (44)) universally for all points $\boldsymbol{\xi} \in B$. This procedure would eliminate the need to classify, a priori, whether $\boldsymbol{\xi}$ is near to, or far from ∂B.

Stresses at internal points close to the boundary. The displacement gradient at a point $\boldsymbol{\xi} \in B$ can be obtained from Eq. (32) or stresses at this point from (28). Continuous versions of (32) and (28) can be written as [Cruse and Richardson (1996)]:

$$u_{k,n}(\boldsymbol{\xi}) = u_{k,n}(\hat{\mathbf{x}}) - \int_{\partial B} U_{ik,n}(\boldsymbol{\xi},\mathbf{y})[\sigma_{ij}(\mathbf{y}) - \sigma_{ij}(\hat{\mathbf{x}})]n_j(\mathbf{y})dS(\mathbf{y})$$
$$+ \int_{\partial B} \Sigma_{ijk,n}(\boldsymbol{\xi},\mathbf{y})[u_i(\mathbf{y}) - u_i(\hat{\mathbf{x}}) - u_{i,\ell}(\hat{\mathbf{x}})(y_\ell - \hat{x}_\ell)]n_j(\mathbf{y})dS(\mathbf{y}), \quad (45)$$

$$\sigma_{ij}(\boldsymbol{\xi}) = \sigma_{ij}(\hat{\mathbf{x}}) + \int_{\partial B} D_{ijk}(\boldsymbol{\xi},\mathbf{y})[\tau_k(\mathbf{y}) - \sigma_{km}(\hat{\mathbf{x}})n_m(\mathbf{y})]dS(\mathbf{y})$$
$$- \int_{\partial B} S_{ijk}(\boldsymbol{\xi},\mathbf{y})[u_k(\mathbf{y}) - u_k(\hat{\mathbf{x}}) - u_{k,\ell}(\hat{\mathbf{x}})(y_\ell - \hat{x}_\ell)]dS(\mathbf{y}). \quad (46)$$

The integrands in Eq. (45) (or (46)) are $\mathcal{O}(r(\hat{\mathbf{x}},\mathbf{y})/r^2(\boldsymbol{\xi},\mathbf{y}))$ and $\mathcal{O}(r^2(\hat{\mathbf{x}},\mathbf{y})/r^3(\boldsymbol{\xi},\mathbf{y}))$ as $\mathbf{y} \to \hat{\mathbf{x}}$. Similar to the behavior of the continuous BIEs in the previous subsection, the integrands in Eqs. (45) and (46) $\to 0$ as $\mathbf{y} \to \hat{\mathbf{x}}$. Either of these equations, therefore, is useful for evaluating the stresses at an internal point $\boldsymbol{\xi}$ that is *close* to ∂B. Of course (see the discussion regarding displacements in the previous subsection), they can also be conveniently used to evaluate displacement gradients or stresses at *any* point $\boldsymbol{\xi} \in B$.

2.3. *Acoustics*

Linear acoustic wave problems are governed by the Helmholtz equation:

$$\nabla^2\phi + k^2\phi = 0 \quad \forall\, \mathbf{x} \in \mathrm{B}, \tag{47}$$

where $\phi(\mathbf{x}, \omega)$ is the complex acoustic pressure, $k = \omega/c$ the wavenumber, ω the circular frequency, and c the speed of sound in the acoustic medium occupying domain B (see Fig. 1). Domain B can be an exterior domain, for example, outside a vibrating structure.

The boundary conditions can be classified as follows:

$$\text{Pressure is given:} \quad \phi = \bar{\phi}, \quad \forall\, \mathbf{x} \in \partial\mathrm{B}, \tag{48}$$

$$\text{Velocity is given:} \quad q = \frac{\partial\phi}{\partial n} = \bar{q} = i\omega\rho\bar{v}_n, \quad \forall\, \mathbf{x} \in \partial\mathrm{B}, \tag{49}$$

$$\text{Impedance is given:} \quad \phi = Z\bar{v}_n, \quad \forall\, \mathbf{x} \in \partial\mathrm{B}, \tag{50}$$

where ρ is the mass density, v_n the normal particle velocity, Z the specific impedance, and the barred quantities indicate given values. For exterior (infinite domain) acoustic wave problems, in addition to the boundary conditions on ∂B, the field at infinity must also satisfy the Sommerfeld radiation condition.

2.3.1. *Singular integral equations*

Integral equations have been applied for solving acoustic wave problems for decades [Schenck (1968); Burton and Miller (1971); Kress (1985); Seybert *et al.* (1985)]. In the direct BIE formulation, the representation integral of the solution to equation (47) is given as [Seybert *et al.* (1985); Liu and Rizzo (1992); Liu and Chen (1999)]:

$$\phi(\boldsymbol{\xi}) = \int_{\partial B} [G(\boldsymbol{\xi}, \mathbf{y}, \omega)q(\mathbf{y}) - F(\boldsymbol{\xi}, \mathbf{y}, \omega)\phi(\mathbf{y})]dS(\mathbf{y}) + \phi^I(\boldsymbol{\xi}), \tag{51}$$

where $\boldsymbol{\xi} \in B, \phi^I(\boldsymbol{\xi})$ is a possible incident wave for an exterior problem, and the two kernels for 3D problems are given by:

$$G(\boldsymbol{\xi}, \mathbf{y}, \omega) = \frac{1}{4\pi r(\boldsymbol{\xi}, \mathbf{y})} e^{ikr(\boldsymbol{\xi}, \mathbf{y})}, \tag{52}$$

$$\begin{aligned} F(\boldsymbol{\xi}, \mathbf{y}, \omega) &= \frac{\partial G(\boldsymbol{\xi}, \mathbf{y}, \omega)}{\partial n(\mathbf{y})} \\ &= \frac{1}{4\pi r^2(\boldsymbol{\xi}, \mathbf{y})}[ikr(\boldsymbol{\xi}, \mathbf{y}) - 1]r_{,j}(\boldsymbol{\xi}, \mathbf{y})n_j(\mathbf{y})e^{ikr(\boldsymbol{\xi}, \mathbf{y})}. \end{aligned} \tag{53}$$

Let the source point $\boldsymbol{\xi}$ approach a point $\mathbf{x}$ on the boundary. One then obtains the following singular BIE [Seybert *et al.* (1985); Liu and Rizzo (1992); Liu and Chen (1999)]:

$$c(\mathbf{x})\phi(\mathbf{x}) = \int_{\partial B} [G(\mathbf{x}, \mathbf{y}, \omega)q(\mathbf{y}) - F(\mathbf{x}, \mathbf{y}, \omega)\phi(\mathbf{y})]dS(\mathbf{y}) + \phi^I(\mathbf{x}), \tag{54}$$

where $c(\mathbf{x}) = 1/2$ if ∂B is smooth at $\mathbf{x}$. In the general case (i.e., when the boundary is not smooth at $\mathbf{x}$), $c(\mathbf{x})$ can be represented as a CPV integral of the static kernel F over the boundary ∂B. Its value can be determined numerically from the sum of the off-diagonal elements (from this kernel), in the same row, in a BEM implementation of this BIE [Liu (2009)].

This BIE (54) can be employed to solve for the unknowns ϕ and q on ∂B. The integral with the G kernel is a weakly singular integral, while the one with the F kernel is a strongly singular (CPV) integral, as in the potential case.

A regularized or weakly singular form of the BIE (54) can be derived by using the identities for the static kernels [Liu and Rudolphi (1991, 1999); Liu (2000, 2009)]:

$$\gamma\phi(\mathbf{x}) + \int_{\partial B} [F(\mathbf{x},\mathbf{y},\omega) - \overline{F}(\mathbf{x},\mathbf{y})]\phi(\mathbf{y})dS(\mathbf{y}) + \int_{\partial B} \overline{F}(\mathbf{x},\mathbf{y})[\phi(\mathbf{y}) - \phi(\mathbf{x})]dS(\mathbf{y})$$
$$= \int_{\partial B} G(\mathbf{x},\mathbf{y},\omega)q(\mathbf{y})dS(\mathbf{y}) + \phi^I(\mathbf{x}), \tag{55}$$

in which $\overline{F}(\mathbf{x},\mathbf{y}) = F(\mathbf{x},\mathbf{y},0)$ is the static F kernel for potential problems (see Eq. (4)). (A bar has been added in this section to distinguish the static kernels from the dynamic ones.) Also, $\gamma = 0$ for finite domain and $\gamma = 1$ for infinite domain problems. All the three integrals in Eq. (55) are now at most weakly singular and can be handled readily using standard numerical integration schemes.

2.3.2. *Hypersingular integral equations*

It is well known that the acoustic BIE has a major defect for exterior problems, that is, it has nonunique solutions at a set of fictitious eigenfrequencies associated with the resonant frequencies of the corresponding interior problems [Burton and Miller (1971)]. This difficulty is referred to as the fictitious eigenfrequency difficulty. A remedy to this problem is to use the normal derivative BIE in conjunction with the standard BIE. Taking the derivative of integral representation (51) with respect to the normal at a point $\mathbf{x}$ on ∂B, and letting $\boldsymbol{\xi}$ approach $\mathbf{x}$, one obtains the following HBIE:

$$c(\mathbf{x})q(\mathbf{x}) = \int_{\partial B} [K(\mathbf{x},\mathbf{y},\omega)q(\mathbf{y}) - H(\mathbf{x},\mathbf{y},\omega)\phi(\mathbf{y})]dS(\mathbf{y}) + q^I(\mathbf{x}), \tag{56}$$

where $c(\mathbf{x}) = 1/2$ if ∂B is smooth at $\mathbf{x}$. For 3D problems, the two new kernels are given by:

$$K(\mathbf{x},\mathbf{y},\omega) = \frac{\partial G(\mathbf{x},\mathbf{y},\omega)}{\partial n(\mathbf{x})}$$
$$= -\frac{1}{4\pi r^2(\mathbf{x},\mathbf{y})}[ikr(\mathbf{x},\mathbf{y}) - 1]r_{,j}(\mathbf{x},\mathbf{y})n_j(\mathbf{x})e^{ikr(\mathbf{x},\mathbf{y})}, \tag{57}$$

$$H(\mathbf{x},\mathbf{y},\omega) = \frac{\partial F(\mathbf{x},\mathbf{y},\omega)}{\partial n(\mathbf{x})}$$
$$= \frac{1}{4\pi r^3}\{[1-ikr(\mathbf{x},\mathbf{y})]n_j(\mathbf{y}) + (k^2r^2(\mathbf{x},\mathbf{y})$$
$$- 3[1-ikr(\mathbf{x},\mathbf{y})])r_{,j}(\mathbf{x},\mathbf{y})r_{,\ell}(\mathbf{x},\mathbf{y})n_\ell(\mathbf{y})\}n_j(\mathbf{x})e^{ikr(\mathbf{x},\mathbf{y})}. \quad (58)$$

In the HBIE (56), the integral with the kernel K is a strongly-singular integral, while the one with the H kernel is a hypersingular (FP) integral.

The HBIE (56) can be written in the following regularized or weakly-singular form [Liu and Rizzo (1992); Liu and Chen (1999)]:

$$\gamma q(\mathbf{x}) + \int_{\partial B}[H(\mathbf{x},\mathbf{y},\omega) - \overline{H}(\mathbf{x},\mathbf{y})]\phi(\mathbf{y})dS(\mathbf{y})$$
$$+ \int_{\partial B}\overline{H}(\mathbf{x},\mathbf{y})\left[\phi(\mathbf{y}) - \phi(\mathbf{x}) - \frac{\partial\phi}{\partial s_\alpha}(\mathbf{x})(s_\alpha - s_{o\alpha})\right]dS(\mathbf{y})$$
$$+ e_{\alpha k}\frac{\partial\phi}{\partial s_\alpha}(\mathbf{x})\int_{\partial B}[\overline{K}(\mathbf{x},\mathbf{y})n_k(\mathbf{y}) + \overline{F}(\mathbf{x},\mathbf{y})n_k(\mathbf{x})]dS(\mathbf{y})$$
$$= \int_{\partial B}[K(\mathbf{x},\mathbf{y},\omega) + \overline{F}(\mathbf{x},\mathbf{y})]q(\mathbf{y})dS(\mathbf{y})$$
$$- \int_{\partial B}\overline{F}(\mathbf{x},\mathbf{y})[q(\mathbf{y}) - q(\mathbf{x})]dS(\mathbf{y}) + q^I(\mathbf{x}), \quad (59)$$

in which s_α ($\alpha = 1, 2$) are local coordinates in two tangential directions at $\mathbf{x} \in \partial B$ and $e_{\alpha k} = \partial s_\alpha/\partial x_k$ [Liu and Rizzo (1992); Liu and Chen (1999)]. All integrals in (59) are now at most weakly singular if ϕ has continuous first derivatives.

For exterior acoustic wave problems, a dual BIE (or composite BIE [Liu and Rizzo (1992)]) formulation using a linear combination of BIE (54) and HBIE (56) can be written as:

$$\text{BIE} + \beta\,\text{HBIE} = 0, \quad (60)$$

where β is the coupling constant. This formulation is called Burton–Miller formulation [Burton and Miller (1971)] for acoustic wave problems and has been shown to yield unique solutions at all frequencies, if β is a complex number (which, for example, can be chosen as $\beta = i/k$ with $i = \sqrt{-1}$ [Kress (1985)]).

3. Specialized Applications

BEM formulations for problems involving thin structures (beams, plates, shells, gaps) are very interesting. Thin beams are first considered in this section. This is followed by a discussion of BEM formulations for MEMS.

3.1. *Thin bodies*

Many boundary value problems that are solved by the BEM involve bodies with 1D that is much smaller than the other two (or 2Ds that are much smaller than

the third). Common examples are thin plates and shells (or beams). This section presents BEM formulations for 2D potential theory in a region exterior to thin beams, for applications in MEMS.

The first step in MEMS analysis requires solving for the electric field exterior to thin conducting beams by the BEM. A convenient way to model such a problem is to assume that a beam has vanishing thickness and solve the sum of the charges on the upper and the lower surfaces of the beam [Harrington (1993)]. The standard BIE with a weakly singular kernel is used here and this approach works well for determining, for example, the capacitance of a parallel plate capacitor. For MEMS calculations, however, one must obtain the charge densities separately on the upper and the lower surfaces of a beam since the traction at a surface point on a beam depends on the square of the charge density at that point. The gradient BIE is employed in Bao and Mukherjee [2005] to obtain these charge densities separately. The formulation given in Bao and Mukherjee [2005] is a BEM scheme that is particularly well-suited for MEMS analysis of very thin beams — for $h/L \approx 0.001$ — in terms of the length L of a beam and its thickness h. A similar approach has also been developed for MEMS with very thin plates in Bao and Mukherjee [2004]. Similar work has also been reported by Liu [2006] on a dual BIE approach to address large scale 2D beam models and by Chuyan *et al.* [2005] in the context of determining fringing fields and levitating forces for 2D beam shaped conductors in MEMS combdrives.

Two approaches for determining the charge density on the outer surfaces of conducting beams are discussed below. One approach is that presented in Bao and Mukherjee [2005] (here called the sum of charges approach); the other presented in Liu [2006] (here called the dual BIE approach).

3.1.1. *BIEs in infinite region containing two thin conducting beams — Sum of charges approach*

Figure 4 shows two parallel conducting beams and the region outside them. The top beam can be considered to be the physical object and the bottom beam its image in order to model the ground plane.

Of interest is the solution of the following Dirichlet problem for Laplace's equation:

$$\nabla^2\phi(\mathbf{x}) = 0, \quad \mathbf{x} \in B, \quad \phi(\mathbf{x}) \text{ prescribed for } \mathbf{x} \in \partial\mathbf{B}, \tag{61}$$

where B is now the region *exterior* to the two beams. The unit normal $\mathbf{n}$ to B is defined to point away from B (i.e., into a beam). In Fig. 4, $\mathbf{x}^+$ is a collocation point on s_1^+, and $\hat{s}_1^+$ is a boundary element containing $\mathbf{x}^+$.

For this problem, one can write [Bao and Mukherjee (2005)]:

$$\phi(\boldsymbol{\xi}) = -\int_s \frac{\ln r(\boldsymbol{\xi}, \mathbf{y})\sigma(\mathbf{y})ds(\mathbf{y})}{2\pi\epsilon} + C, \tag{62}$$

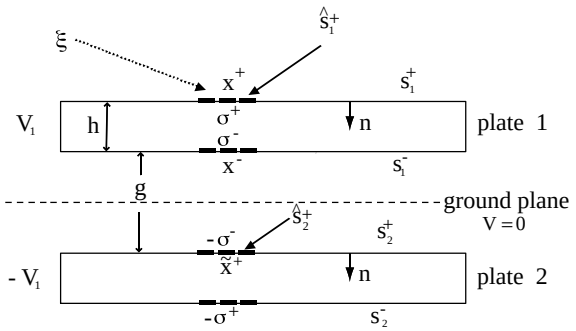

Fig. 4. Two parallel conducting beams (from Bao and Mukherjee [2005]).

where σ is the charge density (per unit area) at a point on a beam surface, ϵ is the permittivity of the medium exterior to the two beams and s is the total outer surface of the two beams. The constant C is given by the expression:

$$C = \phi_\infty - G(R_\infty)Q, \tag{63}$$

where ϕ_∞ and $G(R_\infty)$ are the potential and the Green's function at infinity, respectively, and Q is the total charge on the two beams. Note that the Green's function for the 2D Laplace equation is:

$$G(\mathbf{x}, \mathbf{y}) = -\frac{1}{2\pi} \ln(r(\mathbf{x}, \mathbf{y})). \tag{64}$$

The constant C is usually determined from the constraint equation:

$$\int_s \sigma(\mathbf{y}) ds(\mathbf{y}) = Q. \tag{65}$$

It is proved in Bao and Mukherjee [2005] that, for the situation depicted in Fig. 4, $Q = 0$, and $\phi_\infty = 0$, so that $C = 0$.

Regular BIE — Source point approaching a beam surface s_1^+. It has been shown in Bao and Mukherjee [2005] that for this case:

$$\begin{aligned} 2\pi\epsilon\phi(\mathbf{x}^+) = &- \int_{s_1^+ - \hat{s}_1^+} \ln r(\mathbf{x}^+, \mathbf{y}) \beta(\mathbf{y}) ds(\mathbf{y}) - \int_{\hat{s}_1^+} \ln r(\mathbf{x}^+, \mathbf{y}) \beta(\mathbf{y}) ds(\mathbf{y}) \\ &- \int_{s_2^+} \ln r(\mathbf{x}^+, \mathbf{y}) \beta(\mathbf{y}) ds(\mathbf{y}). \end{aligned} \tag{66}$$

Here $\beta(\mathbf{y}) = \sigma(\mathbf{y}^+) + \sigma(\mathbf{y}^-)$. The second integral in Eq. (66) is logarithmically singular and the rest are regular except when the beam thickness and the gap become very small.

A similar equation can be written for $\mathbf{x}^+ \in s_2^+$. For the case shown in Fig. 4, however, it is not necessary since $\beta(\mathbf{y})$ is equal and opposite on the two beams. Therefore, for this case, Eq. (66) is sufficient to solve for β on both the beams.

Hypersingular BIE — Source point approaching a beam surface s_1^+. It is first noted that for $\mathbf{x}^+ \in s_k^+ \cup s_k^-, k = 1, 2$:

$$\sigma(\mathbf{x}) = \epsilon \frac{\partial \phi}{\partial n}(\mathbf{x}) = \epsilon \mathbf{n}(\mathbf{x}) \cdot [\nabla_{\boldsymbol{\xi}} \phi(\boldsymbol{\xi})]_{\boldsymbol{\xi}=\mathbf{x}}. \tag{67}$$

Consider the limit $\boldsymbol{\xi} \to \mathbf{x}^+ \in \hat{s}_1^+ \in s_1^+$. It is important to realize that this limit is meaningless for a point $\mathbf{x}$ on the edge of a beam, since the charge density is singular on its edges. One obtains the following HBIE:

$$\begin{aligned}\sigma(\mathbf{x}^+) = & \int_{s_1^+ - \hat{s}_1^+} \frac{\beta(\mathbf{y}) \mathbf{r}(\mathbf{x}^+, \mathbf{y}) \cdot \mathbf{n}(\mathbf{x}^+)}{2\pi r^2(\mathbf{x}^+, \mathbf{y})} ds(\mathbf{y}) \\ & + \int_{\hat{s}_1^+} \frac{\mathbf{r}(\mathbf{x}^+, \mathbf{y}) \cdot [\beta(\mathbf{y}) \mathbf{n}(\mathbf{x}^+) - \beta(\mathbf{x}) \mathbf{n}(\mathbf{y})]}{2\pi r^2(\mathbf{x}^+, \mathbf{y})} ds(\mathbf{y}) \\ & + \frac{\beta(\mathbf{x})}{2\pi} \Psi(\hat{s}_1^+, \mathbf{x}^+) + \int_{s_2^+} \frac{\beta(\mathbf{y}) \mathbf{r}(\mathbf{x}^+, \mathbf{y}) \cdot \mathbf{n}(\mathbf{x}^+)}{2\pi r^2(\mathbf{x}^+, \mathbf{y})} ds(\mathbf{y}). \end{aligned} \tag{68}$$

In Eq. (68), the angle subtended by the line element $\hat{s}_1^+$ at the point $\mathbf{x}^+$ [Bao and Mukherjee (2005) and Fig. 5] is:

$$\Psi(\hat{s}_1^+, \mathbf{x}^+) = \oint_{\hat{s}_1^+} \frac{\mathbf{r}(\mathbf{x}^+, \mathbf{y}) \cdot \mathbf{n}(\mathbf{y})}{r^2(\mathbf{x}^+, \mathbf{y})} ds(\mathbf{y}) = \psi_A + \psi_B. \tag{69}$$

A unit vector $\mathbf{u}$, through the point $\mathbf{x}^+$, is chosen such that it intersects $\hat{s}_1^+$ (see Fig. 5). The direction of this unit vector $\mathbf{u}$ is arbitrary except that it must lie between $\mathbf{x}^+A$ and $\mathbf{x}^+B$ (or between $\mathbf{x}^-A$ and $\mathbf{x}^-B$) as shown in Fig. 5. Now, ψ is the angle between the positive $\mathbf{u}$ vector and $\mathbf{r}(\mathbf{x}^+, \mathbf{y})$ with $\mathbf{y} \in \hat{s}_1^+$; i.e.,

$$\cos(\psi(\mathbf{y})) = \frac{\mathbf{r}(\mathbf{x}^+, \mathbf{y}) \cdot \mathbf{u}}{r(\mathbf{x}^+, \mathbf{y})}. \tag{70}$$

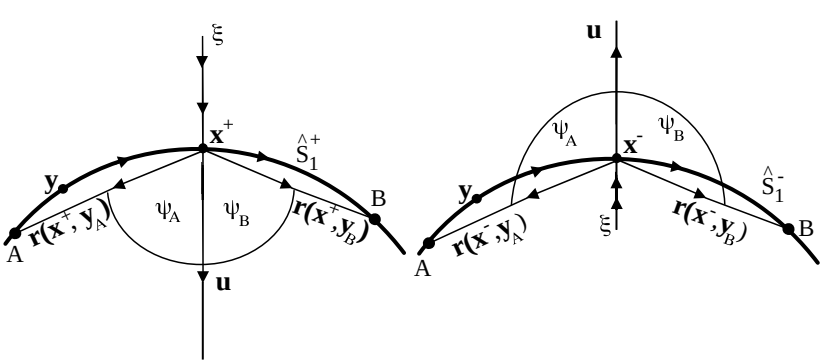

Fig. 5. Evaluations of angles (from Bao and Mukherjee [2005]).

Writing Eq. (68) at $\mathbf{x}^-$ together with some algebraic manipulation gives:

$$\frac{1}{2}[\sigma(\mathbf{x}^+) - \sigma(\mathbf{x}^-)] = \int_{s_1^+ - \hat{s}_1^+} \frac{\beta(\mathbf{y})\mathbf{r}(\mathbf{x}^+, \mathbf{y}) \cdot \mathbf{n}(\mathbf{x}^+)}{2\pi r^2(\mathbf{x}^+, \mathbf{y})} ds(\mathbf{y}) + \int_{\hat{s}_1^+} \frac{\mathbf{r}(\mathbf{x}^+, \mathbf{y}) \cdot [\beta(\mathbf{y})\mathbf{n}(\mathbf{x}^+) - \beta(\mathbf{x})\mathbf{n}(\mathbf{y})]}{2\pi r^2(\mathbf{x}^+, \mathbf{y})} ds(\mathbf{y}) - \frac{\beta(\mathbf{x})}{2\pi}[\pi - \Psi(\hat{s}_1^+, \mathbf{x}^+)] + \int_{s_2^+} \frac{\beta(\mathbf{y})\mathbf{r}(\mathbf{x}^+, \mathbf{y}) \cdot \mathbf{n}(\mathbf{x}^+)}{2\pi r^2(\mathbf{x}^+, \mathbf{y})} ds(\mathbf{y}). \tag{71}$$

Equation (66) gives the sum of the charge densities and the HBIE (71) can be used as a post-processing step to compute values of individual charge densities on each of the beams.

3.1.2. *BIEs in infinite region containing two thin conducting beams — Dual BIE approach*

This approach is described in detail in Liu [2006].

The regular BIE (62), collocated at a boundary point $\mathbf{x}$ (i.e., $\boldsymbol{\xi}$ in (62) is now replaced by $\mathbf{x}$) is used again. This is called the regular MEMS-BIE in the present paper.

Next, the gradient Eq. (67), collocated at a point $\mathbf{x} \in s$ where the boundary is locally smooth, is:

$$(1/2)\sigma(\mathbf{x}) = \int_s \frac{\partial G(\mathbf{x}, \mathbf{y})}{\partial n(\mathbf{x})} \sigma(\mathbf{y}) ds(\mathbf{y}), \tag{72}$$

where G is the Green's function (64) for the 2D Laplace equation.

Equation (72), called the gradient MEMS-BIE in the present paper, is a homogeneous equation which cannot be applied alone to directly solve for the charge density on the surface of a conductor.

The dual BIE approach, proposed in Liu [2006], is described below. As shown in Fig. 4, the thin beam shaped conductors are similar to open cracks (when the beam thickness is small but finite) or true cracks (when the beam thickness approaches zero) in elasticity problems. For crack problems, dual BIE approaches combining the regular and gradient BIEs have been proven to be very effective [Krishnasamy *et al.* (1994); Liu and Rizzo (1997)]. The advantages of dual BIE approaches are that they are valid for both open and true cracks, without the need to switch BIE formulations, and the original boundary variables can be solved directly. Because of the similarities mentioned above, it is expected that dual BIE approaches should be equally effective for solving electrostatic problems with thin beams (inclusions). The following two dual BIE formulations have been tested in Liu [2006] and both have been found to be effective for modeling MEMS with thin beams.

Dual BIE (a). In this approach, the regular MEMS-BIE (62) is applied to the top and edge surfaces of a beam while the gradient MEMS-BIE (72) is applied to the bottom surface of a beam [Krishnasamy *et al.* (1994); Liu and Rizzo (1997)]. The disadvantage of this approach is that the coefficients are not uniform regarding their orders of magnitude, since part of them come from the regular and others from the gradient BIE, which has a different order of singularity compared to the regular BIE.

Dual BIE (b). In this approach, a linear combination of the regular and the gradient MEMS-BIE is applied on the entire surface (of all the beams), in the form:

$$\gamma(\text{regular MEMS-BIE}) + \delta(\text{gradient MEMS-BIE}) = 0, \tag{73}$$

where γ and δ are constants. Appropriate selection of these constants is crucial for the performance of the dual BIE (b). In general, δ should be smaller than γ so that the gradient BIE will not dominate in this dual BIE formulation. In the study of MEMS problems with thin beams, the choice $\gamma = 1$ and $\delta = h_0 - h$ (where h_0 is a reference thickness) has been found to be sufficient. For acoustic problems, (73) is the Burton–Miller BIE formulation (60) which is very effective for overcoming fictitious eigenfrequency difficulties for exterior problems [Burton and Miller (1971); Liu and Rizzo (1992)]. The advantage of this linear combination is that the same BIE formulation is applied uniformly over the entire boundary and, therefore, better numerical conditioning can be expected from this approach.

For constant elements, both the G and $\partial G/\partial n$ integrals in the BIEs (62) (with $\boldsymbol{\xi} = \mathbf{x}$) and (72) are integrated analytically, for all (nonsingular, nearly singular and singular) cases. Thus, the computer codes can handle very thin beams with very small but finite thicknesses, and/or with small gaps, in the MEMS models. Difficulties related to numerical evaluation of nearly singular or singular integrals are overcome by this analytical integration of singular kernels.

3.2. *Micro-electro-mechanical systems*

The field of MEMS is a very broad one that includes fixed or moving microstructures; encompassing micro-electro-mechanical, microfluidic, micro-electro-fluidic-mechanical, micro-opto-electro-mechanical and micro-thermo-mechanical devices and systems. MEMS usually consist of released microstructures that are suspended and anchored, or captured by a hub-cap structure and set into motion by mechanical, electrical, thermal, acoustical or photonic energy source(s).

Typical MEMS structures consist of arrays of thin plates with cross-sections in the order of microns^2 (μm^2) and lengths in the order of ten to hundreds of microns (see, for example, Fig. 6). Sometimes, MEMS structural elements are beams. An example is a small rectangular silicon beam with length in the order of mm and thickness of the order of microns, that deforms when subjected to electric fields. Owing to its small size, significant forces and/or deformations can be obtained with the application of low voltages (≈ 10 V). Examples of devices that utilize vibrations

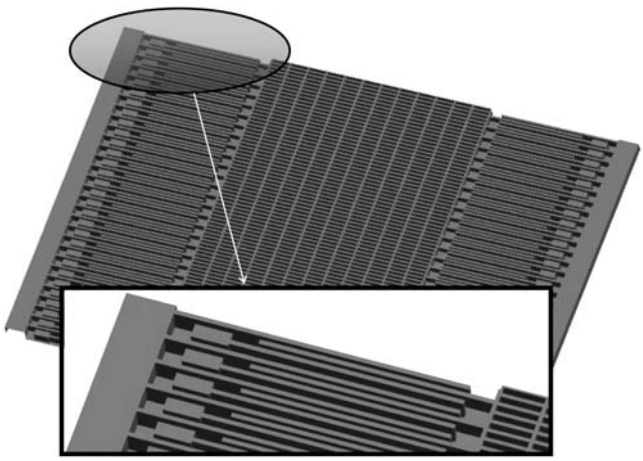

Fig. 6. Parallel plate resonator: Geometry and detail of the parallel plate fingers (from Frangi and diGioa [2005]).

of such beams are comb drives (see Fig. 6), synthetic micro-jets [Roman and Aubry (2003)] (for chemical mixing, cooling of electronic components, micro-propulsion and turbulence control), microspeakers [Ko *et al.* (2003)], etc.

Numerical simulation of electrically actuated MEMS devices have been carried out for nearly two decades using the BEM [Mukherjee (1982); Banerjee (1994); Chandra and Mukherjee (1997); Bonnet (1999); Mukherjee and Mukherjee (2005); Liu (2009)] to model the exterior electric field and the FEM [Yang (1986); Zienkiewicz and Taylor (1994); Hughes (2000); Belytschko *et al.* (2000)] to model deformation of the structure. The commercial software package MEMCAD [Senturia *et al.* (1992)], for example, uses the commercial FEM software package ABAQUS for mechanical analysis, together with a BEM code FastCap [Nabors and White (1991)] for electric field analysis. Other examples of such work are [Gilbert *et al.* (1995); Shi *et al.* (1995); Aluru and White (1997); Das and Batra (2009a); Liu (2006); Liu and Shen (2007)]; as well as, for example, [Senturia *et al.* (1992); Shi *et al.* (1996); Das and Batra (2009b); De and Aluru (2004)] for dynamic analysis of MEMS.

The focus of this section is the study of charge distribution in MEMS devices made up of very thin conducting beams. Integral equations used for this analysis are given in Sec. 3.1. It is noted here that charge distribution on nanoscale objects (conducting carbon nanotubes and semi conducting silicon nanowires) has been studied [Chen and Mukherjee (2006); Chen *et al.* (2008)].

3.2.1. *Numerical results from the sum of charges approach*

The numerical results presented in this section are taken from Bao and Mukherjee [2005].

The model problem chosen here is a two beam capacitor shown in Fig. 4. The length L of each beam is 10 mm, $g/L = 0.1$. The constant ϵ of the external medium is unity. The voltages on the upper and lower plates are $V_1 = +1$ and $V_2 = -1$, respectively. Here, as mentioned before, $C = \phi_\infty = 0$.

Although the thin beam approximation in the sum of charges approach assumes $h/L \approx 0$, an actual value for h must be specified in the numerical calculations because of the way the gap is defined in Fig. 4. According to this figure, the distance between the top surfaces of the two thin beams is taken to be $g + h$ in the thin beam BIE model. For consistency, the same is done for the regular BEM, i.e., the gap between the two beams is also taken as $g + h$ in this case.

The regular BEM uses strictly quadratic elements. (Note that the interpolation functions for the usual quadratic element are: $\eta(\eta-1)/2, (1-\eta^2), \eta(1+\eta)/2$ with $\eta_1 = -1, \eta_2 = 0, \eta_3 = 1$ at the left end, center and right end, respectively, of the master element. Here η is the coordinate on the element of normalized length equal to 2.) Quadratic boundary elements are also used in the sum of charges BEM calculations. However, the first and last boundary elements (in the sum of charges BEM) are nonconforming ones (with $\eta_1 = -0.5, \eta_2 = 0; \eta_3 = 1.0$; and $\eta_1 = -1.0, \eta_2 = 0, \eta_3 = 0.5$, respectively), to allow for singularities in β at $x_1 \pm 0.5$. The rest of the elements are the usual quadratic conforming ones.

The analytical solution for the charge density σ^-, on the lower surface of the top beam in Fig. 4, is given by Hayt and Buck [2001]:

$$\sigma^- = \epsilon \frac{\partial \phi}{\partial n} = \epsilon \frac{2V}{g+h}, \tag{74}$$

at a point reasonably far from the edges of the beam.

Figure 7 shows the variation of the charge densities σ^- and σ^+ along the bottom beam, as obtained from the sum of charges BEM. It is seen that nonconforming elements are needed at the ends of the beams in order to get the proper variation of the charge densities near their ends.

Results from the thin beam BEM are compared with those from the regular BEM and the analytical solution (74) in Table 1, for various values of h/L. As before, $L = 10\,\text{mm}, g/L = 0.1, V_1 = +1, V_2 = -1$ and $C = \phi_\infty = 0$. In both versions of the BEM, log singular integrals are evaluated by the method outlined in Telukunta and Mukherjee [2004]. Nearly log singular integrals appear only in the standard BEM and these, in the interest of "standardization", are evaluated by usual Gauss quadrature.

For the sum of charges BEM solution, σ^- is within around 1% of the analytical solution for $h = 1\,\text{mm}$. Its accuracy improves (as expected) with decreasing beam thickness and the error is around 0.4% for $h = 10^{-2}\,\text{mm}$. The regular BEM fails with this mesh for $h = 10^{-2}\,\text{mm}$.

3.2.2. *Numerical results from the dual BIE approach*

The numerical results presented in this section are taken from Liu [2006].

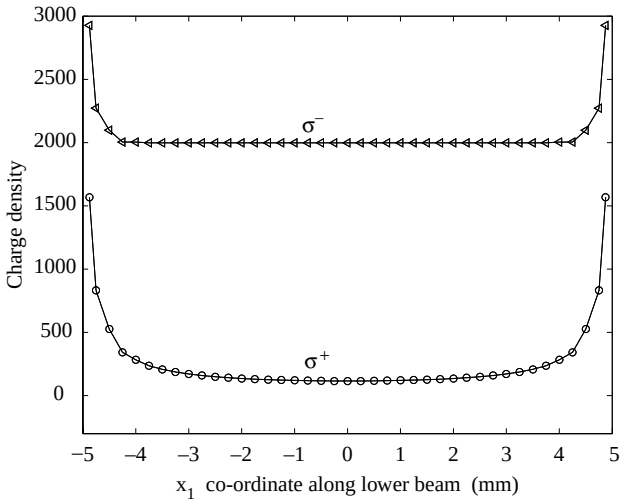

Fig. 7. Charge density distribution, along the bottom beam of the two beam model from Fig. 4, from the sum of charges BEM model. Twenty boundary elements are used on the upper surface of each beam. $h/L = 10^{-4}$. The unit of the charge density is C/m^2 (from Bao and Mukherjee [2005]).

Table 1. Comparison of sum of charges BEM, regular BEM and analytical solution for σ^- for the two beam problem.

h/L	Regular BEM		Sum of Charges BEM		Analytical Soln.
	σ^-	σ^+	σ^-	σ^+	σ^-
0.1	1,107	96.51	989.6	119.8	1,000
0.05	1,409	103.8	1,324	122.0	1,333
0.01	1,840	114.4	1,810	123.8	1,818
0.005	1,917	99.95	1,896	124.1	1,905
0.001	—	—	1,972	124.3	1,980

Note: Mesh: Sum of charges BEM: 20 quadratic elements on the top surface of each beam with singular elements at the ends. Regular BEM: 20 quadratic elements on the top and bottom surfaces of each beam; one quadratic element on each side surface. The charge densities σ^+ and σ^- are tabulated at the center of the top beam. The regular BEM fails (with this mesh) for $h/L = 0.001$.

Two beam capacitor from Fig. 4. The two beam capacitor model is considered first. One model, with parameters $\epsilon = 1, L = 0.01\,\text{m}, h/L = 0.01, g/L = 0.1$, $V = +1, C = 0$ (note that the total gap is again $g+h$) is tested first with the regular BIE and dual BIEs (a) and (b), with constant elements. The number of elements along the beam length is increased from 10, 20, 50 to 100, while five elements are used on each edge of each beam. This corresponds to BEM models with 30, 50, 110 and 210 elements per beam, respectively. The BEM results, from the three BEM formulations, converge very quickly. Figure 8 shows the convergence of the

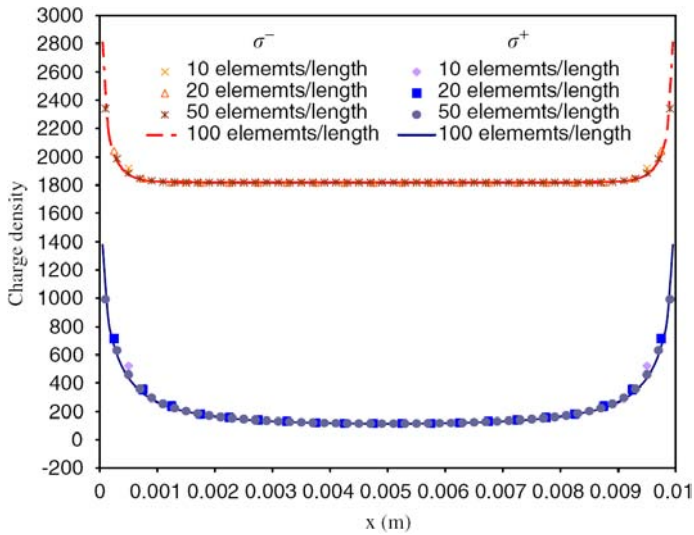

Fig. 8. (Color online) Convergence of the BEM results on the top beam, from the dual BIE (b), in the two beam model shown in Fig. 4. The upper curve is for σ^- and the lower for σ^+ (from Liu [2006]).

BEM results from the dual BIE (b) for the charge densities σ^- and σ^+. In fact, the model with just 10 elements along a beam length yields a value of σ^- at the middle of the lower surface of the top beam which agrees with the analytical solution ($\sigma^- = 1,818$ in this case) up to the first four digits. With an increase in the number of elements along the beam length, only the results near the two edges of a beam change, tending to infinity (due to the singularity of the field at the edges of each beam).

The effectiveness of the dual BIE approach in solving problems with extremely thin beams is demonstrated next. Table 2 presents a comparison of the charge densities on the top beam in the two beam capacitor model with the same set of parameters as in Fig. 8 except that h/L is varied from 0.1 to 10^{-16}. This time, 210 elements are used on each beam.

The regular BIE works very well until h/L reaches 10^{-8}, after which it degenerates. The high accuracy of the regular BIE can most likely be attributed to analytical integration of all integrals. This fact also likely delays the onset of degeneracy of the regular BIE for thin beam models. The dual BIEs (a) and (b) work very well until h/L reaches 10^{-14} and 10^{-16}, respectively. Below $h/L = 10^{-16}$, the ability of the double precision arithmetic used in the code, to represent small numbers, breaks down.

The condition numbers of the BEM systems of equations, using the three BIE formulations for the above cases, are plotted in Fig. 9. As expected, the condition number for the system with the regular BIE increases quickly as the thickness of a beam decreases, indicating the approach of this model towards degeneracy. The

Table 2. Comparison of regular BEM, dual BEM (a) and (b) and analytical solution for σ^- for the two beam problem.

h/L	Regular BIE		Dual BIE (a)		Dual BIE (b)		Analytical Soln.
	σ^-	σ^+	σ^-	σ^+	σ^-	σ^+	σ^-
10^{-1}	1,000	95.18	1,000	95.21	1,000	95.18	1,000
5×10^{-2}	1,333	103.0	1,333	103.0	1,333	103.4	1,333
10^{-2}	1,818	112.0	1,818	112.0	1,818	113.0	1,818
5×10^{-3}	1,905	113.5	1,905	113.5	1,905	114.8	1,905
10^{-3}	1,980	114.9	1,980	114.9	1,980	115.9	1,980
10^{-4}	1,998	115.4	1,998	115.4	1,998	115.7	1,998
10^{-5}	2,000	115.5	2,000	115.5	2,000	115.6	2,000
10^{-6}	2,000	115.5	2,000	115.5	2,000	115.6	2,000
10^{-7}	2,000	115.5	2,000	115.5	2,000	115.6	2,000
10^{-8}	2,003	114.5	2,000	115.5	2,000	115.6	2,000
10^{-9}	—	—	2,000	115.6	2,000	115.6	2,000
10^{-10}	—	—	2,000	115.6	2,000	115.6	2,000
10^{-11}	—	—	2,000	115.6	2,000	115.6	2,000
10^{-12}	—	—	2,000	115.6	2,000	115.6	2,000
10^{-13}	—	—	2,000	115.7	2,000	115.6	2,000
10^{-14}	—	—	2,000	115.2	2,000	115.6	2,000
10^{-15}	—	—	—	—	2,000	115.6	2,000
10^{-16}	—	—	—	—	2,000	115.6	2,000

Note: $\epsilon = 1, L = 0.01\,\text{m}, g/L = 0.1, V = +1, C = 0$. Mesh: 210 constant boundary elements per beam.

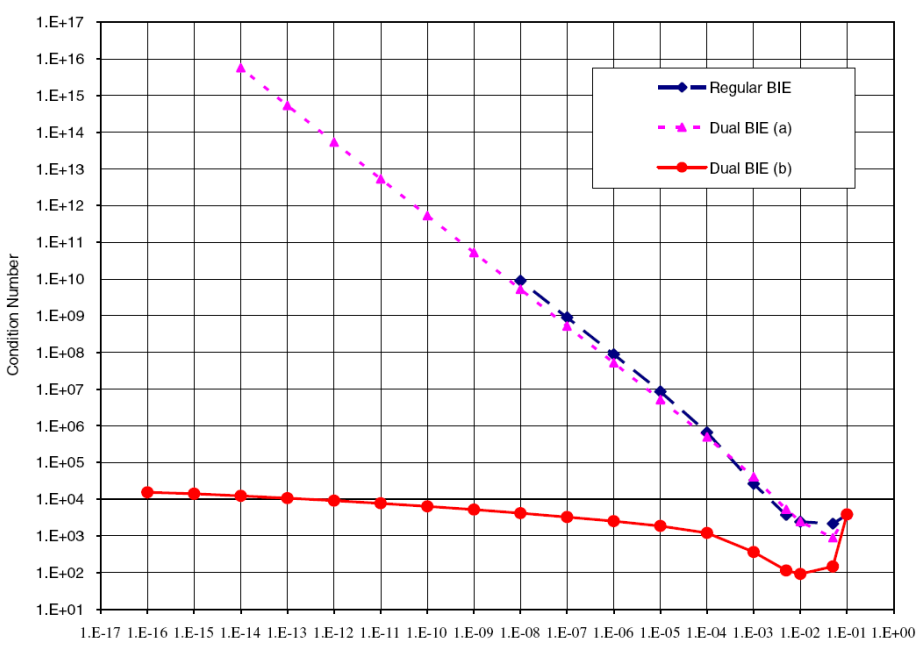

Fig. 9. (Color online) Condition numbers of the systems of equations from different BIE formulations, for the two beam model in Fig. 4 (from Liu [2006]).

condition number for the dual BIE (a) also increases to such a high level that the reliability of numerical results from this approach becomes questionable. This might be a result of the mismatch in the magnitudes of the coefficients since part of them come from the regular and others from the gradient BIE, which has a different order of singularity compared to the regular BIE. The condition numbers for the dual BIE (b) stay almost constant as the thickness of a beam decreases, reflecting the good conditioning of the system from this model which produces a more uniform distribution of the coefficients compared to the other methods. Good conditioning of a system is very important for the success of the fast multipole method (FMM) BEM (see Sec. 4.3) since this method requires convergence of solutions of linear systems of equations from iterative solvers. Thus, the dual BIE (b), which works well for both thick as well as extremely thin beams, appears to be an ideal candidate for the FMM.

A comb drive. A simplified comb-drive model, shown in Fig. 10, is studied next. The conventional BEM uses a direct solver (LAPACK) for solving the linear system. All the computations were done on a Pentium IV laptop PC with a 2.4 GHz CPU and 1 GB RAM. The comb drive models are built with the basic two parallel beam model shown in Fig. 4. The parameters used are: $\epsilon = 1, L = 0.01\,\text{m}$, $h = 0.0002\,\text{m}$, $g = 0.0003\,\text{m}, d = 0.0005\,\text{m}, V = +1, C = 0$. (Here d is the amount by which a lower beam (attached to the right vertical support beam) is horizontally offset with respect to the immediate upper one (attached to the left vertical support beam — see Fig. 10). Figure 10 shows a model with 17 beams (fingers). The two support beams

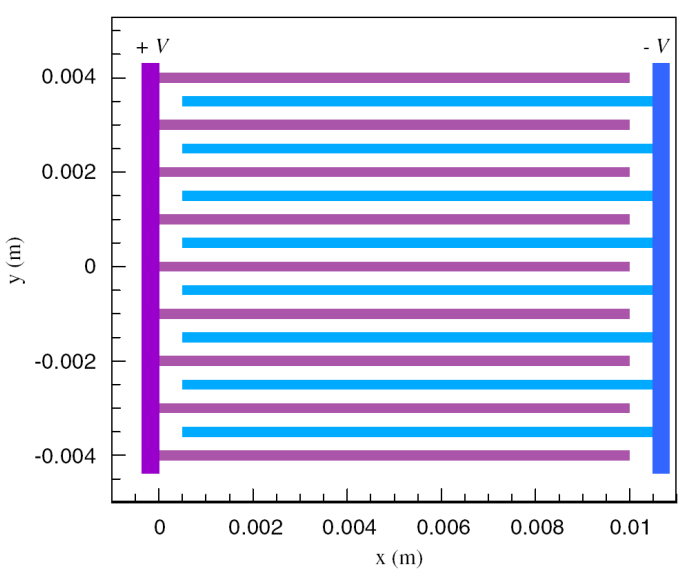

Fig. 10. (Color online) A simple comb drive model with 17 beams. The horizontal offset between the top beam and the next one below it is denoted as d (from Liu [2006]).

on the left and right sides in this figure are not modeled in the BEM discretization. 200 elements are used along the beam length and five elements on each edge (with a total number of elements equal to 410 for each beam). When more beams are added into the model, the number of elements along the beam length are increased to 400 (these results are not discussed in the present paper).

Figure 11 shows the computed charge densities on the center beam (beam 1) with negative voltage and the beam just below the center beam (beam 2) with positive voltage, for the model with 17 beams shown in Fig. 10. Due to the symmetry of the fields above and below each beam, the charge densities on the top and bottom surfaces of each beam are identical and thus only one field is plotted for each beam. The charge density on the two beams are also with the opposite sign and anti-symmetrical, as expected. Figure 12 is a plot of the charge densities on the bottom surface (σ^-) and the top surface (σ^+) of the top beam in Fig. 10. It should be noted that the fields in MEMS are much more complicated than those that the simple parallel beam models can represent, especially near the edges of the beams, due to the simplified geometries used in this study. The BEM code developed in

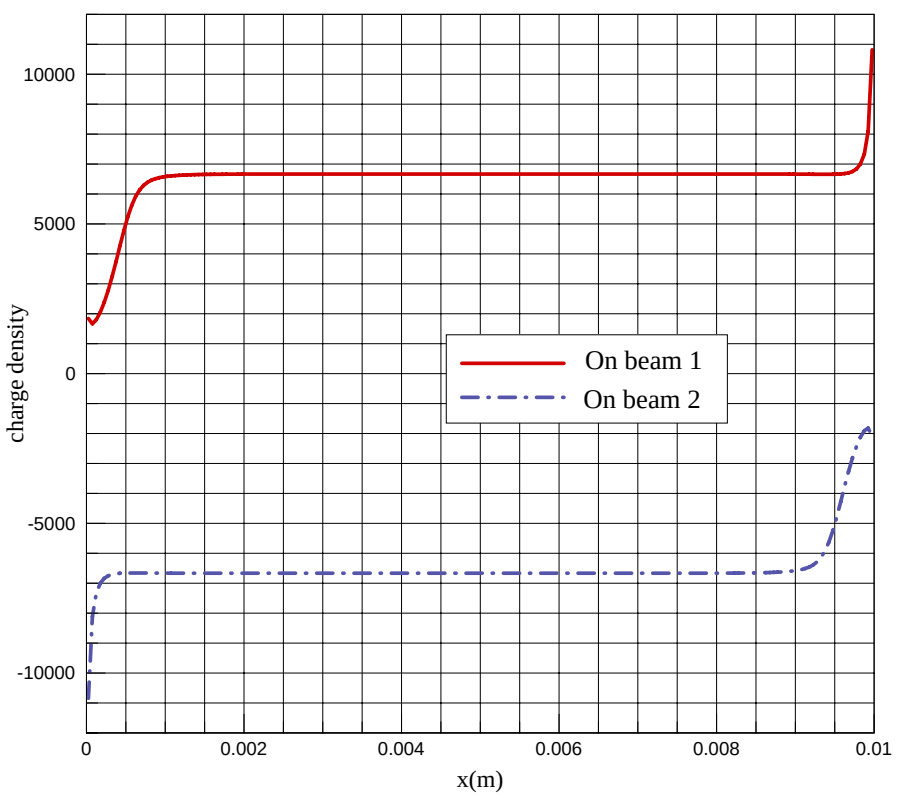

Fig. 11. (Color online) Charge densities on the center beams 1 and 2 (below the center beam) in the comb drive model in Fig. 10 (from Liu [2006]).

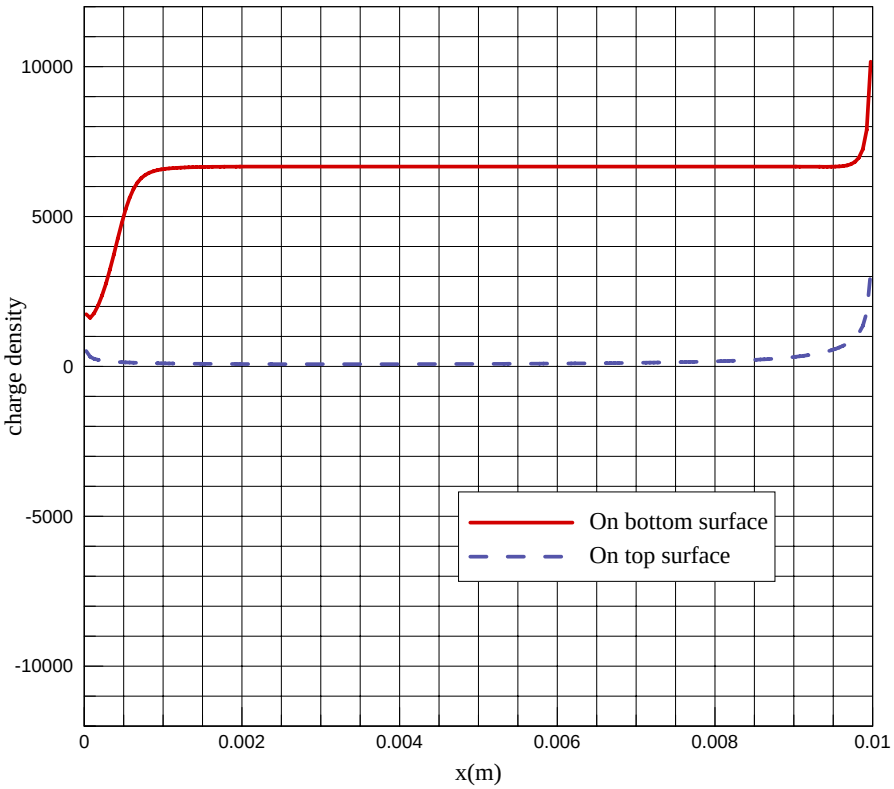

Fig. 12. (Color online) Charge densities on the surfaces of the top beam in the comb drive model in Fig. 10 (from Liu [2006]).

this study, however, can handle more complicated geometries of 2D comb drive models.

Much larger comb drive models (with up to 125 beams) are modeled with the FMM-BEM in Liu [2006]. It is evident from these preliminary studies that the dual BIE (b) is very effective in solving MEMS problems with thin beams and the FMM-BEM using the dual BIE (b) is very efficient for solving large-scale problems.

4. Recent Research

This section describes some recent research related to the BEM. The three topics addressed here are the BCM, the BNM and the FMM-BEM.

4.1. *Boundary contour method*

Derivations of the BCM and the HBCM, for 3D linear elasticity, together with numerical results for selected representative problems, are presented in this section.

4.1.1. *Basic equations*

A regularized form of the standard BIE [Rizzo (1967)], for 3D linear elasticity (Eq. (24)), is repeated below:

$$0 = \int_{\partial B} [U_{ik}(\mathbf{x},\mathbf{y})\sigma_{ij}(\mathbf{y}) - \Sigma_{ijk}(\mathbf{x},\mathbf{y})\{u_i(\mathbf{y}) - u_i(\mathbf{x})\}]\mathbf{e}_j \cdot d\mathbf{S}(\mathbf{y})$$

$$\equiv \int_{\partial B} \mathbf{F}_k \cdot d\mathbf{S}(\mathbf{y}). \tag{75}$$

The kernels $\mathbf{U}$ and $\mathbf{\Sigma}$ are given in Eqs. (17) and (20).

The first task is to show that the integrand vector $\mathbf{F}_k$ in Eq. (75) is divergence free (except at the point of singularity $\mathbf{x}$= $\mathbf{y}$). Writing in component form:

$$\mathbf{F}_k = F_{jk}\mathbf{e}_j = (\sigma_{ij}U_{ik} - \Sigma_{ijk}u_i)\mathbf{e}_j + \Sigma_{ijk}u_i(\mathbf{x})\mathbf{e}_j. \tag{76}$$

Taking the divergence of the above at a field point $\mathbf{y}$, one gets:

$$\nabla_{\mathbf{y}} \cdot \mathbf{F}_k = F_{jk,j}$$

$$= (\sigma_{ij}E_{ijk} - E_{ijk}\epsilon_{ij}) + (\sigma_{ij,j}U_{ik} - \Sigma_{ijk,j}u_i) + \Sigma_{ijk,j}u_i(\mathbf{x}), \tag{77}$$

where the Kelvin strain tensor $\mathbf{E}$ and the infinitesimal strain field $\boldsymbol{\epsilon}$ are:

$$E_{ijk} = (1/2)(U_{ik,j} + U_{jk,i}), \quad \epsilon_{ij} = (1/2)(u_{i,j} + u_{j,i}). \tag{78}$$

Let $(\mathbf{u}, \boldsymbol{\sigma})$ correspond to a body force free elastostatic state with the same elastic constants as the Kelvin solution. The stress and strain tensors, σ_{ij} and ϵ_{ij}, respectively, are related to each other through Hooke's law (27). The corresponding Kelvin stress and strain tensors Σ_{ijk} and E_{ijk}, respectively, are related by Hooke's law in exactly the same manner [Mukherjee (1982)]. As a consequence, the first expression on the RHS of Eq. (77) vanishes. Also, equilibrium in the absence of body forces demands that σ_{ij} be divergence free. The corresponding Kelvin stress tensor Σ_{ijk} is also divergence free, except at the point of singularity. Therefore, the second and third expressions on the RHS of (77) also vanish everywhere, except at the point of singularity. Thus, $\mathbf{F}_k$ in Eq. (77) is divergence free.

The divergence free property of $\mathbf{F}_k$ demonstrates the existence of vector potential functions $\mathbf{V}_k$ such that:

$$\mathbf{F}_k = \nabla \times \mathbf{V}_k. \tag{79}$$

As a consequence of Eq. (79), the surface integral in Eq. (75) over any open surface patch $S \in \partial B$, can be converted to a contour integral around the bounding curve C of S, by applying Stokes' theorem, i.e.,

$$\int_S \mathbf{F}_k \cdot d\mathbf{S} = \oint_C \mathbf{V}_k \cdot d\mathbf{r}. \tag{80}$$

Stokes' theorem is valid under very general conditions. The closed curve C and the open surface S need not be flat — they only need to be piecewise smooth.

4.1.2. *Interpolation functions*

Since the vector $\mathbf{F}_k$ contain the unknown fields $\mathbf{u}$ and $\boldsymbol{\sigma}$, interpolation functions must be chosen for these variables, and potential functions derived for each linearly independent interpolation function, in order to determine the vectors $\mathbf{V}_k$. Also, since the kernels in Eq. (75) are functions only of $z_k = y_k - x_k$ (and not of the source and field coordinates separately), these interpolation functions must also be written in the coordinates z_k in order to determine the potential vectors $\mathbf{V}_k$. Finally, these interpolation functions are global in nature and are chosen to satisfy, a priori, the Navier–Cauchy equations of equilibrium. (Such functions are called Trefftz functions.) The weights, in linear combinations of these interpolation functions, however, are defined piecewise on boundary elements.

Quadratic interpolation functions are used in this work. With (as stated before):

$$z_k = y_k - x_k, \tag{81}$$

one has, on a boundary element:

$$u_i = \sum_{\alpha=1}^{27} \beta_\alpha \bar{u}_{\alpha i}(y_1, y_2, y_3) = \sum_{\alpha=1}^{27} \hat{\beta}_\alpha(x_1, x_2, x_3)\bar{u}_{\alpha i}(z_1, z_2, z_3), \tag{82}$$

$$\sigma_{ij} = \sum_{\alpha=1}^{27} \beta_\alpha \bar{\sigma}_{\alpha ij}(y_1, y_2, y_3) = \sum_{\alpha=1}^{27} \hat{\beta}_\alpha(x_1, x_2, x_3)\bar{\sigma}_{\alpha ij}(z_1, z_2, z_3), \tag{83}$$

where $\bar{u}_{\alpha i}, \bar{\sigma}_{\alpha ij}$ (with $i, j = 1, 2, 3$ and $\alpha = 1, 2, \ldots, 27$) are the interpolation functions and β_α are the weights in the linear combinations of the interpolation functions. Each boundary element has, associated with it, 27 constants β_α that will be related to physical variables on that element. This set β differs from one element to the next.

The displacement interpolation functions for $\alpha = 1, 2, 3$ are constants, those for $\alpha = 4, \ldots, 12$ are of first degree in y_k and those for $\alpha = 13, \ldots, 27$ are of second degree in y_k. There are a total of 27 linearly independent (vector) interpolation functions $\bar{\mathbf{u}}_\alpha$. The interpolation functions for the stresses are obtained from those for the displacements through the use of Hooke's law. The interpolation functions $\bar{u}_{\alpha i}$ and $\bar{\sigma}_{\alpha ij}$ are given in Tables 3 and 4, respectively.

It is easy to show that the coordinate transformation (81) results in the constants $\hat{\beta}_j$ being related to the constants β_α as follows:

$$\hat{\beta}_i = \sum_{\alpha=1}^{27} S_{i\alpha}(x_1, x_2, x_3)\beta_\alpha, \quad i = 1, 2, 3, \tag{84}$$

$$\hat{\beta}_k = \sum_{\alpha=1}^{27} R_{n\alpha}(x_1, x_2, x_3)\beta_\alpha, \quad k = 4, 5, \ldots, 12, \;\; n = k - 3, \tag{85}$$

$$\hat{\beta}_\alpha = \beta_\alpha, \quad \alpha = 13, 14, \ldots, 27, \tag{86}$$

Table 3. Trefftz functions $\bar{u}_{\alpha i}$ for interpolating displacements. $\bar{u}_{\alpha i}$ for $\alpha = 1, 2, 3$ are constants, $\alpha = 4, 5, \ldots, 12$ are linear in y_k and $\alpha = 13, 14, \ldots, 27$ are quadratic in y_k. $k_1 = -4(1-\nu)$, $k_2 = -2(1-2\nu), k_3 = k_1 - 4$.

$\bar{u}_{\alpha i}$	1	2	3	4	5	6	7
$i=1$	1	0	0	y_1	0	0	y_2
$i=2$	0	1	0	0	y_1	0	0
$i=3$	0	0	1	0	0	y_1	0
$\bar{u}_{\alpha i}$	8	9	10	11	12	13	14
$i=1$	0	0	y_3	0	0	y_1^2	y_2^2
$i=2$	y_2	0	0	y_3	0	$k_1 y_1 y_2$	$k_2 y_1 y_2$
$i=3$	0	y_2	0	0	y_3	0	0
$\bar{u}_{\alpha i}$	15	16	17	18	19	20	21
$i=1$	$k_2 y_1 y_2$	$k_1 y_1 y_2$	$k_1 y_1 y_3$	$k_2 y_1 y_3$	y_3^2	y_1^2	0
$i=2$	y_1^2	y_2^2	0	0	0	0	y_2^2
$i=3$	0	0	y_3^2	y_1^2	$k_2 y_1 y_3$	$k_1 y_1 y_3$	$k_1 y_2 y_3$
$\bar{u}_{\alpha i}$	22	23	24	25	26	27	
$i=1$	0	0	0	$y_2 y_3$	0	0	
$i=2$	y_3^2	$k_2 y_2 y_3$	$k_1 y_2 y_3$	0	$y_1 y_3$	0	
$i=3$	$k_2 y_2 y_3$	y_2^2	y_3^2	0	0	$y_1 y_2$	

where

$$S_{i\alpha} = \bar{u}_{\alpha i}(x_1, x_2, x_3), \quad i = 1, 2, 3, \;\; \alpha = 1, 2, \ldots, 27,$$

$$R_{k\alpha} = \left.\frac{\partial \bar{u}_{\alpha \ell}(y_1, y_2, y_3)}{\partial y_j}\right|_{(x_1, x_2, x_3)}, \quad k = 1, 2, \ldots, 9, \;\; \alpha = 1, 2, \ldots, 27,$$

with $j = 1 + \lfloor \frac{k-1}{3} \rfloor$ and $\ell = k - 3j + 3$. Here, the symbol $\lfloor n \rfloor$, called the floor of n, denotes the largest integer less than or equal to n.

It is useful to note that the matrices $\mathbf{S}$ and $\mathbf{R}$ are functions of only the source point coordinates (x_1, x_2, x_3).

4.1.3. *Boundary elements*

The BCM is a perfectly general approach that can be used to solve any well-posed problem in linear elasticity. A departure from the usual BEM, however, is that a set of primary physical variables a_k are first chosen at appropriate points on a boundary element. Some of these would be specified as boundary conditions and the rest would be unknown in a given problem. The first step in the BCM solution procedure is to determine the unspecified primary physical variables in terms of those that are prescribed as boundary conditions. Once all the primary physical variables are known, the rest of the physical variables (the secondary ones) are obtained at a simple postprocessing step. Also, unlike in the standard BEM, it is

Table 4. Trefftz functions $\bar{\sigma}_{\alpha ij}$ for interpolating stresses. For $\alpha = 1, 2, 3$, $\bar{\sigma}_{\alpha ij} = 0$, for $\alpha = 4, 5, \ldots, 12$, $\bar{\sigma}_{\alpha ij}$ are constants, and for $\alpha = 13, 14, \ldots, 27$, $\bar{\sigma}_{\alpha ij}$ are linear in y_k. $k_1 = -4(1-\nu)$, $k_2 = -2(1-2\nu)$, $k_3 = k_1 - 4$.

$\bar{\sigma}_{\alpha ij/\mu}$	1	2	3	4	5	6	7
$i,j = 1,1$	0	0	0	k_1/k_2	0	0	0
$i,j = 1,2$	0	0	0	0	1	0	1
$i,j = 1,3$	0	0	0	0	0	1	0
$i,j = 2,2$	0	0	0	λ/μ	0	0	0
$i,j = 2,3$	0	0	0	0	0	0	0
$i,j = 3,3$	0	0	0	λ/μ	0	0	0
$\bar{\sigma}_{\alpha ij/\mu}$	8	9	10	11	12	13	14
$i,j = 1,1$	λ/μ	0	0	0	λ/μ	$-k_1 y_1$	$-4\nu y_1$
$i,j = 1,2$	0	0	0	0	0	$k_1 y_2$	$4\nu y_2$
$i,j = 1,3$	0	0	1	0	0	0	0
$i,j = 2,2$	k_1/k_2	0	0	0	λ/μ	$k_3 y_1$	$k_1 y_1$
$i,j = 2,3$	0	1	0	1	0	0	0
$i,j = 3,3$	λ/μ	0	0	0	k_1/k_2	$-4\nu y_1$	$-4\nu y_1$
$\bar{\sigma}_{\alpha ij/\mu}$	15	16	17	18	19	20	21
$i,j = 1,1$	$k_1 y_2$	$k_3 y_2$	$k_3 y_3$	$k_1 y_3$	$-4\nu y_1$	$-k_1 y_1$	$-4\nu y_2$
$i,j = 1,2$	$4\nu y_1$	$k_1 y_1$	0	0	0	0	0
$i,j = 1,3$	0	0	$k_1 y_1$	$4\nu y_1$	$4\nu y_3$	$k_1 y_3$	0
$i,j = 2,2$	$-4\nu y_2$	$-k_1 y_2$	$-4\nu y_3$	$-4\nu y_3$	$-4\nu y_1$	$-4\nu y_1$	$-k_1 y_2$
$i,j = 2,3$	0	0	0	0	0	0	$k_1 y_3$
$i,j = 3,3$	$-4\nu y_2$	$-4\nu y_2$	$-k_1 y_3$	$-4\nu y_3$	$k_1 y_1$	$k_3 y_1$	$k_3 y_2$
$\bar{\sigma}_{\alpha ij/\mu}$	22	23	24	25	26	27	
$i,j = 1,1$	$-4\nu y_2$	$-4\nu y_3$	$-4\nu y_3$	0	0	0	
$i,j = 1,2$	0	0	0	y_3	y_3	0	
$i,j = 1,3$	0	0	0	y_2	0	y_2	
$i,j = 2,2$	$-4\nu y_2$	$k_1 y_3$	$k_3 y_3$	0	0	0	
$i,j = 2,3$	$4\nu y_3$	$4\nu y_2$	$k_1 y_2$	0	y_1	y_1	
$i,j = 3,3$	$k_1 y_2$	$-4\nu y_3$	$-k_1 y_3$	0	0	0	

particularly easy to obtain surface variables, such as stresses and curvatures, in the BCM. Surface stresses are discussed later in this section.

The number of primary physical variables on a boundary element must match the number of artificial variables β_k associated with it, in order that the transformation matrix T relating the vectors $\mathbf{a}$ and $\boldsymbol{\beta}$ on element m is square. This relationship is expressed as:

$$\overset{m}{a} = \overset{mm}{T}\beta \ . \tag{87}$$

Of course, the matrix T must be invertible. The issue of invertibility of T is discussed in Nagarajan *et al.* [1996].

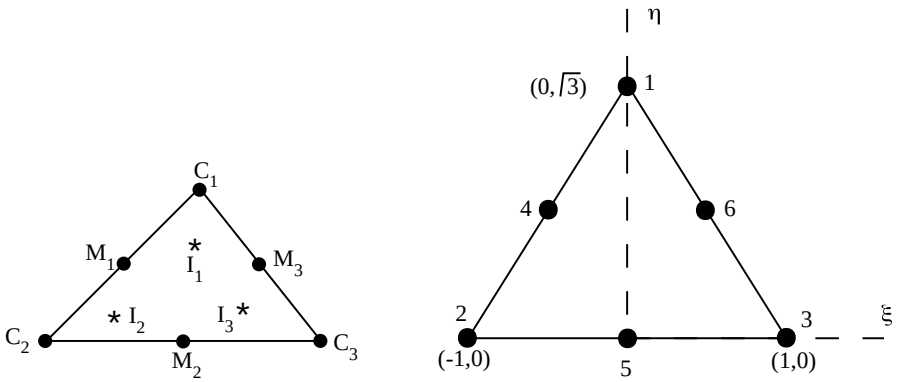

Fig. 13. (a) The CIM9 boundary element. (b) Intrinsic coordinates (from Mukherjee *et al.* [1997]).

The CIM9 boundary element, shown in Fig. 13(a), is used in the present work. The displacement $\mathbf{u}$ is the primary physical variable at the three corner nodes C_i and the three midside nodes M_i, while tractions are primary variables at the internal nodes I_i. Thus, there are a total of 27 primary physical variables. The BCM equations are collocated at the six peripheral nodes as well as at the centroid of the element. In a typical discretization procedure, some of the peripheral nodes may lie on corners or edges, while the internal nodes are always located at regular points where the boundary ∂B is locally smooth. It is of obvious advantage to deal only with displacement components, that are always continuous, on edges and corners, while having traction components only at regular boundary points. This approach eliminates the well-known problems associated with modeling of corners and edges in the usual BEM.

The boundary elements, in general, are curved (quadratic) with their shapes defined by the six points $C_k, M_k, k = 1, 2, 3$. (see Fig. 13). The relative coordinates z_i (see Eq. (81)) of a point on one of the sides of a triangle are written as:

$$z_i = N_k(\xi, \eta) z_i^k, \quad i = 1, 2, 3; \;\; k = 1, 2, \ldots, 6, \tag{88}$$

where z_i^k are the relative coordinates of the peripheral nodes $1, 2, \ldots, 6$ on the CIM9 element (see Fig. 13), and ξ and η are intrinsic coordinates. The shape functions are:

$$\begin{aligned} N_k &= (2L_k - 1)L_k, \quad k = 1, 2, 3; \text{ no sum over } k \\ N_4 &= 4L_1L_2, \quad N_5 = 4L_2L_3, \quad N_6 = 4L_1L_3, \end{aligned} \tag{89}$$

with

$$\begin{aligned} L_1 &= \eta/\sqrt{3}, \\ L_2 &= (1/2)(1 - \xi) - \eta/(2\sqrt{3}), \\ L_3 &= (1/2)(1 + \xi) - \eta/(2\sqrt{3}). \end{aligned} \tag{90}$$

The reference triangle in intrinsic coordinates is shown in Fig. 13(b).

The unit outward normal to a boundary element, at a point on it, is given by:

$$\mathbf{n} = \frac{(\frac{\partial \mathbf{r}}{\partial \xi} \times \frac{\partial \mathbf{r}}{\partial \eta})}{|\frac{\partial \mathbf{r}}{\partial \xi} \times \frac{\partial \mathbf{r}}{\partial \eta}|}, \tag{91}$$

where $\mathbf{r} = z_i \mathbf{e}_i$. It is important to point out that elements of the transformation matrix T in Eq. (87) contain components of the normal $\mathbf{n}$ at the points I_1, I_2, I_3 of the CIM9 element shown in Fig. 13(a).

4.1.4. *Vector potentials*

The homogeneous nature of the Kelvin kernels is exploited in deriving the potential functions. From Eqs. (20) and (17), it is clear that both Σ_{ijk} and U_{ik} are ratios of homogeneous polynomials and are, therefore, homogeneous. Here, $\mathbf{\Sigma}$ is of degree -2 and $\mathbf{u}$ is of degree -1. If an interpolation function is of degree n, then the resulting force vector $\mathbf{F}_{\alpha k}$ (which is $\mathbf{F}_k$ corresponding to the αth interpolation function) is of degree $n-2$. In this work, interpolation functions with $n = 0, 1, 2$ are used (see Tables 3 and 4).

The nonsingular case: $n \neq 0$. The homogeneous nature of the Kelvin kernels greatly facilitates the use of an inversion integral to calculate the inverse curl of a given vector field of zero divergence [Kaplan (1984)]. Thus:

$$\mathbf{F}_{\alpha k} = \boldsymbol{\nabla} \times \mathbf{V}_{\alpha k} \Rightarrow \mathbf{V}_{\alpha k}(z_1, z_2, z_3) = \left[\int_0^1 t \mathbf{F}_{\alpha k}(tz_1, tz_2, tz_3) dt \right] \times \mathbf{r}, \tag{92}$$

where $\mathbf{r} = z_i \mathbf{e}_i$.

Because of the homogeneous nature of $\mathbf{F}_{\alpha k}$:

$$\mathbf{F}_{\alpha k}(tz_1, tz_2, tz_3) = t^{n-2} \mathbf{F}_{\alpha k}(z_1, z_2, z_3). \tag{93}$$

Therefore, for the nonsingular case $n \neq 0$ Eqs. (92) and (93) yield:

$$\mathbf{V}_{\alpha k}(z_1, z_2, z_3) = (1/n) \mathbf{F}_{\alpha k}(z_1, z_2, z_3) \times \mathbf{r}. \tag{94}$$

The singular case: $n = 0$. The singular case ($n = 0$) corresponds to constant displacement interpolation functions $\bar{u}_{\alpha i} = \delta_{\alpha i}$, $\alpha = 1, 2, 3$; $i = 1, 2, 3$, (where $\boldsymbol{\delta}$ is the Kronecker delta — see Table 3). Referring to Eq. (75), one must now deal with the term $\Sigma_{\alpha jk}$ given in Eq. (20). The expression for $\Sigma_{ijk} \mathbf{e}_j$ can be partitioned into three terms, each of which is divergence free [Nagarajan *et al.* (1996)]. One writes:

$$\begin{aligned} -\Sigma_{\alpha jk} \mathbf{e}_j = & \frac{1}{8\pi(1-\nu) r^2} [3 r_{,\alpha} r_{,j} r_{,k} - r_{,j} \delta_{\alpha k}] \mathbf{e}_j \\ & + \frac{1-2\nu}{8\pi(1-\nu) r^2} [r_{,\alpha} \delta_{jk} - r_{,k} \delta_{\alpha j}] \mathbf{e}_j + \frac{r_{,j} \delta_{\alpha k}}{4\pi r^2} \mathbf{e}_j. \end{aligned} \tag{95}$$

Each of the above three terms on the RHS of Eq. (95) is divergence free and can be written as the curl of a potential function. For the first two terms, one has [Nagarajan *et al.* (1996)]:

$$\frac{1}{r^2}[3r_{,\alpha}r_{,j}r_{,k} - r_{,j}\delta_{\alpha k}]\mathbf{e}_j = \boldsymbol{\nabla} \times \left[\epsilon_{kmj}\frac{r_{,\alpha}r_{,m}}{r}\mathbf{e}_j\right], \tag{96}$$

$$\frac{1}{r^2}[r_{,\alpha}\delta_{jk} - r_{,k}\delta_{\alpha j}]\mathbf{e}_j = \boldsymbol{\nabla} \times \left[\frac{\epsilon_{\alpha km}}{r}\mathbf{e}_m\right], \tag{97}$$

where $\boldsymbol{\epsilon}$ is the alternating tensor.

It is well known that the solid angle Ω subtended at the source point $\mathbf{x}$ by the open surface S has the expression:

$$\Omega = \int_S \frac{r_{,j}}{r^2}\mathbf{e}_j \cdot d\mathbf{S} = \int_S \frac{\mathbf{r} \cdot d\mathbf{S}}{r^3}. \tag{98}$$

Therefore, the surface integral of the third term on the RHS of (95) over S equals $(\Omega/4\pi)\delta_{\alpha k}$. While it is possible to convert the surface integral in (98) to a line integral [Nagarajan *et al.* (1996)], use of this line integral has proved to lack robustness in general numerical computations involving 3D bodies of complex shapes. Therefore, the solid angle Ω is computed as a surface integral according to Eq. (98). *This is the only surface integral that is ever computed in the BCM.* Fortunately, the solid angle is a purely geometrical quantity that can be computed easily as a surface integral in a robust fashion. It is also noted here that algebraic expressions exist for the solid angle for the special case when S is a plane.

4.1.5. *Final BCM equations*

Use of the interpolating functions for displacements and stresses from Tables 3 and 4 respectively, together with Eqs. (81)–(87) and (94)–(98) transforms the regularized BIE (75) into a regularized boundary contour equation (BCE) that can be collocated (as for the BEM) at any boundary (surface) point — including that on edges and corners, as long as the displacement is continuous there. This equation is:

$$\begin{aligned} 0 = \frac{1}{2}\sum_{m=1}^{M}\sum_{\alpha=13}^{27}\left[\oint_{L_m}(\bar{\sigma}_{\alpha ij}U_{ik} - \bar{u}_{\alpha i}\Sigma_{ijk})\epsilon_{jnt}z_n dz_t\right]\left[\overset{m}{T}{}^{-1}\overset{m}{a}\right]_\alpha \\ + \sum_{m=1}^{M}\sum_{\alpha=4}^{12}\left[\oint_{L_m}(\bar{\sigma}_{\alpha ij}U_{ik} - \bar{u}_{\alpha i}\Sigma_{ijk})\epsilon_{jnt}z_n dz_t\right]\left[R\overset{m}{T}{}^{-1}\overset{m}{a}\right]_{\alpha-3} \\ + \sum_{\substack{m=1 \\ m\notin\mathcal{S}}}^{M}\sum_{\alpha=1}^{3}\left[\oint_{L_m}D_{\alpha jk}dz_j\right]\left[S\left(\overset{m}{T}{}^{-1}\overset{m}{a} - \overset{P}{T}{}^{-1}\overset{P}{a}\right)\right]_\alpha, \end{aligned} \tag{99}$$

with

$$\oint_{L_m} D_{\alpha jk} dz_j = -\int_{S_m} \Sigma_{\alpha jk} \mathbf{e}_j \cdot d\mathbf{S}$$
$$= \frac{1}{8\pi(1-\nu)} \oint_{L_m} \epsilon_{kij} \frac{r_{,\alpha} r_{,i}}{r} dz_j$$
$$+ \frac{1-2\nu}{8\pi(1-\nu)} \oint_{L_m} \epsilon_{\alpha kj} \frac{1}{r} dz_j + \frac{\Omega}{4\pi} \delta_{\alpha k}. \tag{100}$$

Here L_m is the bounding contour of the surface element S_m. Also, $\overset{m}{T}$ and $\overset{m}{a}$ are the transformation matrix and primary physical variable vectors on element m, $\overset{P}{T}$ and $\overset{P}{a}$ are the same quantities evaluated on any element that belongs to the set $\mathcal{S}$ of elements that contain the source point $\mathbf{x}$, and ϵ_{ijk} is the usual alternating symbol. Finally, M is the total number of elements.

This method of integrating Σ_{ijk} has been presented before, using spherical coordinates, in Ghosh and Mukherjee [1987]. Also, this result in Eq. (100) has been independently derived [Mantič (1993)] with the use of the tangential differential operator:

$$D_{ij}(f(\mathbf{y})) \equiv n_i(\mathbf{y}) f_{,j}(\mathbf{y}) - n_j(\mathbf{y}) f_{,i}(\mathbf{y}). \tag{101}$$

Equations are assembled by using the fact that displacements are continuous across elements. The final result is:

$$Ka = 0, \tag{102}$$

which is written as:

$$Ax = By, \tag{103}$$

where $\mathbf{x}$ contains the unknown and $\mathbf{y}$ the known (from the boundary conditions) values of the primary physical variables on the surface of the body. Once these equations are solved, the vector $\mathbf{a}$ is completely known. Now, at a postprocessing step, $\overset{m}{\beta}_\alpha$ can be obtained on each boundary element from Eq. (87).

4.1.6. *Global equations and unknowns*

The global system Eq. (103) generally leads to a rectangular matrix A. The system of linear equations is usually overdetermined but always consistent. A count of equations and unknowns is given below.

For any general polyhedron, Euler's theorem states that:

$$F + V = E + 2, \tag{104}$$

where F is the number of faces (here the number of elements), V is the number of vertices (here the number of corner nodes) and E is the number of edges (here $1.5F$

for triangular elements). Thus, one has:

$$\text{Number of corner nodes} = (1/2)\ \text{Number of elements} + 2. \tag{105}$$

Also, a CIM9 element has 1.5 midside nodes (i.e., 3 midside nodes per element, each of which is shared by two neighboring elements).

One is now in a position to count the number of (vector) equations and unknowns in the global system (103). In a CIM9 element, the BCM equations are enforced at all the peripheral nodes and also at the centroid of the element. Thus, for M boundary elements, one has M equations at the centroids, $1.5M$ equations at the midside nodes and $0.5M + 2$ at the corner nodes, for a total of $3M + 2$ equations. For a Dirichlet problem, in which all the displacements are prescribed on ∂B, there are a total of $3M$ vector unknowns — the tractions at the nodes interior to the elements. One therefore has two extra vector (six extra scalar) equations. This is the worst-case scenario in the sense that for mixed boundary value problems, the number of equations remains the same while the number of unknowns decreases. For example, for a Neumann problem in which all the tractions are prescribed on ∂B, one only has $2M + 2$ (vector) unknowns (displacements at the peripheral nodes of the elements). Of course, a Neumann problem is ill-posed since rigid body displacements of the body are not constrained.

In summary, use of the CIM9 element results in overdetermined, consistent linear systems for well-posed problems in linear elasticity.

4.1.7. *Surface displacements, stresses and curvatures*

A useful consequence of using global shape functions is that, once the standard BCM equations are solved, it is easy to obtain displacements, stresses and curvatures at a regular off-contour boundary point (ROCBP) on the bounding surface of a body. Here, a point at an edge or corner is called an irregular point while at a regular point the boundary is locally smooth. Also, a regular boundary point can lie on or away from a boundary contour. The former is called a regular contour point (RCP), the latter a ROCBP. A point inside a body is called an internal point.

First, one obtains $\overset{m}{\beta}_\alpha$ from Eq. (87), then uses Eqs. (84) and (85) to get $\hat{\beta}^m_\alpha, \alpha = 1, 2, \ldots, 12$. The curvatures, which are piecewise constant on each boundary element, are obtained by direct differentiation of Eq. (82). Finally, one has the following results:

Surface displacements.

$$[u_i(\mathbf{x})] = \begin{bmatrix} \hat{\beta}_1 \\ \hat{\beta}_2 \\ \hat{\beta}_3 \end{bmatrix}_{\mathbf{x}}. \tag{106}$$

Surface displacement gradients.

$$[u_{i,j}(\mathbf{x})] = \begin{bmatrix} \hat{\beta}_4 & \hat{\beta}_7 & \hat{\beta}_{10} \\ \hat{\beta}_5 & \hat{\beta}_8 & \hat{\beta}_{11} \\ \hat{\beta}_6 & \hat{\beta}_9 & \hat{\beta}_{12} \end{bmatrix}_{\mathbf{x}}. \tag{107}$$

Surface curvatures.

$$\left[\frac{\partial^2 u_1}{\partial x_i \partial x_j}\right] = \begin{bmatrix} 2(\beta_{13}+\beta_{20}) & k_2\beta_{15}+k_1\beta_{16} & k_1\beta_{17}+k_2\beta_{18} \\ & 2\beta_{14} & \beta_{25} \\ \text{symmetric} & & 2\beta_{19} \end{bmatrix}, \tag{108}$$

$$\left[\frac{\partial^2 u_2}{\partial x_i \partial x_j}\right] = \begin{bmatrix} 2\beta_{15} & k_1\beta_{13}+k_2\beta_{14} & \beta_{26} \\ & 2(\beta_{16}+\beta_{21}) & k_2\beta_{23}+k_1\beta_{24} \\ \text{symmetric} & & 2\beta_{22} \end{bmatrix}, \tag{109}$$

$$\left[\frac{\partial^2 u_3}{\partial x_i \partial x_j}\right] = \begin{bmatrix} 2\beta_{18} & \beta_{27} & k_2\beta_{19}+k_1\beta_{20} \\ & 2\beta_{23} & k_1\beta_{21}+k_2\beta_{22} \\ \text{symmetric} & & 2(\beta_{17}+\beta_{24}) \end{bmatrix}, \tag{110}$$

with $k_1 = -4(1-\nu)$ and $k_2 = -2(1-2\nu)$.

Equation (107) gives the displacement gradients at a surface point $\mathbf{x}$. Hooke's law would then give the stress $\sigma_{ij}(\mathbf{x})$. An alternative approach is to use Eq. (83) together with all the β_α on an element.

It should be noted that the approach, described above, cannot be used to find internal stresses since the constants $\overset{m}{\beta}_\alpha$ are only meaningful on the boundary of a body. Therefore, an internal point representation of the differentiated BCE, for the internal displacement gradients $u_{i,j}(p)$, is necessary. It is also of interest to examine the limiting process of a differentiated BCE as an internal point $\boldsymbol{\xi}$ (also denoted as p) approaches a boundary point $\mathbf{x}$ (also denoted as P). This issue has been of interest in the BEM community in the context of the standard BIE and the HBIE [Martin and Rizzo (1996); Cruse and Richardson (1996); Martin *et al.* (1998); Mukherjee and Mukherjee (2001)]. Further, the HBCE must be understood if one wishes to collocate the HBCE as the primary integral equation, as may be necessary, for example, in applications such as fracture mechanics, symmetric Galerkin formulations [Sutradhar *et al.* (2008)] or adaptive analysis. This topic is the subject of the next subsection.

4.1.8. *Regularized hypersingular BIE*

A HBIE can be obtained by differentiating the standard BIE *at an internal point*, with respect to the coordinates of this internal source point. Equation (35) is regularized and contains, at most, weakly singular integrals.

Martin *et al.* [1998] (Appendix II2, p. 905); (see, also, Mukherjee and Mukherjee [2001]) have proved that (35) can be collocated even at an edge or corner point $\mathbf{x}$ on the surface of a 3D body, provided that the displacement and stress fields in (35) satisfy smoothness requirements as discussed in Mukherjee and Mukherjee [2005].

4.1.9. *Regularized hypersingular BCE*

The regularized HBIE (35) can be converted to a regularized (HBCE). Details are available in Mukherjee and Mukherjee [1998] and are given below.

The first step is to transform Eq. (35) into a boundary contour form. The integrands in Eq. (35), without $n_j(\mathbf{y})dS(\mathbf{y})$, are first evaluated at an internal field point q very near Q (i.e., on a surface $\partial\hat{B}$ inside the body, very near and parallel to ∂B), the derivatives are transferred from the kernels to the quantities inside the square brackets by the product rule, and then the limit $q \to Q$ is taken again. This is possible since the integrals in Eq. (35) are regular. The result is:

$$\begin{aligned} 0 = &\int_{\partial B} [U_{ik}(\mathbf{x},\mathbf{y})[\sigma_{ij}(\mathbf{y}) - \sigma_{ij}(\mathbf{x})] - \Sigma_{ijk}(\mathbf{x},\mathbf{y})(u_i(\mathbf{y}) - u_i^{(L)})]_{,n}\, n_j(\mathbf{y}) dS(\mathbf{y}) \\ &- \int_{\partial B} [U_{ik}(\mathbf{x},\mathbf{y})\sigma_{ij,n}(\mathbf{y}) - \Sigma_{ijk}(\mathbf{x},\mathbf{y})[u_{i,n}(\mathbf{y}) - u_{i,n}(\mathbf{x})]] \\ &\times n_j(\mathbf{y}) dS(\mathbf{y}), \quad \mathbf{x},\mathbf{y} \in \partial B, \end{aligned} \tag{111}$$

where

$$u_i^{(L)} = u_i(\mathbf{x}) + u_{i,\ell}(\mathbf{x})(y_\ell - x_\ell).$$

Note also that:

$$u_{i,n}^{(L)} = u_{i,n}(\mathbf{x}).$$

Therefore, the affine displacement field $u_i^{(L)}$ gives the stress field $\sigma_{ij}(\mathbf{x})$, so that the stress field $\sigma_{ij}(\mathbf{y}) - \sigma_{ij}(\mathbf{x})$ is obtained from the displacement field $u_i(\mathbf{y}) - u_i^{(L)}$.

Using the identity [Nagarajan *et al.* (1996)]:

$$\mathbf{v}_{,n} = \nabla \times (\mathbf{v} \times \mathbf{e}_n) \tag{112}$$

(which is valid if the vector field $\mathbf{v}$ is divergence-free) and Stokes' theorem, the first integral on the RHS of Eq. (111), over S_m, is converted to the contour integral:

$$I_1 = \oint_{L_m} [U_{ik}(\mathbf{x},\mathbf{y})[\sigma_{ij}(\mathbf{y}) - \sigma_{ij}(\mathbf{x})] - \Sigma_{ijk}(\mathbf{x},\mathbf{y})[u_i(\mathbf{y}) - u_i^{(L)}]]\epsilon_{jnt} dz_t. \tag{113}$$

In the above, S_m and L_m are the surface and bounding contour, respectively, of the mth boundary element.

An explicit form of Eq. (113) is derived in Appendix A of this section.

Next, it is noted from Eqs. (106) and (84) that:

$$u_{i,n}(\mathbf{x}) = \left[S_{,N} \overset{P}{\beta} \right]_i, \tag{114}$$

where, $N \equiv \partial/\partial x_n$.

Further, as proved in Appendix B of this section:

$$u_{i,n}(\mathbf{y}) = \left[S_{,N} \overset{m}{\beta} \right]_i + \sum_{\alpha=4}^{12} \left[R_{,N} \overset{m}{\beta} \right]_{\alpha-3} \bar{u}_{\alpha i}(z_1, z_2, z_3). \tag{115}$$

Now, the second integral on the RHS of Eq. (111) (called I_2) is written as:

$$\begin{aligned} I_2 = &- \int_{\partial B} [U_{ik}(\mathbf{x}, \mathbf{y}) \sigma_{ij,n}(\mathbf{y}) - \Sigma_{ijk}(\mathbf{x}, \mathbf{y}) u_{i,n}(\mathbf{y})] n_j(\mathbf{y}) dS(\mathbf{y}) \\ &- u_{i,n}(\mathbf{x}) \int_{\partial B} \Sigma_{ijk}(\mathbf{x}, \mathbf{y}) n_j(\mathbf{y}) dS(\mathbf{y}). \end{aligned} \tag{116}$$

The next steps involve writing $\partial B \equiv \cup S_m$, separating the constant and linear parts of $u_{i,n}$ in the first term on the RHS of (116), and using Eq. (115). This sets the stage for converting I_2 into two contour integrals. Details are given in Appendix C of this section.

The final result is a HBCE version of the regularized HBIE (35). This equation is valid at any point on the boundary ∂B as long as the stress (i.e., all its 6 components) is continuous there. This includes edge, corner and regular points, that lie on or off contours.

The regularized HBCE is:

$$\begin{aligned} 0 = &- \sum_{m=1}^{M} \sum_{\alpha=13}^{27} \left[\oint_{L_m} (\bar{\sigma}_{\alpha ij} U_{ik} - \bar{u}_{\alpha i} \Sigma_{ijk}) \epsilon_{jnt} dz_t \right] [\overset{m}{T^{-1}} \overset{m}{a}]_\alpha \\ &+ \sum_{m=1}^{M} \sum_{\alpha=4}^{12} \left[\oint_{L_m} (\bar{\sigma}_{\alpha ij} U_{ik} - \bar{u}_{\alpha i} \Sigma_{ijk}) \epsilon_{jst} z_s dz_t \right] [R_{,N} \overset{m}{T^{-1}} \overset{m}{a}]_{\alpha-3} \\ &- \sum_{\substack{m=1 \\ m \notin \mathcal{S}}}^{M} \sum_{\alpha=4}^{12} \left[\oint_{L_m} (\bar{\sigma}_{\alpha ij} U_{ik} - \bar{u}_{\alpha i} \Sigma_{ijk}) \epsilon_{jnt} dz_t \right] [R(\overset{m}{T^{-1}} \overset{m}{a} - \overset{P}{T^{-1}} \overset{P}{a})]_{\alpha-3} \\ &+ \sum_{\substack{m=1 \\ m \notin \mathcal{S}}}^{M} \sum_{\alpha=1}^{3} \left[\oint_{L_m} D_{\alpha jk} dz_j \right] \left[S_{,N} (\overset{m}{T^{-1}} \overset{m}{a} - \overset{P}{T^{-1}} \overset{P}{a}) \right]_\alpha \\ &+ \sum_{\substack{m=1 \\ m \notin \mathcal{S}}}^{M} \sum_{\alpha=1}^{3} \left[\oint_{L_m} \Sigma_{\alpha jk} \epsilon_{jnt} dz_t \right] [S(\overset{m}{T^{-1}} \overset{m}{a} - \overset{P}{T^{-1}} \overset{P}{a})]_\alpha, \end{aligned} \tag{117}$$

where, as before, $\mathcal{S}$ is the set of boundary elements that contains the source point $\mathbf{x}$. The derivatives $R_{,N}$ and $S_{,N}$ in (117) are taken with respect to the source point coordinates x_n. In Eq. (117), the integrands in the first two terms are regular ($O(1)$). The third and fourth (potentially strongly singular, $O(1/r)$) as well as the fifth (potentially hypersingular, $O(1/r^2)$) need to be evaluated only on nonsingular elements.

4.1.10. *Collocation of the HBCE at an irregular surface point*

Martin *et al.* [1998] have stated the requirements for collocating a regularized HBIE at an irregular point on ∂B. This matter is discussed in Mukherjee and Mukherjee [2005]. It has been proved in Mukherjee and Mukherjee [2001] (see, also Mukherjee and Mukherjee [2005]) that the BCE interpolation functions given in Eqs. (82) and (83) satisfy, a priori, all these smoothness requirements for collocation of the HBCE (117) at an irregular surface point. Thus, there is no need to consider "relaxed smoothness requirements" in this method. It is worth repeating again that it is extremely difficult to find, in general, BEM shape functions (for 3D elasticity problems) that satisfy conditions ii(b)–iv [Mukherjee and Mukherjee (2005)] a priori. The primary reason for this is that BEM shape functions are defined only on the bounding surface of a body, while the BCM ones are defined in B (although the weights are defined only on ∂B).

4.1.11. *Displacements and stresses at internal points*

At this stage, it is a simple matter to derive equations for displacements and stresses at a point inside a body. The general equations are derived in Mukherjee *et al.* [2000a] and equations for internal points close to the bounding surface are derived in Mukherjee *et al.* [2000b]. They are given below.

Internal displacements. One has to compare the regularized BIE (75), the regularized BCE (99) and the usual BIE (19) at an internal point $p = \boldsymbol{\xi}$. The result is:

$$
\begin{aligned}
u_k(\boldsymbol{\xi}) = \frac{1}{2}\sum_{m=1}^{M}\sum_{\alpha=13}^{27}\left[\oint_{L_m}(\bar{\sigma}_{\alpha ij}(\mathbf{z})U_{ik}(\mathbf{z}) - \bar{u}_{\alpha i}(\mathbf{z})\Sigma_{ijk}(\mathbf{z}))\epsilon_{jst}z_s dz_t\right]\Big[\overset{m}{T}{}^{-1}\overset{m}{a}\Big]_{\alpha} \\
+\sum_{m=1}^{M}\sum_{\alpha=4}^{12}\left[\oint_{L_m}(\bar{\sigma}_{\alpha ij}(\mathbf{z})U_{ik}(\mathbf{z}) - \bar{u}_{\alpha i}(\mathbf{z})\Sigma_{ijk}(\mathbf{z}))\epsilon_{jst}z_s dz_t\right] \\
\times\Big[R(\boldsymbol{\xi})\,\overset{m}{T}{}^{-1}\overset{m}{a}\Big]_{\alpha-3} \\
+\sum_{m=1}^{M}\sum_{\alpha=1}^{3}\left[\oint_{L_m}D_{\alpha jk}(\mathbf{z})dz_j\right]\Big[S(\boldsymbol{\xi})\,\overset{m}{T}{}^{-1}\overset{m}{a}\Big]_{\alpha},
\end{aligned}
\tag{118}
$$

where $\mathbf{z} = \mathbf{y} - \boldsymbol{\xi}$.

Displacements at internal points close to the boundary. One should study Sec. 2.2.4 for a similar discussion related to the BEM [Mukherjee *et al.* (2000b)].

The first step is to choose the target point $\hat{\mathbf{x}}$ at or close to the centroid of a boundary element (see Fig. 3). Since all other terms in Eq. (118), except the one involving the solid angle, are evaluated as contour integrals, these terms are already regularized. There are at least two ways of regularizing the solid angle term in

Eq. (118). The first is to evaluate the solid angle Ω (see Eq. (98)) as a line integral by employing Eq. (16) in Liu [1998]. The second is to use a boundary contour version of Eq. (43) and still evaluate Ω as a surface integral. The latter approach is adopted in this work.

The boundary contour version of Eq. (43) is:

$$\begin{aligned} u_k(\boldsymbol{\xi}) = u_k(\hat{\mathbf{x}}) &+ \frac{1}{2}\sum_{m=1}^{M}\sum_{\alpha=13}^{27}\left[\oint_{L_m}(\bar{\sigma}_{\alpha ij}(\mathbf{z})U_{ik}(\mathbf{z}) - \bar{u}_{\alpha i}(\mathbf{z})\Sigma_{ijk}(\mathbf{z}))\epsilon_{jst}z_s dz_t\right]\left[\overset{m}{T^{-1}}\overset{m}{a}\right]_{\alpha} \\ &+ \sum_{m=1}^{M}\sum_{\alpha=4}^{12}\left[\oint_{L_m}(\bar{\sigma}_{\alpha ij}(\mathbf{z})U_{ik}(\mathbf{z}) - \bar{u}_{\alpha i}(\mathbf{z})\Sigma_{ijk}(\mathbf{z}))\epsilon_{jst}z_s dz_t\right]\left[R(\boldsymbol{\xi})\ \overset{m}{T^{-1}}\overset{m}{a}\right]_{\alpha-3} \\ &+ \sum_{m=1}^{M}\sum_{\alpha=1}^{3}\left[\oint_{L_m} D_{\alpha jk}(\mathbf{z})dz_j\right]\left[S(\boldsymbol{\xi})\ \overset{m}{T^{-1}}\overset{m}{a} - S(\hat{\mathbf{x}})\beta^{\hat{P}}\right]_{\alpha}, \end{aligned} \tag{119}$$

where

$$u_k(\hat{\mathbf{x}}) = \hat{\beta}_k^{\hat{P}} = \sum_{\alpha=1}^{27} S_{k\alpha}(\hat{\mathbf{x}})\beta_{\alpha}^{\hat{P}}. \tag{120}$$

Note that the point $\hat{P}$ has coordinates $\hat{\mathbf{x}}$.

It is important to note that, on a singular element (i.e., when integration is being carried out on an element that contains the point $\hat{\mathbf{x}}$), one has:

$$\overset{m}{T^{-1}}\overset{m}{a} = \overset{m}{\beta} = \beta^{\hat{P}}. \tag{121}$$

In this case, the numerator of the last integrand in Eq. (119) is $\mathcal{O}(r(\boldsymbol{\xi}, \hat{\mathbf{x}}))$ while the denominator in the solid angle term is $\mathcal{O}(r^2(\boldsymbol{\xi}, \hat{\mathbf{x}}))$ as $\mathbf{y} \to \hat{\mathbf{x}}$, so that Eq. (119) is "nearly weakly singular" as $\mathbf{y} \to \hat{\mathbf{x}}$. It is useful to remember that the integral of $D_{\alpha jk}$ in Eq. (119) contains the solid angle term which is evaluated as a surface integral.

Internal stresses. This time, one compares the regularized HBIE (35), the regularized HBCE (117) and the usual integral expression for the displacement gradient at an internal point $p = \boldsymbol{\xi}$ (Eq. (32)). The result is:

$$\begin{aligned} u_{k,n}(\boldsymbol{\xi}) = &- \sum_{m=1}^{M}\sum_{\alpha=13}^{27}\left[\oint_{L_m}(\bar{\sigma}_{\alpha ij}(\mathbf{z})U_{ik}(\mathbf{z}) - \bar{u}_{\alpha i}(\mathbf{z})\Sigma_{ijk}(\mathbf{z}))\epsilon_{jnt}dz_t\right]\left[\overset{m}{T^{-1}}\overset{m}{a}\right]_{\alpha} \\ &+ \sum_{m=1}^{M}\sum_{\alpha=4}^{12}\left[\oint_{L_m}(\bar{\sigma}_{\alpha ij}(\mathbf{z})U_{ik}(\mathbf{z}) - \bar{u}_{\alpha i}(\mathbf{z})\Sigma_{ijk}(\mathbf{z}))\epsilon_{jst}z_s dz_t\right] \\ &\times \left[R_{,n}(\boldsymbol{\xi})\ \overset{m}{T^{-1}}\overset{m}{a}\right]_{\alpha-3} \end{aligned}$$

$$
\begin{aligned}
&- \sum_{m=1}^{M} \sum_{\alpha=4}^{12} \left[\oint_{L_m} (\bar{\sigma}_{\alpha ij}(\mathbf{z}) U_{ik}(\mathbf{z}) - \bar{u}_{\alpha i}(\mathbf{z}) \Sigma_{ijk}(\mathbf{z})) \epsilon_{jnt} dz_t \right] \left[R(\boldsymbol{\xi}) \overset{m}{T}{}^{-1} \overset{m}{a} \right]_{\alpha-3} \\
&+ \sum_{m=1}^{M} \sum_{\alpha=1}^{3} \left[\oint_{L_m} D_{\alpha jk}(\mathbf{z}) dz_j \right] \left[S_{,n}(\boldsymbol{\xi}) \overset{m}{T}{}^{-1} \overset{m}{a} \right]_{\alpha} \\
&+ \sum_{m=1}^{M} \sum_{\alpha=1}^{3} \left[\oint_{L_m} \Sigma_{\alpha jk}(\mathbf{z}) \epsilon_{jnt} dz_t \right] \left[S(\boldsymbol{\xi}) \overset{m}{T}{}^{-1} \overset{m}{a} \right]_{\alpha}. \qquad (122)
\end{aligned}
$$

Hooke's law is now used to obtain the internal stresses from the internal displacement gradients.

Curvatures at an internal point are given in Eqs. (108)–(110).

Stresses at internal points close to the bounding surface. As before for the case of displacement evaluation at an internal point close to the boundary of a body, one has two choices with respect to the strategy for the evaluation of the solid angle. Again, for the sake of uniformity, a boundary contour version of Eq. (45) is used here, together with the evaluation of the solid angle as a surface integral.

A boundary contour version of Eq. (45) is obtained in a manner that is quite analogous to the approach discussed in Sec. 4.1.9 [Mukherjee and Mukherjee (1998)]. The first step is to use the product rule to transform Eq. (45) to the form:

$$
\begin{aligned}
u_{k,n}(\boldsymbol{\xi}) = u_{k,n}(\hat{\mathbf{x}}) &- \int_{\partial B} [U_{ik}(\boldsymbol{\xi}, \mathbf{y}) [\sigma_{ij}(\mathbf{y}) - \sigma_{ij}(\hat{\mathbf{x}})] \\
&- \Sigma_{ijk}(\boldsymbol{\xi}, \mathbf{y}) [u_i(\mathbf{y}) - u_i^{(L)}]]_{,n} n_j(\mathbf{y}) dS(\mathbf{y}) \\
&+ \int_{\partial B} [U_{ik}(\boldsymbol{\xi}, \mathbf{y}) \sigma_{ij,n}(\mathbf{y}) - \Sigma_{ijk}(\boldsymbol{\xi}, \mathbf{y}) [u_{i,n}(\mathbf{y}) - u_{i,n}(\hat{\mathbf{x}})]] \\
&\times n_j(\mathbf{y}) dS(\mathbf{y}), \qquad (123)
\end{aligned}
$$

where (see Fig. 3):

$$
u_i^{(L)} = u_i(\hat{\mathbf{x}}) + u_{i,\ell}(\hat{\mathbf{x}}) \hat{z}_\ell, \qquad (124)
$$

with

$$
\hat{z}_\ell = y_\ell - \hat{x}_\ell. \qquad (125)
$$

The BCM version of Eq. (45) is:

$$
\begin{aligned}
u_{k,n}(\boldsymbol{\xi}) &= u_{k,n}(\hat{\mathbf{x}}) \\
&- \sum_{m=1}^{M} \sum_{\alpha=13}^{27} \left[\oint_{L_m} (\bar{\sigma}_{\alpha ij}(\hat{\mathbf{z}}) U_{ik}(\mathbf{z}) - \bar{u}_{\alpha i}(\hat{\mathbf{z}}) \Sigma_{ijk}(\mathbf{z})) \epsilon_{jnt} dz_t \right] \left[\overset{m}{T}{}^{-1} \overset{m}{a} \right]_{\alpha}
\end{aligned}
$$

$$+\sum_{m=1}^{M}\sum_{\alpha=4}^{12}\left[\oint_{L_m}(\bar{\sigma}_{\alpha ij}(\mathbf{z})U_{ik}(\mathbf{z})-\bar{u}_{\alpha i}(\mathbf{z})\Sigma_{ijk}(\mathbf{z}))\epsilon_{jst}z_s dz_t\right]$$

$$\times\left[R_{,n}(\boldsymbol{\xi})\overset{m}{T^{-1}}\overset{m}{a}\right]_{\alpha-3}$$

$$-\sum_{\substack{m=1\\ m\notin\mathcal{S}}}^{M}\sum_{\alpha=4}^{12}\left[\oint_{L_m}(\bar{\sigma}_{\alpha ij}(\hat{\mathbf{z}})U_{ik}(\mathbf{z})-\bar{u}_{\alpha i}(\hat{\mathbf{z}})\Sigma_{ijk}(\mathbf{z}))\epsilon_{jnt}dz_t\right]$$

$$\times\left[R(\hat{\mathbf{x}})\left(\overset{m}{T^{-1}}\overset{m}{a}-\beta^{\hat{P}}\right)\right]_{\alpha-3}$$

$$+\sum_{m=1}^{M}\sum_{\alpha=1}^{3}\left[\oint_{L_m}D_{\alpha jk}(\mathbf{z})dz_j\right]\left[S_{,n}(\boldsymbol{\xi})\overset{m}{T^{-1}}\overset{m}{a}-S_{,n}(\hat{\mathbf{x}})\beta^{\hat{P}}\right]_{\alpha}$$

$$+\sum_{\substack{m=1\\ m\notin\mathcal{S}}}^{M}\sum_{\alpha=1}^{3}\left[\oint_{L_m}\Sigma_{\alpha jk}(\mathbf{z})\epsilon_{jnt}dz_t\right]\left[S(\hat{\mathbf{x}})\left(\overset{m}{T^{-1}}\overset{m}{a}-\beta^{\hat{P}}\right)\right]_{\alpha}. \tag{126}$$

It should be noted that the first, third and fifth terms, with summations and integrals, on the RHS of Eq. (126), arise from the first integral in Eq. (123); while the second and fourth arise from the second integral in Eq. (123). Again, as in the case of Eq. (119), the fifth term (i.e., the fourth with summations and integral) on the RHS of Eq. (126) is "nearly weakly singular" ($\mathcal{O}(1/r(\boldsymbol{\xi},\hat{\mathbf{x}}))$ as $\mathbf{y}\to\hat{\mathbf{x}}$).

4.1.12. *Numerical results*

Numerical results from the BCM and the HBCM, for selected 3D examples, are available [Nagarajan *et al.* (1996); Mukherjee *et al.* (1997); Mukherjee and Mukherjee (1998)]. Typical results, for a thick hollow sphere under internal pressure, are given below. For results in the first three paragraphs in this subsection, the inner and outer radii of the sphere are 1 and 2 units, respectively, the shear modulus $\mu = 1$, the Poisson's ratio $\nu = 0.3$, and the internal pressure is 1. For results in the last paragraph, the inner and outer radii of the sphere are 1 and 4 units, respectively, Young's modulus $E = 1$, Poisson's ratio $\nu = 0.25$, and the internal pressure is 1. A generic surface mesh on a one-eighth sphere is shown in Fig. 14. Two levels of discretization — medium and fine, are used in this work. The boundary elements on each surface of the one-eighth sphere are nearly uniform. Mesh statistics are given in Table 5.

Surface displacements from the BCM and the HBCM. First, note that (117) has two free indices, k and n, so that it represents nine equations. These equations arise from $u_{k,n}$. Different strategies are possible for collocating (117) at a boundary point. The first is to use all nine equations. The second is to use six corresponding to $\epsilon_{kn} = (1/2)(u_{k,n} + u_{n,k})$. The six-equation strategy amounts to

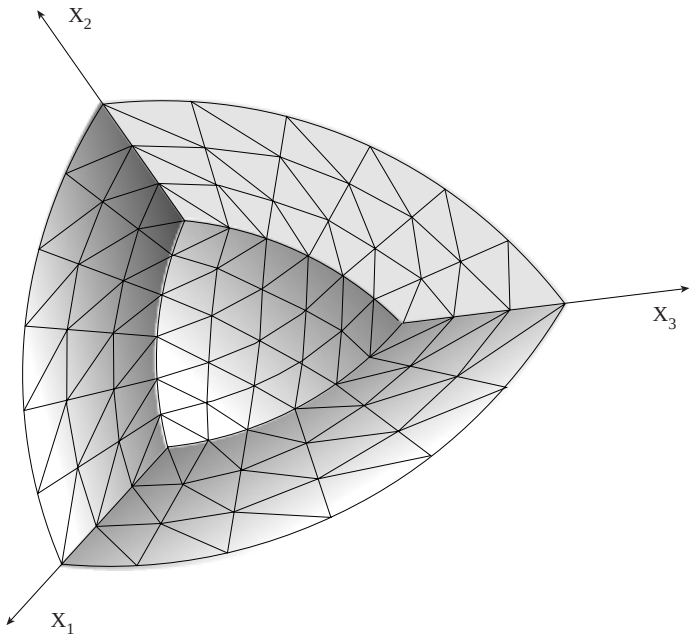

Fig. 14. A typical mesh on the surface of a one-eighth sphere (from Mukherjee *et al.* [1999]).

Table 5. Mesh statistics on a one-eighth sphere (from Mukherjee *et al.* [1999]).

Mesh	Number of Elements		
	On each flat plane	On each curved surface	Total
Coarse	12	9	54
Medium	36	36	180
Fine	64	64	320

replacing U_{kn}, the RHS of (117), by $(1/2)(U_{kn} + U_{nk})$. (Note that the RHS of (117) is here called U_{kn}.) Both the nine-equation and six-equation strategies lead to overdetermined systems, but are convenient for collocating at irregular boundary points since the source point normal is not involved in these cases. A third, the three-equation strategy, suitable for collocation at regular points, corresponds to the traction components τ_n. In this case, the RHS (U_{kn}) of (117) is replaced by $[\lambda U_{mm}\delta_{kn}+\mu(U_{kn}+U_{nk})]n_k(P)$. The three-equation strategy involving the traction components is not convenient for collocating the HBCE at a point on an edge or a corner of a body where the normal to the body surface has a jump discontinuity. In view of the assumed continuity of the stress tensor at such a point, this situation leads to a jump in traction at that point, unless the stress tensor is zero there. One would, therefore, need to use multiple source points, each belonging to a smooth

surface meeting at that irregular point, and collocate separately at these points. Since the primary purpose here is to demonstrate collocation of (35) at irregular boundary points, only the nine-equation and six-equation strategies are used below.

It should be mentioned here that, for the HBCM in 2D elasticity, the displacement gradient strategy has been successfully employed in Phan *et al.* [1998] and the traction strategy above has been implemented by Zhou *et al.* [1999].

The overdetermined system of linear algebraic equations, resulting from the nine-equation and the six-equation strategies mentioned above, have been solved by using a subroutine based on QR decomposition of the system matrix. This subroutine has been obtained from the IMSL software package.

It is seen from Fig. 14 that many of the collocation points lie on edges and six of them lie on corners of the surface of the one-eighth sphere. These results, displayed in Fig. 15, show a comparison of the BCM (from Eq. (99)) and HBCM (from Eq. (117)) results with the exact solution of the problem [Timoshenko and Goodier (1970)]. The first and last points along the axis lie on corners, the rest lie along an edge. The agreement between the exact, BCM and nine-equation HBCM solution is seen to be very good.

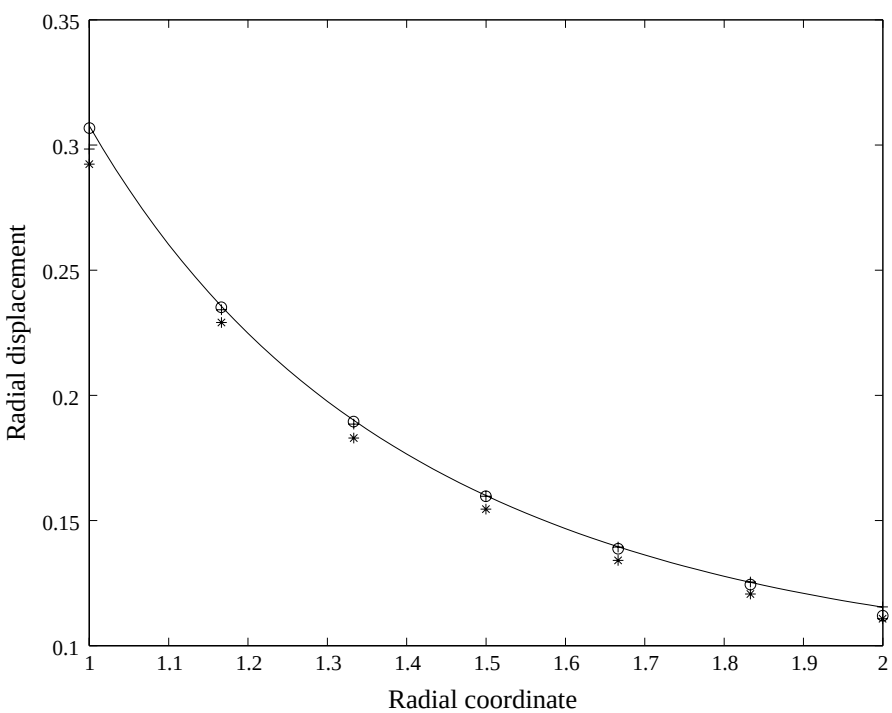

Fig. 15. Hollow sphere under internal pressure. Radial displacement as a function of radius along the x_1 axis. Numerical solutions are obtained from the medium mesh. Exact solution: —, BCM solution: ∘ ∘ ∘∘, six-equation HBCM solution: ∗∗∗∗, nine-equation HBCM solution: ++++ (from Mukherjee and Mukherjee [2001]).

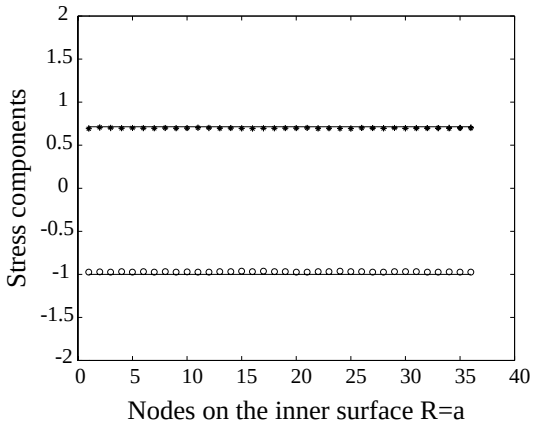

(a)

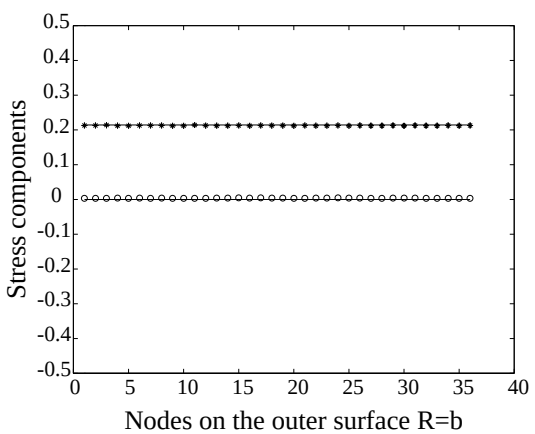

(b)

Fig. 16. Hollow sphere under internal pressure. Stresses (a) on the inner surface $R = a$ and (b) on the outer surface $R = b$. Exact solution —. Numerical solution from the medium mesh: $\sigma_{\theta\theta} = \sigma_{\phi\phi}$ ****, σ_{RR} ○○○○ (from Mukherjee *et al.* [1999]).

Surface stresses. Stresses on the inner ($R = a$) and on the outer ($R = b$) surface of the sphere, obtained from Eq. (107) and Hooke's law, are shown in Fig. 16. The nodes are chosen at the centroids of the boundary elements. The agreement between the numerical and analytical solutions is again very good.

Internal stresses relatively far from the bounding surface. Internal stresses along the line $x_1 = x_2 = x_3$, obtained from Eq. (122) and Hooke's law, appear in Fig. 17. Very good agreement is observed between the numerical and analytical solutions.

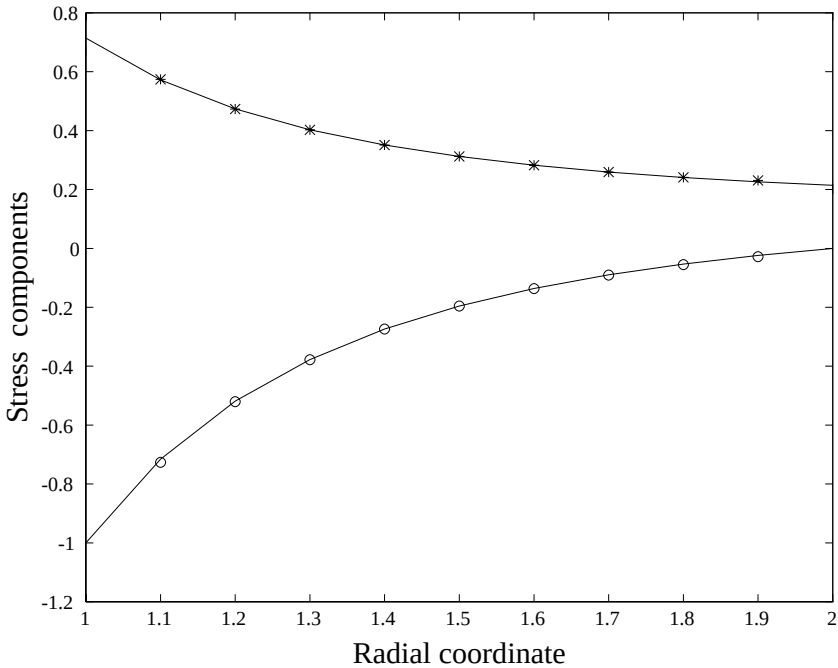

Fig. 17. Hollow sphere under internal pressure. Stresses as functions of radius along the line $x_1 = x_2 = x_3$. Exact solutions —. Numerical solutions from the fine mesh: $\sigma_{\theta\theta} = \sigma_{\phi\phi}$ ****, σ_{RR} oooo (from Mukherjee *et al.* [2000a]).

Internal stresses very close to the bounding surface. Numerical results for stress components, from the standard (Eq. (122)) and the new (Eq. (126)) BCM, are shown in Figs. 18(a) and 18(b), respectively. The results from the standard BCM exhibit large errors whereas results from the new BCM faithfully track the exact solutions in both cases. Finally, Fig. 19 gives the global picture for stresses throughout the sphere. The new BCM performs well, even at points that are very close to the surface of the hollow sphere.

It is interesting to point out that the poor performance of the standard BCM, at points close to the bounding surface (see Fig. 18), arise from erroneous numerical evaluation of "nearly hypersingular" integrals. This behavior, sometimes called the "boundary layer effect", is well known in the BEM community. Appropriate analytical treatment of the standard BEM or BCM equations is necessary before numerical computations are carried out.

4.1.13. *Appendices*

Appendix A: An explicit form of Eq. (113). Recalling Eq. (82), one has:

$$u_i(\mathbf{y}) = \sum_{\alpha=1}^{27} \hat{\beta}_\alpha^m \bar{u}_{\alpha i}(z_1, z_2, z_3),$$

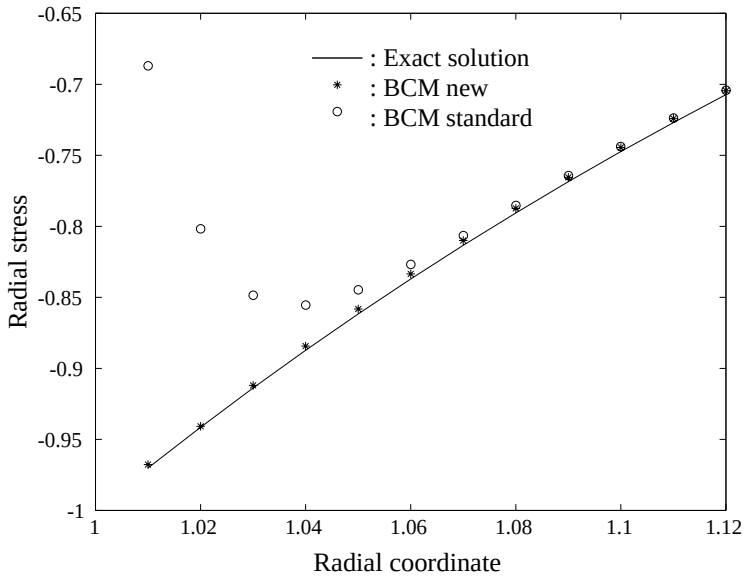

(a)

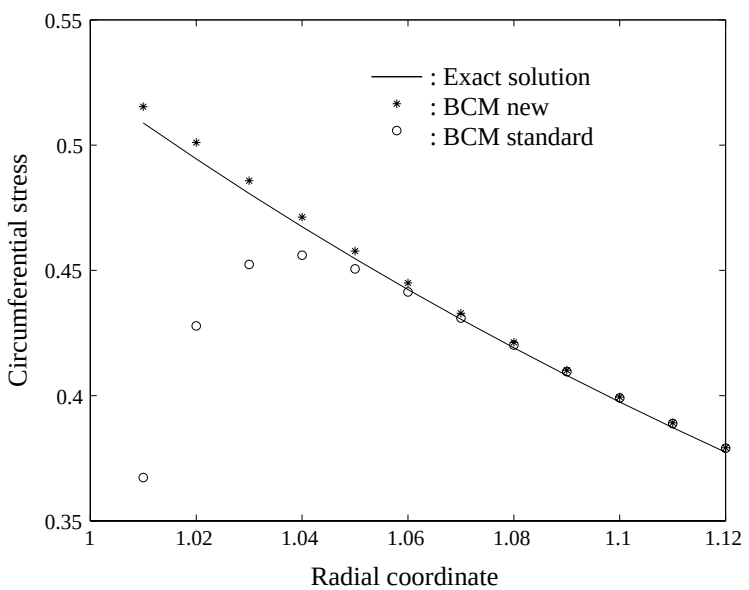

(b)

Fig. 18. Hollow sphere under internal pressure. Radial and circumferential stresses (σ_{rr} and $\sigma_{\theta\theta}$) as functions of radial distance from the center of the sphere. The new and standard BCM solutions from the fine mesh, together with exact solutions, for points very close to the inner surface of the sphere (from Mukherjee *et al.* [2000b]).

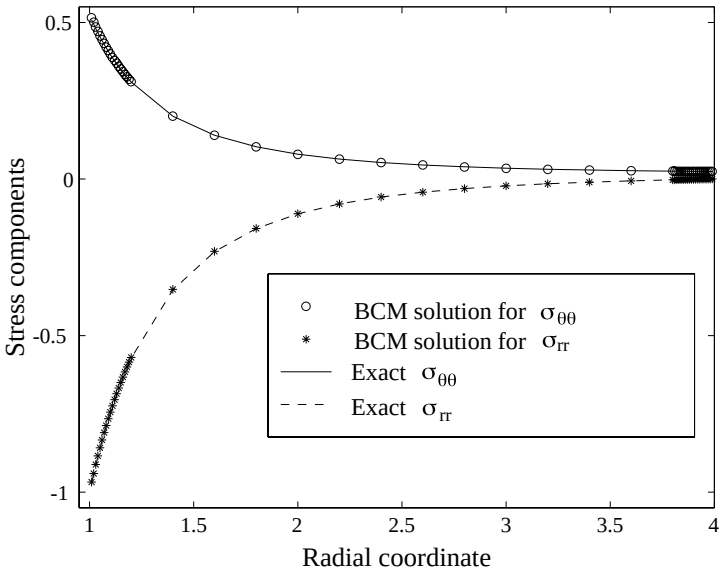

Fig. 19. Hollow sphere under internal pressure. Radial and circumferential stresses as functions of the radial distance from the center of the sphere. Results from the new BCM (fine mesh) together with the exact solution (from Mukherjee *et al.* [2000b]).

$$u_i(\mathbf{x}) = \sum_{\alpha=1}^{3} \hat{\beta}_\alpha^P \bar{u}_{\alpha i}(z_1, z_2, z_3),$$

$$u_{i,\ell}(\mathbf{x})[y_\ell - x_\ell] = \sum_{\alpha=4}^{12} \hat{\beta}_\alpha^P \bar{u}_{\alpha i}(z_1, z_2, z_3),$$

(the last equation above can be proved from Eq. (107)), the integral in Eq. (113) can be written as:

$$I_1 = \oint_{L_m} U_{ik}(\mathbf{x}, \mathbf{y}) \left[\sum_{\alpha=4}^{12} (\hat{\beta}_\alpha^m - \hat{\beta}_\alpha^P) \bar{\sigma}_{\alpha ij} + \sum_{\alpha=13}^{27} \hat{\beta}_\alpha^m \bar{\sigma}_{\alpha ij} \right] \epsilon_{jnt} dz_t$$

$$- \oint_{L_m} \Sigma_{ijk}(\mathbf{x}, \mathbf{y}) \left[\sum_{\alpha=1}^{12} (\hat{\beta}_\alpha^m - \hat{\beta}_\alpha^P) \bar{u}_{\alpha i} + \sum_{\alpha=13}^{27} \hat{\beta}_\alpha^m \bar{u}_{\alpha i} \right] \epsilon_{jnt} dz_t,$$

where the fact that $\bar{\sigma}_{\alpha ij} = 0$ for $\alpha = 1, 2, 3$ has been used.

Appendix B: Proof of Eq. (115). The displacement $u_i(\mathbf{y})$ is given by the first equation in Appendix A above. Also:

$$u_{i,n}(\mathbf{y}) = \sum_{\alpha=4}^{27} \hat{\beta}_\alpha^m \bar{u}_{\alpha i,n}(z_1, z_2, z_3), \tag{127}$$

since $\bar{u}_{\alpha i}$, $\alpha = 1, 2, 3$, are constants.

Now,

$$u_{i,n}(\mathbf{y})_{\text{constant}} \equiv \sum_{\alpha=4}^{12} \hat{\beta}_\alpha^m \bar{u}_{\alpha i,n} = \Big[S_{,N} \overset{m}{\beta} \Big]_i,$$

where the last equality is obtained from Eq. (114).

Let

$$u_{i,n}(\mathbf{y})_{\text{linear}} \equiv \sum_{\alpha=13}^{27} \hat{\beta}_\alpha^m \bar{u}_{\alpha i,n}(z_1, z_2, z_3) = \sum_{\alpha=13}^{27} \overset{m}{\beta}_\alpha \, \bar{u}_{\alpha i,n}(z_1, z_2, z_3).$$

Now, with $n = 1$,

$$\begin{aligned} \sum_{\alpha=13}^{27} \overset{m}{\beta}_\alpha \, \bar{\mathbf{u}}_{\alpha,1} &= 2\Big(\overset{m}{\beta}_{13} + \overset{m}{\beta}_{20} \Big)\overline{\mathbf{u}}_4 + 2 \overset{m}{\beta}_{15} \, \overline{\mathbf{u}}_5 + 2 \overset{m}{\beta}_{18} \, \overline{\mathbf{u}}_6 \\ &\quad +, \cdots, +\Big(k_2 \overset{m}{\beta}_{19} + k_1 \overset{m}{\beta}_{20} \Big)\overline{\mathbf{u}}_{12} \\ &= \sum_{\alpha=4}^{12} \Big[R_{,1} \overset{m}{\beta} \Big]_{\alpha-3} \bar{\mathbf{u}}_\alpha(z_1, z_2, z_3). \end{aligned}$$

Similar expressions can be obtained for $n = 2, 3$.

In the above, a vector displacement shape function is defined as:

$$\overline{\mathbf{u}}_\alpha = [\bar{u}_{\alpha 1}, \bar{u}_{\alpha 2}, \bar{u}_{\alpha 3}]^T,$$

(where T denotes the transpose of the vector), and the constants k_1 and k_2 are defined in Table 3.

Appendix C: Conversion of Eq. (116).

$$\begin{aligned} \overset{m}{I}_2 = &- \sum_{\alpha=4}^{12} \left[\int_{S_m} [U_{ik}(\mathbf{x}, \mathbf{y}) \bar{\sigma}_{\alpha ij} - \Sigma_{ijk}(\mathbf{x}, \mathbf{y}) \bar{u}_{\alpha i}] n_j dS \right] \Big[R_{,N} \overset{m}{\beta} \Big]_{\alpha-3} \\ &+ \sum_{\alpha=1}^{3} \left[\int_{S_m} \Sigma_{\alpha jk}(\mathbf{x}, \mathbf{y}) n_j dS \right] \Big[S_{,N} \overset{m}{\beta} \Big]_\alpha - \sum_{\alpha=1}^{3} u_{\alpha,n}(\mathbf{x}) \int_{S_m} \Sigma_{\alpha jk}(\mathbf{x}, \mathbf{y}) n_j dS. \end{aligned}$$

Applying Kaplan [1984]'s formula [Nagarajan *et al.* (1996); Mukherjee *et al.* (1997)], to the first term (its integrand is $O(1/r)$), one gets the contour integral:

$$\overset{m}{I}_{2_1} = - \sum_{\alpha=4}^{12} \left[\oint_{L_m} (\bar{\sigma}_{\alpha ij} U_{ik} - \bar{u}_{\alpha i} \Sigma_{ijk}) \epsilon_{jst} z_s dz_t \right] \Big[R_{,N} \overset{m}{\beta} \Big]_{\alpha-3}.$$

The remaining terms cancel on a singular element (see Eq. (114)), while, on a nonsingular element, one gets (see Eq. (100)):

$$\overset{m}{I}_{2_2} = - \sum_{\alpha=1}^{3} \left[\oint_{L_m} D_{\alpha jk} dz_j \right] \Big[S_{,N} \Big(\overset{m}{\beta} - \overset{P}{\beta} \Big) \Big]_\alpha.$$

4.2. *Boundary node method*

The Extended Boundary Node Method [EBNM Telukunta and Mukherjee (2005)], for 3D potential theory, is described below.

4.2.1. *Boundary and domain based meshfree methods*

Boundary based methods. Mukherjee, together with his research collaborators, has proposed a new computational approach called the BNM [Mukherjee and Mukherjee (1997a); Kothnur *et al.* (1999); Chati *et al.* (1999); Chati and Mukherjee (2000), Chati *et al.* (2001a, 2001b); Gowrishankar and Mukherjee (2002); Mukherjee and Mukherjee (2005)]. Other examples of boundary-based meshfree methods are the local BIE (LBIE) approach [Zhu *et al.* (1998); Sladek *et al.* (2000)], the boundary only radial basis function method (BRBFM) [Chen and Tanaka (2002)], the boundary cloud method (BCLM) [Li and Aluru (2002, 2003)], the boundary point interpolation method (BPIM) [Liu (2002)] and the hybrid boundary node method (HBNM) [Zhang *et al.* (2002)]. The LBIE, however, is not strictly a boundary method since it requires evaluation of integrals over certain surfaces (called L_s in Zhu *et al.* [1998]) that can be regarded as "closure surfaces" of boundary elements. Li and Aluru [2002, 2003] have proposed a boundary only method called the BCLM. This method is very similar to the BNM in that scattered boundary points are used for constructing approximating functions and these approximants are used with the appropriate BIEs for the problem. However, a key attractive feature of these papers is that, unlike the BNM where boundary curvilinear co-ordinates must be employed, the usual Cartesian co-ordinates can be used in the BCLM.

Domain based methods. The oldest of the meshfree methods is smooth particle hydrodynamics (SPH) [Lucy (1977); Monaghan (1982, 1988, 1992)]. Great progress has been made during the last twenty years in solid mechanics applications of domain-based mesh-free methods. Prominent among these include the element-free galerkin (EFG) method [Belytschko *et al.* (1994, 1996); Bobaru and Mukherjee (2001, 2002); Mukherjee and Mukherjee (1997b)], the reproducing Kernel particle method (RKPM) [Liu *et al.* (1996a, 1996b)], $h-p$ clouds [Oden *et al.* (1998)], the meshless local Petrov–Galerkin (MLPG) approach [Atluri and Shen (2002); Gilhooley *et al.* (2008); Batra and Spinello (2009); Batra and Porfiri (2008)], the natural element method (NEM) [Sukumar *et al.* (2001)], the generalized finite element method (GFEM) [Strouboulis *et al.* (2000)], the extended finite element method (X-FEM) [Sukumar *et al.* (2000)], the method of finite spheres (MFS) [De and Bathe (2001a, 2001b)] and the finite cloud method (FCM) [Aluru and Li (2001)].

4.2.2. *Boundary node method*

The BNM is a combination of the moving least squares (MLS) approximation scheme [Lancaster and Salkauskas (1981)] and the standard BIE method. The method divorces the traditional coupling between spatial discretization (meshing)

and interpolation (as commonly practiced in the FEM or in the BEM). Instead, a "diffuse" approximation, based on MLS approximants, is used to represent the unknown functions; and boundary cells, with a very flexible structure (e.g., any cell can be arbitrarily subdivided without affecting its neighbors), are used for integration. Thus, the BNM retains the *meshless attribute of the EFG method [Belytschko et al. (1994)] and the dimensionality advantage of the BEM*. As a consequence, the BNM only requires the specification of *points on the* $2D$ *bounding surface* of a 3D body (including crack faces in fracture mechanics problems), together with unstructured surface cells, thereby practically eliminating the meshing problem. In contrast, the FEM needs volume meshing, the BEM needs surface meshing, and the EFG needs points throughout the domain of a body.

It is important to mention here that integration over boundary cells is still required in the standard BNM. (Totally mesh-free versions, however, have been proposed [Gowrishankar and Mukherjee (2002); Zhang *et al.* (2002)]). Therefore, the BNM is a "pseudo" meshfree method rather than a "pure" one.

As mentioned above, use of Cartesian, rather than curvilinear co-ordinates, is certainly preferable in the BNM, especially for 3D problems. This has been done (for 2D problems) by Li and Aluru [2002, 2003] in an elegant fashion. The approaches presented in these two papers, however, have certain disadvantages. The Hermite type approximation approach [Li and Aluru (2002)] requires fairly intensive computations. The variable basis approach [Li and Aluru (2003)] (as well as the standard BNM [Mukherjee and Mukherjee (1997a)]), on the other hand, does not properly model possible discontinuities in the normal derivative of the potential function across edges and corners. Telukunta and Mukherjee [2004] have tried to combine the advantages of the variable basis approach [Li and Aluru (2003)], together with allowing possible discontinuities in the normal derivative of the potential function, across edges and corners, in an approach called the EBNM.

The next section describes reduced basis functions, proposed in the EBNM, for 3D problems in potential theory. This is followed by a discussion of coupling of these approximants with the standard BIE in order to obtain the EBNM. Numerical results for some Dirichlet problems and one mixed problem, in 3D potential theory, complete this discussion. Particular attention is paid to the question of modeling of discontinuities in the normal derivative of the potential function across edges and corners.

4.2.3. *The boundary node method with Cartesian coordinates*

It is assumed that the bounding surface ∂B of a solid body B is the union of piecewise smooth segments called panels. The BNM employs a diffuse approximation in which the value of a variable at a boundary point is defined in terms of its values at neighboring boundary points within its domain of dependence (DOD). Correspondingly, a boundary node affects points within its range of influence (ROI). These regions are shown in Fig. 20(a).

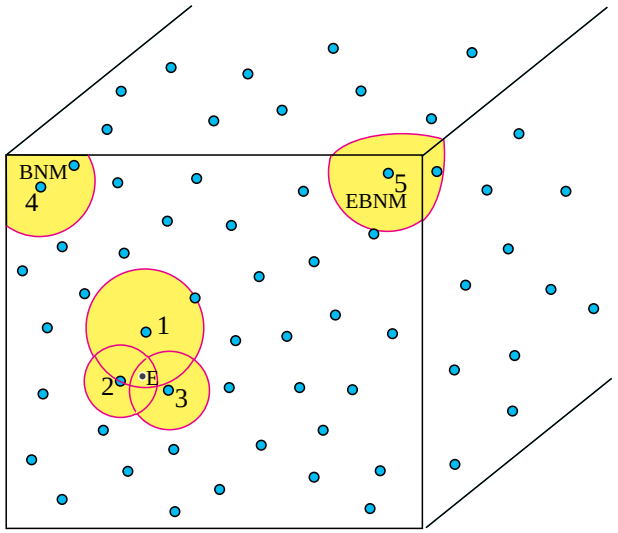

(a)

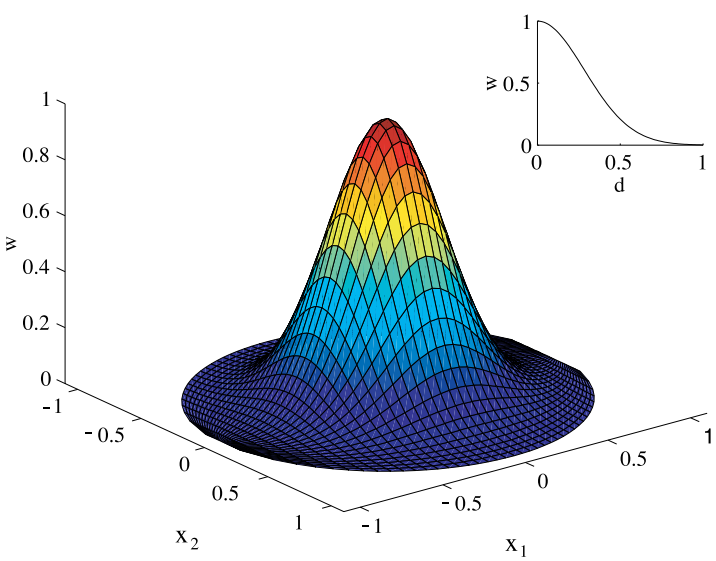

(b)

Fig. 20. (Color online) DOD and ROI. (a) The nodes 1, 2 and 3 lie within the DOD of the evaluation point E. The ROIs of nodes 1, 2, 3, 4 and 5 are shown as gray regions. In the standard BNM, the ROI of a node near an edge, e.g., node 4, is truncated at the edges of a panel. In the EBNM, the ROI can reach over to neighboring panels and contain edges and/or corners — see, e.g., node 5 (b) Gaussian weight function defined on the ROI of a node (from Telukunta and Mukherjee [2005]).

One of the drawbacks of using curvilinear boundary co-ordinates in the BNM, especially for 3D problems, is the need to truncate the ROI of a node at an edge or corner (see Fig. 20(a)). Another is the need to compute geodesics on general surfaces (for 3D problems). The more straightforward approach, namely the use of Cartesian co-ordinates, suffers from the disadvantage that the matrix $\mathbf{A} = \mathbf{P}^T\mathbf{W}\mathbf{P}$ (defined later) becomes singular if all the nodes in the DOD of an evaluation point lie on a straight line for 2D or on a plane for 3D problems [Nayroles *et al.* (1992); Li and Aluru (2002, 2003); Telukunta and Mukherjee (2004)]. Li and Aluru [2002, 2003] have suggested ways to use Cartesian co-ordinates in a modified version of the BNM which is called the BCLM in the present paper. Nice results for 2D problems in potential theory are given in these papers. An improvement on the original BNM and the BCM is achieved in the EBNM. A detailed formulation of the EBNM, for problems in 2D potential theory, is presented in Telukunta and Mukherjee [2004]. This idea is discussed below for 3D problems in potential theory with linear approximants [Telukunta and Mukherjee (2005)]. Extension to 3D elasticity is relatively straightforward.

MLS approximants. Let B be a 3D body with a piecewise smooth bounding surface ∂B. One writes:

$$u(\mathbf{x}) = \mathbf{p}^T(\mathbf{x})\mathbf{a}, \quad \tau(\mathbf{x}) = \mathbf{q}^T(\mathbf{x})\mathbf{b}, \tag{128}$$

where $u(\mathbf{x})$ is the sought after harmonic function, and its normal derivative is $\tau = \frac{\partial u}{\partial n}$. Collocation is only allowed at a point on ∂B where the boundary is locally smooth — it is not allowed on an edge or at a corner. Appropriate selection of the approximation functions $\mathbf{p}(\mathbf{x})$ and $\mathbf{q}(\mathbf{x})$ (each a vector of length m) is of crucial importance. The choice of $\mathbf{q}(\mathbf{x})$, in fact, is the key contribution of the present work, and is discussed in detail later in this section.

The coefficients a_i and b_i are obtained by minimizing the weighted discrete L_2 norms:

$$R_u = \sum_{I=1}^{n} w_I(d)[\mathbf{p}^T(\mathbf{x}^I)\mathbf{a} - \hat{u}_I]^2, \quad R_\tau = \sum_{I=1}^{n} w_I(d)[\mathbf{q}^T(\mathbf{x}^I)\mathbf{b} - \hat{\tau}_I]^2, \tag{129}$$

where the summation is carried out over the n boundary nodes for which the weight function (discussed in the next subsection) $w_I(d) \neq 0$. These n nodes are said to be within the DOD of a point $\mathbf{x}$ (evaluation point E in Fig. 20(a)). Also, $\hat{u}_I$ and $\hat{\tau}_I$ are approximations to the nodal values u_I and τ_I. These equations can be written in compact form as:

$$R_u = [\mathbf{P}(\mathbf{x}^I)\mathbf{a} - \hat{\mathbf{u}}]^T\mathbf{W}(\mathbf{x}, \mathbf{x}^I)[\mathbf{P}(\mathbf{x}^I)\mathbf{a} - \hat{\mathbf{u}}], \tag{130}$$

$$R_\tau = [\mathbf{Q}(\mathbf{x}^I)\mathbf{b} - \hat{\boldsymbol{\tau}}]^T\mathbf{W}(\mathbf{x}, \mathbf{x}^I)[\mathbf{Q}(\mathbf{x}^I)\mathbf{b} - \hat{\boldsymbol{\tau}}], \tag{131}$$

where $\hat{\mathbf{u}}^T = (\hat{u}_1, \hat{u}_2, \ldots, \hat{u}_n)$, $\hat{\boldsymbol{\tau}}^T = (\hat{\tau}_1, \hat{\tau}_2, \ldots, \hat{\tau}_n)$, $\mathbf{P}(\mathbf{x}^I)$ is an $n \times m$ matrix whose kth row is:

$$[p_1(\mathbf{x}^k), p_2(\mathbf{x}^k), \ldots, p_m(\mathbf{x}^k)].$$

Similarly for $\mathbf{Q}(\mathbf{x}^I)$; and $\mathbf{W}(\mathbf{x}, \mathbf{x}^I)$ is an $n \times n$ diagonal matrix with $w_{kk} = w_k(d)$ (no sum over k).

The stationarity of R_u and R_τ with respect to $\mathbf{a}$ and $\mathbf{b}$, respectively, leads to the equations:

$$\mathbf{a}(\mathbf{x}) = \mathbf{A}^{-1}(\mathbf{x})\mathbf{B}(\mathbf{x})\hat{\mathbf{u}}, \quad \mathbf{b}(\mathbf{x}) = \mathbf{C}^{-1}(\mathbf{x})\mathbf{D}(\mathbf{x})\hat{\boldsymbol{\tau}}, \tag{132}$$

where

$$\begin{aligned} \mathbf{A}(\mathbf{x}) &= \mathbf{P}^T(\mathbf{x}^I)\mathbf{W}(\mathbf{x}, \mathbf{x}^I)\mathbf{P}(\mathbf{x}^I), \quad \mathbf{B}(\mathbf{x}) = \mathbf{P}^T(\mathbf{x}^I)\mathbf{W}(\mathbf{x}, \mathbf{x}^I), \\ \mathbf{C}(\mathbf{x}) &= \mathbf{Q}^T(\mathbf{x}^I)\mathbf{W}(\mathbf{x}, \mathbf{x}^I)\mathbf{Q}(\mathbf{x}^I), \quad \mathbf{D}(\mathbf{x}) = \mathbf{Q}^T(\mathbf{x}^I)\mathbf{W}(\mathbf{x}, \mathbf{x}^I). \end{aligned} \tag{133}$$

It is noted that the coefficients a_i and b_i are functions of $\mathbf{x}$. Substituting Eq. (132) into Eq. (128), leads to:

$$u(\mathbf{x}) = \sum_{I=1}^{n} M_I(\mathbf{x})\hat{u}_I, \quad \tau(\mathbf{x}) = \sum_{I=1}^{n} N_I(\mathbf{x})\hat{\tau}_I, \tag{134}$$

where

$$\mathbf{M}(\mathbf{x}) = \mathbf{p}^T(\mathbf{x})(\mathbf{A}^{-1}\mathbf{B})(\mathbf{x}), \quad \mathbf{N}(\mathbf{x}) = \mathbf{q}^T(\mathbf{x})(\mathbf{C}^{-1}\mathbf{D})(\mathbf{x}). \tag{135}$$

The matrices $\mathbf{A}$ and $\mathbf{C}$ must be nonsingular for this method to work. This issue is discussed in Li and Aluru [2003], Telukunta and Mukherjee [2004] and also later in the present paper. Equations (134) relate the approximations $\hat{\mathbf{u}}$ and $\hat{\boldsymbol{\tau}}$ to their real values. Matrix versions of (134) can be written as:

$$[\mathbf{H}]\{\hat{\mathbf{u}}\} = \{\mathbf{u}\}, \quad [\mathbf{J}]\{\hat{\boldsymbol{\tau}}\} = \{\boldsymbol{\tau}\}. \tag{136}$$

Equations (136) relate the nodal approximations of u and τ to their nodal values.

Weight functions. A MLS approach is adopted in the BNM and in the EBNM. Now, one has variable weight functions within each cloud, i.e., $w_I(\mathbf{x}, \mathbf{x}^I)$. The basic idea behind the choice of a weight function is that its value should decrease with distance from a node and that it should have compact support so that the ROI of the node (see Fig. 20(b)) is of finite extent. A simple choice is the Gaussian weight function (used in this work):

$$w_I(d) = \begin{cases} e^{-(d/d_I)^2} & \text{for } d \le d_I \\ 0 & \text{for } d > d_I, \end{cases} \tag{137}$$

where $d = g(\mathbf{x}, \mathbf{x}^I)$ is the minimum distance measured on the surface ∂B (i.e., the *geodesic*) between $\mathbf{x}$ and the collocation node I with co-ordinates $\mathbf{x}^I$; and the quantities d_I determine the extent of the ROI (the compact support) of node I. Other choices of weight functions are discussed in the literature [Chati and Mukherjee (2000); Mukherjee and Mukherjee (2005)], including an exponential weight function that is continuous (equals zero) at $d = d_I$. See Most and Bucher [2005] for a proposal of a weight function such that the MLS interpolants approximately satisfy the delta function property. The weight function in (137), which, of course, is

discontinuous at $d = d_I$, is simpler to evaluate and works well for the numerical examples discussed later in this paper.

In the previous research performed on the 3D BNM, the ROI of a node has been truncated at the edge of a panel (Fig. 20(a)) so that geodesics need only be computed on piecewise smooth surfaces. The ROIs can be made globally uniform, or can be adjusted such that approximately the same number of nodes get included in the ROI of any given node I. Both these ideas have been successfully implemented in the BNM [Chati and Mukherjee (2000); Chati *et al.* (1999, 2001a)]. Of course, no such truncations are necessary with Cartesian co-ordinates and truncations have not been carried out in the EBNM (Fig. 20(a)). The fact that DODs and ROIs can, in general, include edges and corners, makes the choice of the functions $q_k(\mathbf{x})$ (in Eq. $(128)_2$) very interesting.

Variable basis approximations in the EBNM. Li and Aluru [2003] present a variable basis approach for solving the 2D Laplace's equation with the BCLM. This is an elegant approach in which reduced bases are appropriately employed in order to avoid singularity of the matrix $\mathbf{A}$. A disadvantage of this approach, as well as that of the standard BNM, is that discontinuities in the normal derivative of the potential function, across edges and corners, are not addressed properly — normal derivatives are modeled with continuous approximants, even across edges and corners. The present work attempts to combine the advantages of the variable basis approach [Li and Aluru (2003)], together with allowing discontinuities in $\tau = \partial u/\partial n$, in a new approach called the EBNM. The EBNM for 3D potential theory is described next.

The first step is to distinguish between singular and nonsingular clouds (DODs and ROIs are sometimes called clouds in this work — the term is taken from the work presented in Li and Aluru [2002, 2003]. A **straight cloud** (for 2D problems) is one in which the nodes lie on a straight line. Similarly, a **flat cloud** (for 3D problems) is one in which the nodes lie on a plane. A **curved cloud** is a smooth curve in 2D and a smooth surface in 3D problems. Finally, a **broken cloud** contains at least one corner in 2D and at least one edge or corner in 3D problems. *The approximants for u are identical in the variable basis BCM* [*Li and Aluru* (2003)] *and in the EBNM. They are, however, different for τ — the approximants for τ are continuous* (*same as those for u*) *in Li and Aluru* [2003] *but allow for jumps in τ across corners and edges in the EBNM. The specific approximants for the 3D EBNM, for potential theory, are given below.*

Bases for u and τ. A basis for a cloud must satisfy two competing requirements — it must be broad enough to include all cases, yet it must be narrow enough such that the matrices $\mathbf{A}$ and $\mathbf{C}$ in (133) are nonsingular.

First, a word of caution. In order for the matrices $\mathbf{A}$ and $\mathbf{C}$ to be invertible (for 3D problems), a flat cloud (or a flat segment of a broken cloud) must always contain 3 or more points, and all the points on it must not lie on a straight line.

The following bases are used for the various cases listed below.

Flat cloud: $\begin{cases} x_1 = c_1 \quad \text{or} \quad n_1x_1 + n_2x_2 = c_4 \quad \text{Basis } [1, x_2, x_3] \quad \text{for } \mathbf{p} \text{ and } \mathbf{q}, \\ x_2 = c_2 \quad \text{or} \quad n_2x_2 + n_3x_3 = c_5 \quad \text{Basis } [1, x_3, x_1] \quad \text{for } \mathbf{p} \text{ and } \mathbf{q}, \end{cases}$

All other flat clouds: Basis $[1, x_1, x_2]$ for $\mathbf{p}$ and $\mathbf{q}$,

All curved clouds: Basis $[1, x_1, x_2, x_3]$ for $\mathbf{p}$ and $\mathbf{q}$,

Broken cloud: Basis $\begin{cases} [1, x_1, x_2, x_3] & \text{for } \mathbf{p} \\ \text{see below} & \text{for } \mathbf{q}. \end{cases}$

Explanation for choice of basis for u on a broken cloud. It is assumed that $u(x_1, x_2, x_3) \in C^\infty$ in B. Let a point P on an edge on ∂B have co-ordinates (x_{10}, x_{20}, x_{30}) which, for simplicity, is written as (x_0, y_0, z_0). A Taylor series expansion for u about (x_0, y_0, z_0) is of the form:

$$u(x, y, z) = u(x_0, y_0, z_0) + u_x(x_0, y_0, z_0)(x - x_0) + u_y(x_0, y_0, z_0)(y - y_0) + u_z(x_0, y_0, z_0)(z - z_0) + \text{h.o.t.} \tag{138}$$

The affine approximation of u about P is of the form:

$$l(x, y, z) = a_0 + a_1x + a_2y + a_3z \tag{139}$$

which insures that a constant function, and the one with constant derivatives, can be well represented or approximated by (128).

Choice of basis for τ on a broken cloud. A general curved cloud segment has the equation $f(x_1, x_2, x_3) = 0$. Assuming $\boldsymbol{\nabla} u \in C^\infty$ in B, one has:

$$\tau = u_{,1}(x_1, x_2, x_3)n_1 + u_{,2}(x_1, x_2, x_3)n_2 + u_{,3}(x_1, x_2, x_3)n_3. \tag{140}$$

One can, therefore, use the basis $n_1[1, x_1, x_2, x_3] \cup n_2[1, x_1, x_2, x_3] \cup n_3[1, x_1, x_2, x_3]$ on a *general curved cloud segment* $f(x_1, x_2, x_3) = 0$.

Special cases: Flat segments of a broken cloud.

Plane P_1: $n_1x_1 = c_1$ Basis $n_1[1, x_2, x_3]$
Plane P_2: $n_2x_2 = c_2$ Basis $n_2[1, x_3, x_1]$
Plane P_3: $n_3x_3 = c_3$ Basis $n_3[1, x_1, x_2]$
Plane P_4: $n_1x_1 + n_2x_2 = c_4$ Basis $n_1[1, x_1 \text{ or } x_2, x_3] \cup n_2[1, x_1 \text{ or } x_2, x_3]$
Plane P_5: $n_2x_2 + n_3x_3 = c_5$ Basis $n_2[1, x_1, x_2 \text{ or } x_3] \cup n_3[1, x_1, x_2 \text{ or } x_3]$
Plane P_6: $n_3x_3 + n_1x_1 = c_6$ Basis $n_3[1, x_1 \text{ or } x_3, x_2] \cup n_1[1, x_1 \text{ or } x_3, x_2]$
Plane P_7: $n_1x_1 + n_2x_2 + n_3x_3 = c_7$ Basis $n_1[1, \text{two of } (x_1, x_2, x_3)] \cup n_2[1, \text{ two of } (x_1, x_2, x_3)] \cup n_3[1, \text{ two of } (x_1, x_2, x_3)]$

On a broken cloud, one must use a basis that is a union of the bases for its segments.

For a union of two flat segments, one has, for example:

$P_1 \cup P_2$: Basis $[n_1, n_1x_2, n_1x_3, n_2, n_2x_3, n_2x_1]$

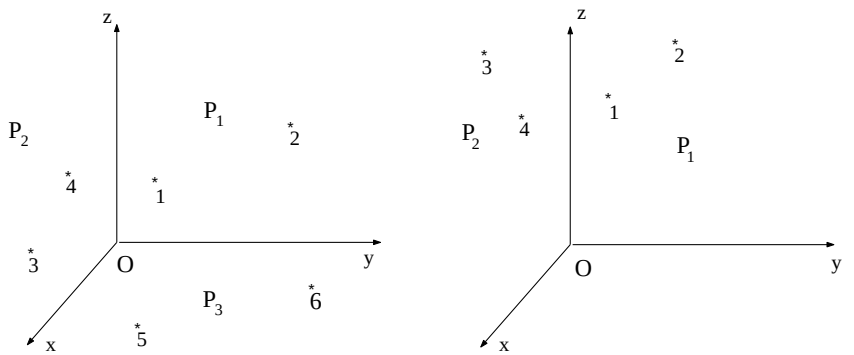

Fig. 21. Broken clouds (a) three planes meet at a corner O, (b) two planes meet at an edge (the z axis). Two points on each flat cloud segment (from Telukunta and Mukherjee [2005]).

$P_1 \cup P_4$: Basis $[n_1, n_1x_2, n_1x_3, n_2, n_2x_3, n_2x_1]$
$P_1 \cup P_5$: Basis $[n_1, n_1x_2, n_1x_3, n_2, n_2x_3, n_2x_1, n_3, n_3x_1, n_3x_2]$
$P_1 \cup P_7$: Basis $[n_1, n_1x_2, n_1x_3, n_2, n_2x_3, n_2x_1, n_3, n_3x_1, n_3x_2]$

For a union of three flat segments, one has, for example:

$P_1 \cup P_2 \cup P_3$: Basis $[n_1, n_1x_2, n_1x_3, n_2, n_2x_3, n_2x_1, n_3, n_3x_1, n_3x_2]$

Special cases: curved segments of a broken cloud.

S_1: $f_1(x_1, x_2) = 0$ Basis $[n_1, n_1x_1, n_1x_2, n_1x_3, n_2, n_2x_1, n_2x_2, n_2x_3]$
S_2: $f_2(x_2, x_3) = 0$ Basis $[n_2, n_2x_1, n_2x_2, n_2x_3, n_3, n_3x_1, n_3x_2, n_3x_3]$
S_3: $f_3(x_3, x_1) = 0$ Basis $[n_1, n_1x_1, n_1x_2, n_1x_3, n_3, n_3x_1, n_3x_2, n_3x_3]$
S_4: $f_4(x_1, x_2, x_3) = 0$ Basis $[n_1, n_1x_1, n_1x_2, n_1x_3, n_2, n_2x_1, n_2x_2, n_2x_3, n_3, n_3x_1, n_3x_2, n_3x_3]$

In the above, $f_k, k = 1, 2, 3, 4$, are nonlinear functions of some or all of their arguments.

On a broken cloud, one must use a basis that is a union of the bases for its segments.

For example:

$P_1 \cup S_1$: Basis $[n_1, n_1x_1, n_1x_2, n_1x_3, n_2, n_2x_1, n_2x_2, n_2x_3]$
$P_1 \cup S_2$: Basis $[n_1, n_1x_2, n_1x_3, n_2, n_2x_1, n_2x_2, n_2x_3, n_3, n_3x_1, n_3x_2, n_3x_3]$

Note that the case $P_1 \cup S_1$ is a 3D version of the 2D example in Fig. 2(b) of Telukunta and Mukherjee [2004].

Invertibility of $\mathbf{C = Q^T WQ}$ for $\boldsymbol{\tau}$ on a broken cloud. Two cases are considered below.

Three co-ordinate planes intersect. It is convenient to start with two points on each flat cloud segment (see Fig. 21(a)). Let $(x_1, x_2, x_3) \rightarrow (x, y, z)$ and $[n_1, n_2, n_3] \rightarrow [p, q, r]$. Referring to Fig. 21(a), one has:

$$\begin{gathered} x_1 = x_2 = 0, \quad y_3 = y_4 = 0 \quad z_5 = z_6 = 0 \\ p_1 = p_2 = q_3 = q_4 = r_5 = r_6 = -1; \quad \text{rest are zero.} \end{gathered} \tag{141}$$

The basis for this case, $P_1 \cup P_2 \cup P_3$, is $[n_1, n_1x_2, n_1x_3, n_2, n_2x_3, n_2x_1, n_3, n_3x_1, n_3x_2]$. This is written as $[p, py, pz, q, qz, qx, r, rx, ry]$. With this, one gets:

$$[Q] = \begin{bmatrix} -1 & -y_1 & -z_1 & 0 & 0 & 0 & 0 & 0 & 0 \\ -1 & -y_2 & -z_2 & 0 & 0 & 0 & 0 & 0 & 0 \\ 0 & 0 & 0 & -1 & -z_3 & -x_3 & 0 & 0 & 0 \\ 0 & 0 & 0 & -1 & -z_4 & -x_4 & 0 & 0 & 0 \\ 0 & 0 & 0 & 0 & 0 & 0 & -1 & -x_5 & -y_5 \\ 0 & 0 & 0 & 0 & 0 & 0 & -1 & -x_6 & -y_6 \end{bmatrix}, \tag{142}$$

$$[C] = \begin{bmatrix} M_1 & 0 & 0 \\ 0 & M_2 & 0 \\ 0 & 0 & M_3 \end{bmatrix}, \tag{143}$$

where

$$[M_1] = \begin{bmatrix} \sum_{P_1} w_i & \sum_{P_1} w_i y_i & \sum_{P_1} w_i z_i \\ \sum_{P_1} w_i y_i & \sum_{P_1} w_i y_i^2 & \sum_{P_1} w_i y_i z_i \\ \sum_{P_1} w_i z_i & \sum_{P_1} w_i y_i z_i & \sum_{P_1} w_i z_i^2 \end{bmatrix}, \tag{144}$$

$$[M_2] = \begin{bmatrix} \sum_{P_2} w_i & \sum_{P_2} w_i z_i & \sum_{P_2} w_i x_i \\ \sum_{P_2} w_i z_i & \sum_{P_2} w_i z_i^2 & \sum_{P_2} w_i z_i x_i \\ \sum_{P_2} w_i x_i & \sum_{P_2} w_i z_i x_i & \sum_{P_2} w_i x_i^2 \end{bmatrix}, \tag{145}$$

$$[M_3] = \begin{bmatrix} \sum_{P_3} w_i & \sum_{P_3} w_i x_i & \sum_{P_3} w_i y_i \\ \sum_{P_3} w_i x_i & \sum_{P_3} w_i x_i^2 & \sum_{P_3} w_i x_i y_i \\ \sum_{P_3} w_i y_i & \sum_{P_3} w_i x_i y_i & \sum_{P_3} w_i y_i^2 \end{bmatrix}. \tag{146}$$

The zero blocks in $\mathbf{C}$ are 3×3 matrices.

It is interesting to note that Eqs. (143)–(146) remain true irrespective of the number of points on each flat cloud segment on $P_k, k = 1, 2, 3$. It is easy to show that the matrix $\mathbf{C}$ is singular if and only if all points in any flat cloud segment are colinear. Obviously, each flat cloud segment must contain at least 3 points. If $\mathbf{C}$ becomes singular, the DOD must be extended to include more points such that each flat cloud segment contains a set of points that do not lie on a straight line.

Two co-ordinate planes intersect. One starts again with two points on each flat cloud segment. Referring to Fig. 21(b), one has:

$$\begin{aligned} x_1 = x_2 = 0, \quad y_3 = y_4 = 0 \\ p_1 = p_2 = q_3 = q_4 = -1; \quad \text{rest are zero.} \end{aligned} \tag{147}$$

The basis for this case, $P_1 \cup P_2$, is $[n_1, n_1x_2, n_1x_3, n_2, n_2x_3, n_2x_1]$. This is written as $[p, py, pz, q, qz, qx]$. With this, one gets:

$$[Q] = \begin{bmatrix} -1 & -y_1 & -z_1 & 0 & 0 & 0 \\ -1 & -y_2 & -z_2 & 0 & 0 & 0 \\ 0 & 0 & 0 & -1 & -z_3 & -x_3 \\ 0 & 0 & 0 & -1 & -z_4 & -x_4 \end{bmatrix}, \tag{148}$$

$$[C] = \begin{bmatrix} M_1 & 0 \\ 0 & M_2 \end{bmatrix}, \tag{149}$$

where the matrices M_1 and M_2 are the same as those in Eqs. (144) and (145). Also, the zero blocks in $\mathbf{C}$ are 3×3 matrices.

The matrix $\mathbf{C}$ in (149) remains the same irrespective of the number of points on each flat cloud segment on $P_k, k = 1, 2$. Again, the matrix $\mathbf{C}$ becomes singular if all the points on any of the flat cloud segments are colinear; and this singularity can be avoided by suitably extending the DOD.

Coupling of BIE with MLS interpolants. The MLS interpolants are next coupled with the appropriate BIE.

Boundary integral equations for potential theory. The regularized BIE for 3D potential theory is (8).

Extended boundary node method for potential theory. The boundary ∂B of the body B is partitioned into N_c cells ∂B_k and the MLS approximations (134) for the functions u and τ are used in the usual BIE for potential theory (8). The result is:

$$\begin{aligned} 0 = \sum_{k=1}^{N_c} \int_{\partial B_k} \Bigg[& G(\mathbf{x}, \mathbf{y}) \sum_{I=1}^{n_y} N_I(\mathbf{y}) \hat{\tau}_I \\ & - F(\mathbf{x}, \mathbf{y}) \left\{ \sum_{I=1}^{n_y} M_I(\mathbf{y}) \hat{u}_I - \sum_{I=1}^{n_x} M_I(\mathbf{x}) \hat{u}_I \right\} \Bigg] dS(\mathbf{y}), \end{aligned} \tag{150}$$

where $M_I(\mathbf{x})$ and $M_I(\mathbf{y})$ are the contributions from the Ith node to the collocation (source) point $\mathbf{x}$ and field point $\mathbf{y}$ respectively. Also, n_y nodes lie in the DOD of the field point $\mathbf{y}$ and n_x nodes lie in the DOD of the source point $\mathbf{x}$. When $\mathbf{x}$ and $\mathbf{y}$ belong to the same cell, the cell is treated as a singular cell and special techniques are needed to numerically evaluate the weakly singular integrals that involve the kernel $G(\mathbf{x}, \mathbf{y})$. This method is described in detail below.

Numerical evaluation of singular and regular integrals. One has to deal with strongly singular ($\mathcal{O}(1/r^2)$), weakly singular ($\mathcal{O}(1/r)$) as well as regular integrals in this work. Strongly singular integrals are made weakly singular by multiplying the F kernel by the $\mathcal{O}(r)$ function $u(\mathbf{y}) - u(\mathbf{x})$ (see (8)). Weakly singular integrals are regularized by a mapping method [Nagarajan and Mukherjee (1993); Chati and Mukherjee (2000); Mukherjee and Mukherjee (2005)]. This method is outlined below.

Consider evaluating the integral with $G(\mathbf{x}, \mathbf{y})$ in (8) over a (in general curved) surface cell as shown in Fig. 22(a). These cells, in general, are nonplanar (quadratic) triangles with their shapes defined by the six points shown in Fig. 22(a). A cell is entirely contained in a panel. This integral can be represented as:

$$I = \int_{\partial B} O(1/r) dS_Q. \tag{151}$$

The cell shown in Figs. 22(a) and 22(b) contains the source point $\mathbf{x}$ (called P in these figures), so that the field point $\mathbf{y}$ could coincide with the collocation point $\mathbf{x}$. Although quadratic (T6) triangles are used here to describe the geometry of a cell, the method described here can be easily extended to model various other kinds of geometric representations for it.

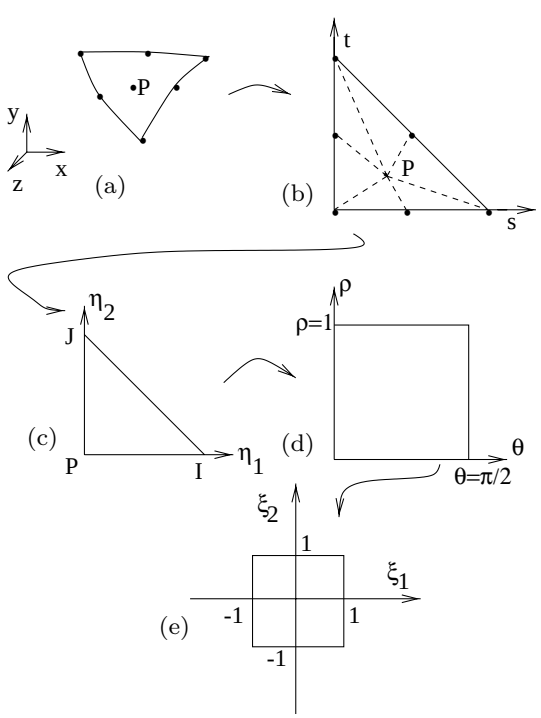

Fig. 22. Mapping scheme for the evaluation of weakly singular integrals (from Mukherjee and Mukherjee [2005]).

First, the cell is mapped into the master triangle (Fig. 22(b)) using the well-known shape functions for T6 triangles. This involves a Jacobian J_1 and the integral I takes the form:

$$I = \int_{t=0}^{t=1} \int_{s=0}^{s=1-t} O(1/r) J_1 \, ds \, dt. \tag{152}$$

Now, the master triangle is divided into n_t triangles. ($n_t = 6$ in Fig. 22(b) while $n_t = 3$ is used in this work. For $n_t = 3$, the source point P is connected to each vertex of the master triangle). Each individual small triangle is mapped into the parametric $(\eta_1 - \eta_2)$ space (Fig. 22(c)) using the mapping for linear (T3) triangles. The integral I can now be written as:

$$I = \sum_{i=1}^{n_t} \int_{\eta_2=0}^{\eta_2=1} \int_{\eta_1=0}^{\eta_1=1-\eta_2} O(1/r) J_1 J_2^{(i)} d\eta_1 \, d\eta_2, \tag{153}$$

where $J_2^{(i)}$ is the Jacobian for each triangle. Now, consider the mapping [Nagarajan and Mukherjee (1993)]:

$$\eta_1 = \rho \cos^2 \theta, \quad \eta_2 = \rho \sin^2 \theta, \tag{154}$$

which maps the flat triangle from the $\eta_1 - \eta_2$ space into a rectangle in the ρ–θ space (Fig. 22(d)). The integral I now takes the form:

$$I = \sum_{i=1}^{n_t} \int_{\theta=0}^{\theta=\pi/2} \int_{\rho=0}^{\rho=1} O(1/r) J_1 J_2^{(i)} \rho \sin\theta \, d\rho \, d\theta. \tag{155}$$

As ρ is a measure of the distance between the source point and the field point, the integral I is now regularized. In other words, the ρ in the numerator cancels the $\mathcal{O}(1/r)$ singularity. The final mapping involves the use of quadratic (Q4) shape functions to map the rectangle from the ρ–θ space into the master square in ξ_1–ξ_2 space (Fig. 22(e)). The final form of the integral I is:

$$I = \sum_{i=1}^{n_t} \int_{\xi_2=-1}^{\xi_2=1} \int_{\xi_1=-1}^{\xi_1=1} O(1/r) J_1 J_2^{(i)} J_3 \rho \sin\theta \, d\xi_1 \, d\xi_2, \tag{156}$$

where J_3 is the Jacobian of the final transformation. Finally, regular Gaussian integration can be used to evaluate the above integral I.

The approach described above, for the evaluation of weakly singular integrals, is also employed for the evaluation of regular integrals in this work. This time, subdivision of the triangle in Fig. 22(b) is no longer necessary. The rest of the procedure remains the same as described above.

The square in Fig. 22(e) is called the final square in the rest of this section.

Assembly of equations and treatment of boundary conditions. The final assembled equations from the EBNM are of the form:

$$[\mathbf{K_1}]\{\hat{\mathbf{u}}\} + [\mathbf{K_2}]\{\hat{\boldsymbol{\tau}}\} = 0, \quad N_B \text{ equations}, \tag{157}$$

where N_B is the number of boundary nodes. Equation (157) contains approximations, to the nodal values, of the potentials (the vector $\hat{\mathbf{u}}$) and the normal derivatives (the vector $\hat{\boldsymbol{\tau}}$) on ∂B.

It is assumed that in a general mixed boundary value problem, either u or τ is prescribed at each boundary node. Let the vector $\{\bar{\mathbf{y}}\}$ contain the prescribed boundary conditions and $\{\mathbf{x}\}$ contain the rest. Each of these vectors is of length N_B. Also let $\{\hat{\mathbf{y}}\}$ and $\{\hat{\mathbf{x}}\}$ be their corresponding approximations. Finally, let $\{\hat{\mathbf{z}}\} = (\{\hat{\mathbf{u}}\} \cup \{\hat{\boldsymbol{\tau}}\})$.

Equation (157) is now written as:

$$[\mathbf{M}]\{\hat{\mathbf{z}}\} = \{0\}, \quad N_B \text{ equations.} \tag{158}$$

Referring to Eq. (136), the nodes with prescribed quantities are considered first. This gives rise to a system of equations of the form:

$$[\mathbf{H_1}]\{\hat{\mathbf{z}}\} = \{\bar{\mathbf{y}}\}, \quad N_B \text{ equations.} \tag{159}$$

Equations (158) and (159) are now solved together for $2N_B$ unknowns $\hat{z}_k$. Finally, (as a post-processing step) consideration of the rest of the boundary nodes (those without prescribed boundary conditions) results in the equations:

$$\{\mathbf{x}\} = [\mathbf{H_2}]\{\hat{\mathbf{z}}\}, \quad N_B \text{ equations,} \tag{160}$$

which yield the required boundary values x_k.

4.2.4. *Numerical results*

Numerical results are presented below for Dirichlet problems and for one mixed problem for Laplace's equation in 3D. Dirichlet problems are chosen in order to test the ability of the new algorithm to model discontinuities across corners, if any, in $\tau = \partial u/\partial n$, with prescribed values of u on the boundary.

The L_2 error for the Dirichlet problems is defined as:

$$\epsilon = \frac{\sqrt{\sum_{i=1}^{N_B} (\tau_i^{(\text{exact})} - \tau_i^{(\text{num})})^2}}{\sqrt{N_B} |\tau_i^{(\text{exact})}|_{\max}} \times 100, \tag{161}$$

where N_B is the total number of boundary nodes.

Standard Gauss integration (with $N \times N$ Gauss points in the final square) is employed for the numerical evaluation of regular integrals. For the evaluation of *regularized* weakly singular integrals, each master triangle is divided into 3 triangles, and $N \times N$ Gauss points are used in each final square, for a total of $3N^2$ Gauss points. Unless otherwise mentioned, $N = 4$ is used for all the numerical examples.

Problems on a cube. The first set of problems involves a unit cube with Dirichlet boundary conditions. Prescribed values on the boundary of a cube are obtained from

the following exact solutions of Laplace's equation:

$$(1) \quad \text{“linear cube”} \qquad u = x_1 + x_2 + x_3, \tag{162}$$

$$(2) \quad \text{“sinsinh cube”} \qquad u = \sinh\left(\frac{\pi x_1}{2}\right) \sin\left(\frac{\pi x_2}{2\sqrt{2}}\right) \sin\left(\frac{\pi x_3}{2\sqrt{2}}\right). \tag{163}$$

A schematic of the cube with a typical surface mesh appears in Fig. 23(a). Each face of the cube is first divided into equal squares, and then into triangles. One node is placed at the centroid of each cell.

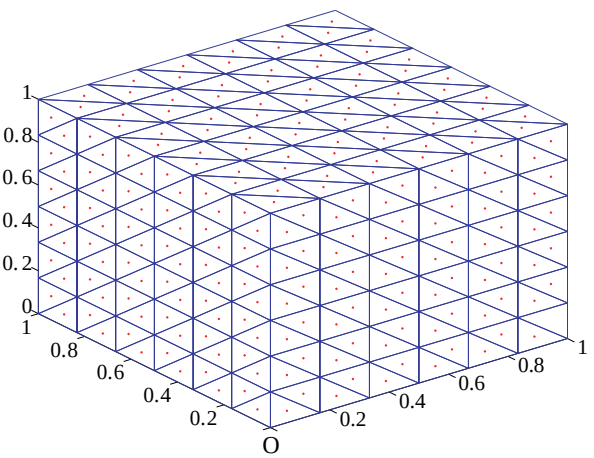

(a)

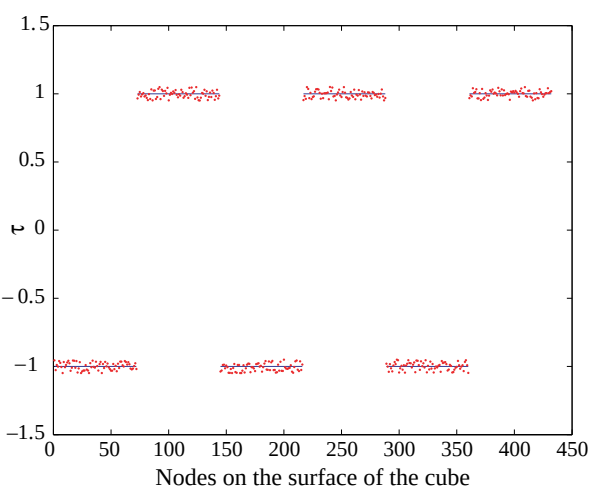

(b)

Fig. 23. (Color online) Cube problem (a) cube with 72 triangular (T3) cells on each face; one centroidal node on each cell (b) τ at nodes on the surface of the cube (—) exact solution (.....) EBNM solution (from Telukunta and Mukherjee [2005]).

The "linear cube". For this problem, 72 triangular (T3) cells are used on each face of the cube. Numerical results for $\tau \in \partial B$, from the EBNM, are compared with the exact solution in Fig. 23(b). The value of d_I in Eq. (137) for this calculation is 0.2357 units. The exact solution for τ is 1 on three faces and -1 on the others. The EBNM captures well the jumps in τ across all the edges of the cube. There are, however, small oscillations in the EBNM solution. The reasons for this require further investigation.

The value of the L_2 error in this example is 2.72%.

The "sinsinh" cube. Results obtained for this problem are summarized in Table 6. The value of d_I is adjusted such that there are, approximately, 14–16 nodes within the DOD of each evaluation point. The results are seen to be quite satisfactory.

Problems on a sphere and on an octant of a sphere. A sphere, and an octant of a sphere, with generic surface meshes, are shown in Figs. 24(a) and 24(b), respectively. A Dirichlet problem on the sphere is defined by prescribing the following exact solution of the 3D Laplace equation on the sphere surface [Mukherjee and Mukherjee (2005)]:

$$u = \frac{2r^2}{R^2}\cos^2\phi - \frac{2r^2}{3R^2} - \frac{1}{3}, \tag{164}$$

where R is the radius of the sphere, ϕ is the angle measured from the x_3 axis and $r^2 = x_1^2 + x_2^2 + x_3^2$.

Of course, the sphere has a smooth surface and the primary reason for solving this problem is to set up the next one on an octant of a sphere. With 128 uniform $T6$ cells on the sphere surface, and $d_I = 0.6$, the ENBM delivers an L_2 error of 0.5393%.

The next problem is a mixed boundary value problem on an octant of a sphere (Fig. 24(b)). This problem is very important because it could not be solved by the standard BNM in which curvilinear surface co-ordinates were used and ROIs were truncated at the edges. For this problem, the function u, obtained from (164), is again prescribed on the curved surface, while $\tau = 0$ is prescribed on the three flat surfaces.

Table 6. L_2 errors for the EBNM for the "sinsinh" cube problem as a function of discretization. 4×4 Gauss points are used (in the final square) for regular and $3 \times 4 \times 4$ Gauss points for regularized weakly singular integration.

T3 cells/face	d_I	ϵ (%)
9	0.4718	2.4119
16	0.3535	2.5053
25	0.2829	1.7041

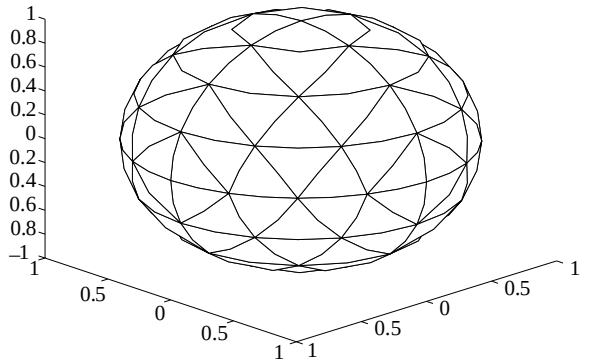

(a)

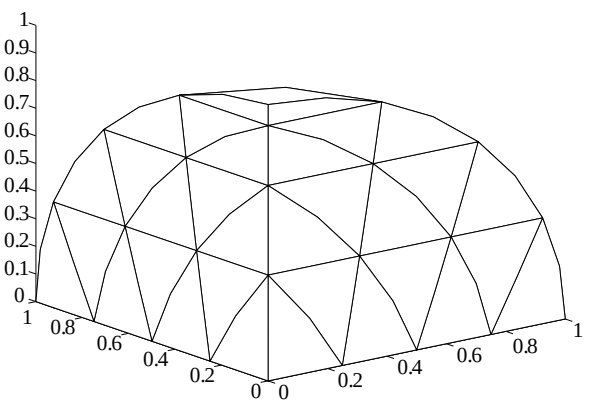

(b)

Fig. 24. (a) A sphere (b) an octant of a sphere (from Telukunta and Mukherjee [2005]).

This time, 16 T6 cells are used on the curved surface, as well as on each of the three flat surfaces, for a total of 64 cells. The cells are uniform on a given panel and $d_I = 0.6$. The L_2 error is still defined by (161) but $N_B = 16$ are the nodes on the curved surface at which the function u is prescribed. The L_2 error obtained in this case is 4.595%.

Problem on a cylinder. The final problem concerns a cylinder with a radius of 1 unit and height 3 units (see Fig. 25(a)). A Dirichlet problem is defined by prescribing the following function on the surface of the cylinder:

$$u = x_1^2 + x_2^2 + x_3^2. \tag{165}$$

It is noted that $\hat{u} = x_1^2 + x_2^2 + x_3^2 - 6$ is an exact solution of the 3D Laplace equation, and that $\frac{\partial u}{\partial n} = \frac{\partial \hat{u}}{\partial n}$; so that it is easy to determine the exact solution for $\frac{\partial u}{\partial n}(\mathbf{x})$ with $\mathbf{x} \in \partial B$.

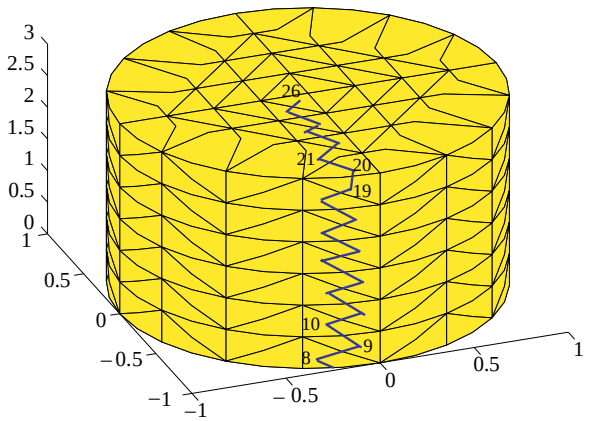

(a)

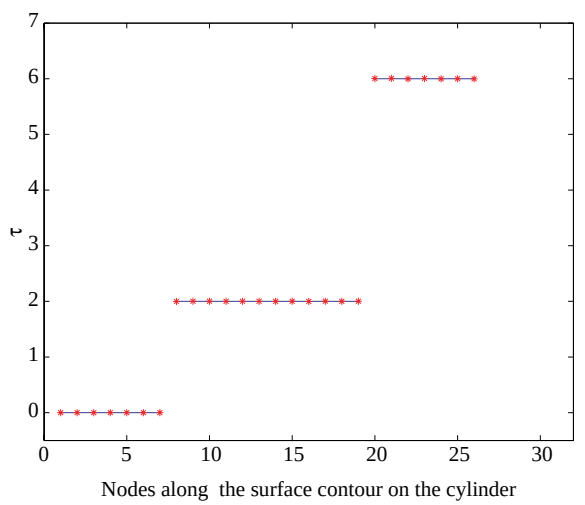

(b)

Fig. 25. (Color online) (a) Nodes (at centroids of triangular surface cells) along a surface contour on a cylinder (radius = 1 unit, height = 3 units). 320 $T6$ cells are used with 1 node per cell. $d_I = 0.3537$. Nodes 1–7 lie on the bottom surface $x_3 = 0$. (b) Normal derivative τ along the surface contour shown in Fig. 25(a). (—) Exact solution, ($\star\star\star$) EBNM solution (from Telukunta and Mukherjee [2005]).

A contour, connecting cell centroids on the cylinder surface, is shown in Fig. 25(a). The normal derivative τ at these centroids along this contour, obtained from the EBNM, is compared with the exact solution in Fig. 25(b). Excellent results are obtained — the jumps in τ are obtained perfectly within plotting accuracy.

Dependence of solution accuracy on the order of integration is shown in Table 7. It is seen that the EBNM solution is very good for all cases.

Table 7. L_2 errors for the EBNM for the cylinder problem for different orders of integration. Regular integrals are evaluated with $N \times N$ and regularized weakly singular integrals with $3 \times N \times N$ Gauss points (on the final square). 216 $T6$ cells are used with 1 node per cell. $d_I = 0.3537$.

Gauss points, N	ϵ (%)
2	0.834
4	0.319
6	0.276

4.2.5. *Discussion*

A few general issues, pertaining to the BEM and the BNM are discussed first. This is followed by a discussion of the EBNM.

Meshing issues pertaining to the BEM and the BNM. It is well known that surface meshing (that suffices for BEM applications in linear problems) is much easier than (3D) domain meshing (as is typically required for the FEM). One might then wonder about the need for a (pseudo) mesh-free version of the BEM. It is important to point out, however, that certain situations, such as problems with moving boundaries, or those in which optimal shape design and/or adaptive meshing is carried out, typically require multiple remeshings during the solution process. This process can be painful even for the BEM. The BNM has a very flexible cell structure — the cells, used just for integration, only need to cover the surface of a body and not overlap — no other topological restrictions are imposed. Therefore, this method offers an attractive alternative to the standard BEM, especially for this class of problems. As an illustration of the power of the BNM, the initial and final cell distribution on a cube, from an ONE-step adaptive (standard) BNM calculation for 3D potential theory [Chati *et al.* (2001a)], is reproduced as Fig. 26 in this paper. This is, in fact, a Dirichlet problem with the prescribed potential on the cube surface given by Eq. (163). The advantage of a flexible cell structure is apparent in Fig. 26(b) in which the cube surface has 1,764 cells of different sizes.

Computational efficiency of the BNM. The MLS interpolants, used in this work, can prove to be computationally expensive. Several ideas for acceleration of the BNM, however, exist. Perhaps the most promising is the use of FMM to accelerate the BNM. This FMM is presented, in some detail, in Sec. 4.3 of this paper.

There are ideas at the local level that can be employed to improve the efficiency of the BNM. A simple one is to obtain the DOD of the centroid of a cell, and then to use this DOD for each of its Gauss points (rather than computing the DOD separately for each Gauss point in the cell). This idea looks promising for simple problems and will be investigated further. Another possibility is the use of weighted

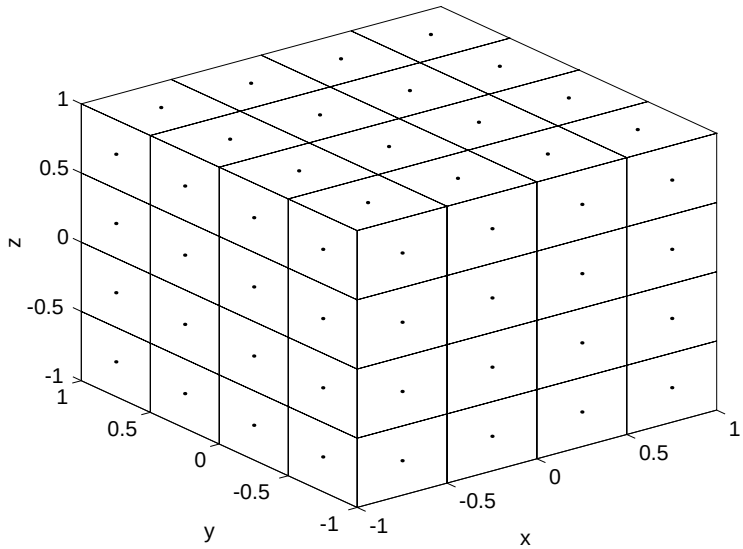

(a)

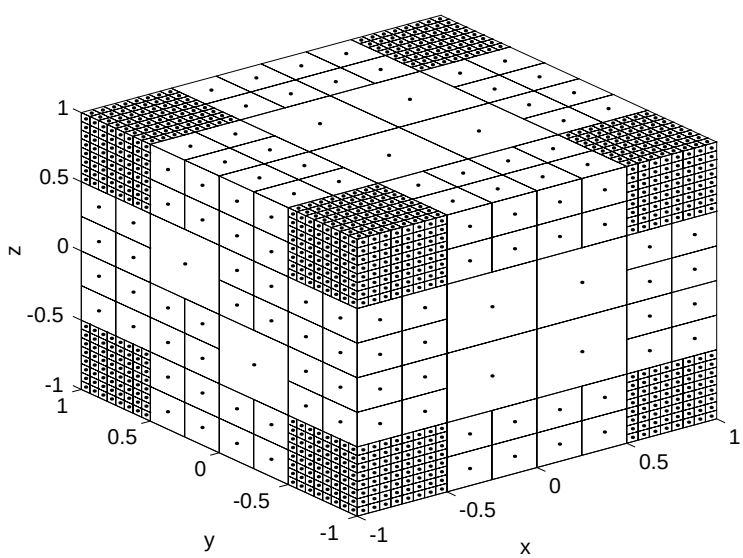

(b)

Fig. 26. ONE-step multilevel BNM cell refinement for the "sinsinh cube" problem (a) initial configuration with 96 surface cells (b) final adapted configuration (obtained in one step) with 1,764 surface cells (from Chati *et al.* [2001a]).

orthogonal polynomials to make the matrices **A** and **C** in Eq. (133) diagonal! This idea has been proposed in Kitipornchai *et al.* [2005].

Performance of the EBNM. The performance of the EBNM, for 3D Dirichlet problems on boundaries with edges and corners, is encouraging. Several important issues are discussed below.

(1) If curvilinear surface co-ordinates are employed for 3D problems (as in the original BNM), the use of broken clouds appears, in general, to be impossible (at least to SM). The use of Cartesian co-ordinates provides this opportunity.
(2) Use of Cartesian rather than curvilinear co-ordinates is easier and the 3D EBNM exhibits superior performance on problems with edges and corners, as compared to the original 3D BNM [Chati and Mukherjee (2000)].
(3) BNM results for 3D potential theory and linear elasticity have been reported before [Chati and Mukherjee (2000); Chati *et al.* (1999)]. This work, with curvilinear boundary surface co-ordinates, has clouds that are terminated at the edges (when they exist) of the bounding surface of a 3D body. Results for cubes are excellent. A problem on an octant of a sphere, whose boundary contains edges on which a flat surface meets a curved one, could not, however, be solved by the original BNM, but is solved successfully by the EBNM.
(4) On the whole, the EBNM does well in the matter of modeling of jumps across edges, but exhibits small oscillations on smooth boundary segments. The reasons for this behavior is a matter of further investigation. It is possible that use of higher order background bases, as opposed to the linear ones employed here, will alleviate this problem.
(5) Another interesting issue is that of the use of geodesics versus Euclidean distances, between nodes and evaluation points, in the BNM and the EBNM. Use of geodesics appears to work universally in all problems that have been tried so far, at least by Mukherjee and his collaborators, and is strongly recommended. Under certain conditions, the much simpler idea of using Euclidean distances appears to suffice. One such instance is the case of distances measured on smooth clouds that have "relatively gentle" curvature (see, e.g., 3D results in Chati *et al.* [2001b]). Another is the case of cubes. Finally, results for the octant of a sphere (see Sec. 4.2.4) have also been obtained with Euclidean distances in this work.

It is conceivable that the 3D EBNM will require the use of geodesics for complicated boundary value problems. It is important to mention, however, that computation of geodesics is an essential component of the original BNM — they are used for searching for nodes in a DOD, in a weight function, and in the curvilinear co-ordinates themselves. By contrast, only the first two tasks require geodesics in the EBNM. It is expected that approximate geodesics, e.g., use of Euclidean distances to replace geodesics on smooth curved segments of broken clouds, will suffice in the

EBNM. This idea would greatly simplify any implementation of the EBNM for 3D problems.

4.3. *Fast multipole BEM*

The BEM (and the related methods BCM and BNM) has been limited to solving problems with only a few thousand DOF on a PC for many years. This is because the conventional BEM produces dense and nonsymmetric matrices that, although typically smaller in size as compared to the FEM, require $\mathcal{O}(N^2)$ operations to compute the coefficients and $\mathcal{O}(N^3)$ operations to solve the system using direct solvers (where N is the number of equations in a linear system).

In the mid 1980s, Rokhlin and Greengard [Rokhlin (1995); Greengard and Rokhlin (1987); Greengard (1988)] pioneered the innovative FMM that can be used to accelerate the solutions of the BEM several times over the conventional BEM approach, promising to reduce the CPU time in the FMM accelerated BEM to $\mathcal{O}(N)$. With the help of the FMM, the BEM can now solve large-scale problems. Some of the early work on the fast multipole BEM in mechanics appeared in the 1990s [Pierce and Napier (1995); Gomez and Power (1997); Fu *et al.* (1998); Nishimura *et al.* (1999); Mammoli and Ingber (1999)]. The work demonstrates the great promise of the fast multipole BEM for solving large-scale problems. A comprehensive review of FMM research up to 2002 can be found in Nishimura [2002] and a first book on the FMM and the BEM has been recently published [Liu (2009)].

4.3.1. *Basic ideas in the fast multipole method*

A BEM system of equations for potential theory problems (see (8)) can be written as:

$$\begin{bmatrix} f_{11} & f_{12} & \cdots & f_{1N} \\ f_{21} & f_{22} & \cdots & f_{2N} \\ \cdots & \cdots & \cdots & \cdots \\ f_{N1} & f_{N2} & \cdots & f_{NN} \end{bmatrix} \begin{Bmatrix} \phi_1 \\ \phi_2 \\ \cdots \\ \phi_N \end{Bmatrix} = \begin{bmatrix} g_{11} & g_{12} & \cdots & g_{1N} \\ g_{21} & g_{22} & \cdots & g_{2N} \\ \cdots & \cdots & \cdots & \cdots \\ g_{N1} & g_{N2} & \cdots & g_{NN} \end{bmatrix} \begin{Bmatrix} q_1 \\ q_2 \\ \cdots \\ q_N \end{Bmatrix}, \tag{166}$$

where ϕ_i and q_i are the potential and its normal derivative, respectively, at boundary node i, and g_{ij} and f_{ij} are the coefficients computed using the G and F kernel, respectively. After applying the boundary conditions, a standard linear system of equations is formed as follows by switching the columns in the two matrices in Eq. (166):

$$\begin{bmatrix} a_{11} & a_{12} & \cdots & a_{1N} \\ a_{21} & a_{22} & \cdots & a_{2N} \\ \cdots & \cdots & \cdots & \cdots \\ a_{N1} & a_{N2} & \cdots & a_{NN} \end{bmatrix} \begin{Bmatrix} \lambda_1 \\ \lambda_2 \\ \cdots \\ \lambda_N \end{Bmatrix} = \begin{Bmatrix} b_1 \\ b_2 \\ \cdots \\ b_N \end{Bmatrix}, \quad \text{or} \quad \mathbf{A}\boldsymbol{\lambda} = \mathbf{b}, \tag{167}$$

where $\mathbf{A}$ is the coefficient matrix, $\boldsymbol{\lambda}$ the unknown vector and $\mathbf{b}$ the known RHS vector. Obviously, the construction of matrix $\mathbf{A}$ requires $\mathcal{O}(N^2)$ operations and the

size of the required memory for storing $\mathbf{A}$ is also $\mathcal{O}(N^2)$ since $\mathbf{A}$, in general, is a nonsymmetric and dense matrix. The solution time of the system (167) using direct solvers such as Gauss elimination is even worse, requiring $\mathcal{O}(N^3)$ operations because of this general matrix. Even with iterative solvers, the solution requires $\mathcal{O}(N^2)$ operations. That is why the conventional BEM approach for solving the BIEs is, in general, slow and inefficient for large-scale problems, despite its robustness in the meshing stage as compared with domain based methods.

The main idea of the fast multipole BEM is to apply iterative solvers (such as GMRES [Saad and Schultz (1986)]) to solve Eq. (167) and employ the FMM to accelerate the matrix-vector multiplication $\mathbf{A}\boldsymbol{\lambda}$ in each iteration, without forming the entire matrix $\mathbf{A}$ explicitly. Direct integrations are still needed when the elements are close to the source point, while fast multipole expansions are used for elements that are far away from the source point. Figure 27 is a graphical illustration of the fast multipole BEM as compared with the conventional BEM. For the far field calculations, the node-to-node (or element-to-element) interactions in the conventional BEM (Fig. 27(a)) are replaced by cell-to-cell interactions (Fig. 27(b)) by using a hierarchical tree structure of cells containing groups of elements (in Fig. 27, the dots indicate nodes/cells and lines indicate the interactions needed). This is possible by using the multipole and local expansions of the integrals and some translations to be discussed in the following section. The numbers of lines represent the computational complexities of the two approaches and dramatic decrease of operations in the fast multipole BEM is obvious from this illustration.

A fundamental reason for the reduction in operations in the fast multipole BEM, as shown in Fig. 27(b), is due to the fact that Green's functions or the kernels in the BIEs can be expanded in the following form:

$$G(\mathbf{x}, \mathbf{y}) = \sum_i G_i^x(\mathbf{x}, \mathbf{y}_c) G_i^y(\mathbf{y}, \mathbf{y}_c), \tag{168}$$

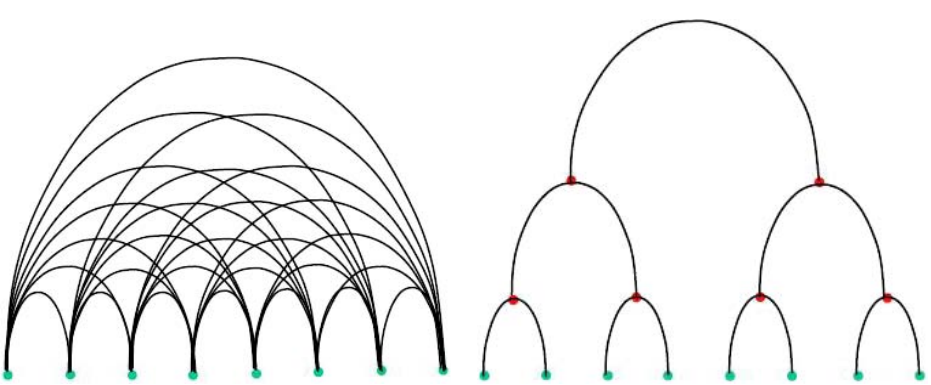

(a) Conventional BEM approach ($O(N^2)$)

(b) Fast multipole BEM approach ($O(N)$) for large N)

Fig. 27. (Color online) A graphical illustration of the conventional BEM and the fast multipole BEM (from Liu [2009]).

where $\mathbf{y}_c$ is an expansion point. This can be achieved by using various forms of expansions, including but not limited to Taylor series expansions. By using an expansion as in Eq. (168), the original integral, such as the one with the G kernel in the BIE for potential theory problems, can be written as:

$$\int_{\partial B_c} G(\mathbf{x},\mathbf{y})q(\mathbf{y})dS(\mathbf{y}) = \sum_i G_i^x(\mathbf{x},\mathbf{y}_c)\int_{\partial B_C} G_i^y(\mathbf{y},\mathbf{y}_c)q(\mathbf{y})dS(\mathbf{y}), \qquad (169)$$

where ∂B_c is a subset of ∂B away from $\mathbf{x}$. In the conventional BEM, the integral is computed using the expression on the LHS of Eq. (169) directly. Any changes in the location of the source point $\mathbf{x}$ will require re-evaluation of the entire integral. In the fast multipole BEM, when the source point $\mathbf{x}$ is far away from ∂B_c, the original integral is computed using the expression on the RHS of Eq. (169), in which the new integrals only need to be evaluated once, independent of the location of the source point $\mathbf{x}$. In other words, the direct relation between $\mathbf{x}$ and $\mathbf{y}$ is cut off by using the expansion and introduction of the new "middle" point $\mathbf{y}_c$. Additional expansions and translations, as well as the hierarchical tree structure of the elements, are introduced in the fast multipole BEM to further reduce computational costs. Using the fast multipole method for the BEM, the solution time can be reduced to order $\mathcal{O}(N)$ for large-scale problems [Nishimura (2002)]. The memory requirement can also be reduced to $\mathcal{O}(N)$ since with iterative solvers the entire matrix does not need to be stored in the memory. This drastic improvement in computing efficiency has presented many opportunities for the BEM. Large BEM models with a couple of millions of DOF, that could not be solved by the conventional BEM before, can now be readily solved using the fast multipole BEM within hours on a PC and BEM models with tens of millions of DOF can be solved on a supercomputer.

4.3.2. *Fast multipole BEM for 2D problems*

Fast multipole BEM for 2D problems can be developed using complex variable notation. The 2D potential problem is used as an example.

Consider the following integral with the G kernel for the 2D potential problem:

$$\int_{\partial B_c} G(\mathbf{x},\mathbf{y})q(\mathbf{y})dS(\mathbf{y}), \qquad (170)$$

in which the fundamental solution G is given in (64) and ∂B_c is a subset of the boundary ∂B away from the source point $\mathbf{x}$.

For convenience, introduce complex notation in 2D, that is, replace the source point $\mathbf{x} \Rightarrow z_0 = x_1 + ix_2$, and the field point $\mathbf{y} \Rightarrow z = y_1 + iy_2$, in the complex plane, where $i = \sqrt{-1}$ (Fig. 28). Using complex notation, one can write:

$$G(\mathbf{x},\mathbf{y}) = \mathrm{Re}\{G(z_0,z)\}, \qquad (171)$$

where

$$G(z_0,z) = -\frac{1}{2\pi}\log(z_0 - z), \qquad (172)$$

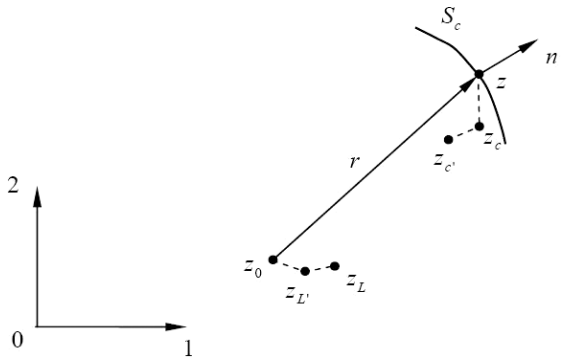

Fig. 28. Complex notation and related points for fast multipole expansions (from Liu [2009]).

is the fundamental solution in complex notation and Re{ } indicates the real part of the variable or function. Thus, the integral in Eq. (170) is equivalent to the real part of the following integral:

$$\int_{\partial B_c} G(z_0, z) q(z) dS(z), \tag{173}$$

where $q(z)$ is still a real-valued function of complex variable z.

Several important concepts in the FMM are presented next.

Multipole expansion (Moments). The first idea is to expand the kernel function to see if one can separate the source point z_0 and field point z. To do this, introduce an expansion point z_c that is close to the field point z (Fig. 28), that is, $|z - z_c| \ll |z_0 - z_c|$. One can write:

$$G(z_0, z) = -\frac{1}{2\pi} \log(z_0 - z) = -\frac{1}{2\pi} \left[\log(z_0 - z_c) + \log\left(1 - \frac{z - z_c}{z_0 - z_c}\right) \right]. \tag{174}$$

Applying the following Taylor series expansion:

$$\log(1 - \xi) = -\sum_{k=1}^{\infty} \frac{\xi^k}{k}, \quad \text{for } |\xi| < 1, \tag{175}$$

to the second logarithmic term on the RHS of Eq. (174), one obtains:

$$G(z_0, z) = \frac{1}{2\pi} \sum_{k=0}^{\infty} O_k(z_0 - z_c) I_k(z - z_c). \tag{176}$$

In the above, two auxiliary functions $I_k(z)$ and $O_k(z)$ are introduced. These are defined as:

$$I_k(z) = \frac{z^k}{k!}, \qquad \text{for } k \geq 0, \tag{177}$$

$$O_k(z) = \frac{(k-1)!}{z^k}, \quad \text{for } k \geq 1; \quad \text{and} \quad O_0(z) = -\log(z). \tag{178}$$

The derivatives of these functions satisfy the equations:

$$I_k'(z) = I_{k-1}(z) \qquad \text{for } k \geq 1; \text{ and } I_0'(z) = 0, \tag{179}$$

$$O_k'(z) = -O_{k+1}(z) \quad \text{for } k \geq 0. \tag{180}$$

Note that in the G kernel given in Eq. (176), z_0 and z are now separated due to the introduction of the "middle point" z_c. This is a key idea in the FMM.

The integral in Eq. (173) is now evaluated as follows:

$$\int_{\partial B_c} G(z_0, z)q(z)dS(z) = \frac{1}{2\pi}\int_{\partial B_c}\left[\sum_{k=0}^{\infty} O_k(z - z_c)I_k(z - z_c)\right] q(z)dS(z), \tag{181}$$

that is, the *multipole expansion*:

$$\int_{\partial B_c} G(z_0, z)q(z)dS(z) = \frac{1}{2\pi}\sum_{k=0}^{\infty} O_k(z_0 - z_c)M_k(z_c), \tag{182}$$

where

$$M_k(z_c) = \int_{\partial B_c} I_k(z - z_c)q(z)dS(z), \quad k = 1, 2, \ldots \tag{183}$$

are called *moments* about z_c, which are independent of the collocation point z_0 and only need to be computed once. After these moments are obtained, the G kernel integral can be evaluated readily using Eq. (182) for any collocation point z_0 away from ∂B_c (which will be within a *cell* centered at z_c). The moments can be evaluated analytically using complex notation on constant elements [Liu (2009)].

Error estimate for the multipole expansion. Errors in the multipole expansion are controlled by the number of terms used in the expansion in (176). An error bound can be derived readily for this multipole expansion [Greengard (1988)]. If one applies a multipole expansion with p terms in Eq. (182), one has the following error bound:

$$\begin{aligned}
E_M^p &= \left|\int_{\partial B_c} G(z_0, z)q(z)dS(z) - \frac{1}{2\pi}\sum_{k=0}^{p} O_k(z_0 - z_c)M_k(z_c)\right| \\
&= \frac{1}{2\pi}\left|\sum_{k=p+1}^{\infty} O_k(z - z_c)M_k(z_c)\right| \leq \frac{1}{2\pi}\sum_{k=p+1}^{\infty} |O_k(z - z_c)||M_k(z_c)| \\
&= \frac{1}{2\pi}\sum_{k=p+1}^{\infty} |O_k(z - z_c)|\left|\int_{\partial B_c} I_k(z - z_c)q(z)dS(z)\right| \\
&\leq \frac{1}{2\pi}\sum_{k=p+1}^{\infty} |O_k(z - z_c)|\int_{\partial B_c} |I_k(z - z_c)||q(z)|dS(z) \\
&\leq \frac{A}{2\pi}\sum_{k=p+1}^{\infty} |O_k(z - z_c)|\frac{R^k}{k!}
\end{aligned}$$

$$= \frac{A}{2\pi} \sum_{k=p+1}^{\infty} \frac{(k-1)! R^k}{|z_0 - z_c|^k k!} \leq \frac{A}{2\pi} \sum_{k=p+1}^{\infty} \frac{R^k}{|z_0 - z_c|^k}$$

$$= \frac{A}{2\pi} \frac{R^{p+1}}{|z_0 - z_c|^{p+1}} \frac{1}{(1 - R/|z_0 - z_c|)}, \tag{184}$$

in which R is the radius of a region centered at z_c such that:

$$|z - z_c| < R; \quad \text{and} \quad A \equiv \int_{\partial B_c} |q(z)| dS(z). \tag{185}$$

With $\rho = |z - z_c|/R$, the above estimate of the error bound can be written as:

$$E_M^p \leq \frac{A}{2\pi} \frac{1}{(\rho - 1)} \left[\frac{1}{\rho}\right]^p. \tag{186}$$

It is noticed from Eq. (186) that the larger the value of ρ, the smaller the value of this estimate of the error bound. If $\rho \geq 2$, that is, when $|z_0 - z_c| \geq 2R$, one has the following estimate:

$$E_M^p \leq \frac{A}{2\pi} \left[\frac{1}{2}\right]^p. \tag{187}$$

An error bound can be used to estimate the number p of the expansion terms needed for a given accuracy.

Moment-to-moment translation (M2M). If the expansion point z_c is moved to a new location $z_{c'}$ (Fig. 28), one can apply a translation to obtain the moment at the new location without re-computing the moment by using Eq. (183). This translation is obtained by considering the following relationship between the moments:

$$M_k(z_{c'}) = \int_{\partial B_c} I_k(z - z_{c'}) q(z) dS(z)$$

$$= \int_{\partial B_c} I_k[(z - z_c) + (z_c - z_{c'})] q(z) dS(z). \tag{188}$$

Applying the binomial formula, one gets:

$$M_k(z_{c'}) = \sum_{\ell=0}^{k} I_{k-\ell}(z_c - z_{c'}) M_\ell(z_c). \tag{189}$$

This is the *M2M translation* for the moments when z_c is moved to $z_{c'}$. Note that there are only a finite number of terms needed in this translation, that is, no additional truncation error is introduced in the M2M translations.

Local expansion and moment-to-local translation (M2L). Next, another expansion is introduced, the so called local expansion about the source point z_0. Suppose z_L is a point close to the source point z_0 (Fig. 28), that is,

$|z_0 - z_L| \ll |z_L - z_c|$. From the multipole expansion in Eq. (182), one has:

$$\int_{\partial B_c} G(z_0, z) q(z) dS(z) = \frac{1}{2\pi} \sum_{k=0}^{\infty} O_k(z_0 - z_c) M_k(z_c)$$

$$= \frac{1}{2\pi} \sum_{k=0}^{\infty} O_k[(z_L - z_c) + (z_0 - z_L)] M_k(z_c)]. \quad (190)$$

Expanding this expression about the point $z_0 = z_L$, one obtains the following *local expansion*:

$$\int_{\partial B_c} G(z_0, z) q(z) dS(z) = \frac{1}{2\pi} \sum_{\ell=0}^{\infty} L_\ell(z_L) I_\ell(z_0 - z_L), \quad (191)$$

where the local expansion coefficients $L_\ell(z_L)$ are given by the following $M2L$ *translation*:

$$L_\ell(z_L) = (-1)^\ell \sum_{k=0}^{\infty} O_{\ell+k}(z_L - z_c) M_k(z_c). \quad (192)$$

Similar to the multipole expansion, an estimate of the error bound for a local expansion with p terms from Eq. (191) can be found as follows [Greengard (1988)]:

$$E_L^p = \left| \int_{\partial B_c} G(z_0, z) q(z) dS(z) - \frac{1}{2\pi} \sum_{\ell=0}^{p} L_\ell(z_L) I_\ell(z_0 - z_L) \right|$$

$$= \frac{1}{2\pi} \left| \sum_{\ell=p+1}^{\infty} L_\ell(z_L) I_\ell(z_0 - z_L) \right| \leq \frac{A[4e(p+\rho)(\rho+1) + \rho^2]}{2\pi\rho(\rho-1)} \left[\frac{1}{\rho}\right]^{p+1} \quad (193)$$

for any $p \geq \max\{2, 2\rho/(\rho-1)\}$, where e is the base of the natural logarithm, and A and ρ are as defined for Eq. (186).

Local-to-local translation (L2L). If the point for local expansion is moved from z_L to $z_{L'}$ (Fig. 28), one has the following expression using a local expansion with p terms from Eq. (191):

$$\int_{\partial B_c} G(z_0, z) q(z) dS(z) \approx \frac{1}{2\pi} \sum_{\ell=0}^{p} L_\ell(z_L) I_\ell(z_0 - z_L)$$

$$= \frac{1}{2\pi} \sum_{\ell=0}^{p} L_\ell(z_L) I_\ell[(z_0 - z_{L'}) + (z_{L'} - z_L)] \quad (194)$$

Applying the binomial formula and the relation:

$$\sum_{\ell=0}^{p} \sum_{m=0}^{\ell} = \sum_{m=0}^{p} \sum_{\ell=m}^{p}$$

one obtains:

$$\int_{\partial B_c} G(z_0, z)q(z)dS(z) \approx \frac{1}{2\pi}\sum_{\ell=0}^{p} L_\ell(z_{L'})I_\ell(z_0 - z_{L'}), \tag{195}$$

where the new coefficients are given by the following *L2L translation*:

$$L_\ell(z_{L'}) = \sum_{m=\ell}^{p} I_{m-\ell}(z_{L'} - z_L)L_m(z_L). \tag{196}$$

Note again that L2L translations involve only finite sums and do not introduce any new source of errors once the number of the local expansion terms p is fixed.

The multipole expansion and related translations for the F kernel integral and integrals in the HBIE can be derived similarly for 2D potential problems [Liu (2009)].

Fast multipole BEM algorithms. A detailed description of the fast multiple BEM algorithm can be found in the literature [Liu (2009); Nishimura (2002); Liu and Nishimura (2006)]. The main ingredients are summarized below (see Fig. 29). An iterative solver, such as GMRES [Saad and Schultz (1986)], will need to be used to solve the system of equations $\mathbf{A}\boldsymbol{\lambda} = \mathbf{b}$ with the fast multipole BEM. Each equation in this system of equations represents the sum of the integrals on all the elements when the source point is placed at one node. The FMM is used to evaluate the integrals on those elements that are far away from the source point, while the conventional approach is applied to evaluate the integrals on the remaining elements

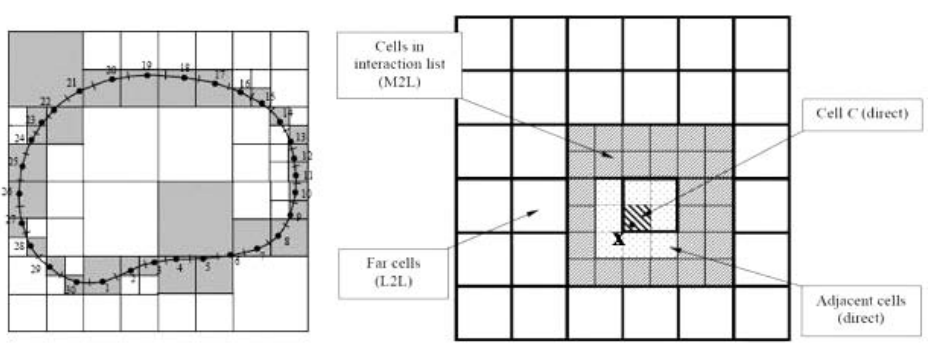

Apply an iterative solver (GMRES) to solve the BEM system of equations **Ax** = **b**:
Step 1. ***Discretization***. Discretize the boundary as in the conventional BEM.
Step 2. Determine a ***tree structure*** for the boundary elements.
Step 3. ***Upward pass***. Compute the moments on all cells, tracing the tree structure upward (M2M).
Step 4. ***Downward pass***. Compute the local expansion (coefficients), tracing the tree structure downward (using M2L for cells in the *interaction list* and L2L for all *far cells*).
Step 5. ***Evaluation of integrals*** for collocation at **x**. Direct method for *adjacent cells* and local expansion (L2L) for all other cells.
Step 6. ***Iterations of the solution***. Update the matrix-vector multiplication in **Ax** = **b**, and iterate.

Fig. 29. FMM-BEM algorithm.

that are close to the source point. The algorithms in the fast multipole BEM can be summarized as follows:

First, discretize the boundary of the problem domain using boundary elements as usual (as in the conventional BEM). Second, regroup the elements using cells (a square in 2D or a box in 3D) that have a multilevel, hierarchical (upside-down) tree structure (Fig. 27(b)) with the smallest cells (leaves) containing a limited number of elements. Compute the moments on each leaf in the multipole expansions (using, for example, Eq. (183) for 2D potential problems). Third, compute the moments on larger cells using the M2M translations, climbing the tree upward (upward pass). Fourth, compute the local expansion coefficients using M2L translations for larger cells and then for smaller cells using L2L translations, all the way down to a leaf (downward pass). Finally, evaluate the integral for each node (source point) using the local expansion for far-away elements and direct integration for nearby elements. This completes one matrix-vector multiplication $\mathbf{A}\boldsymbol{\lambda}$ for the iterative solver. The procedure is repeated until the solution for the system $\mathbf{A}\boldsymbol{\lambda} = \mathbf{b}$ converges within a given tolerance.

4.3.3. *Fast multipole formulation for 3D problems*

Again, the potential theory problem is used as an example to show the main results in the fast multipole BEM for 3D problems. First, it is noted that the kernel $G(\mathbf{x}, \mathbf{y})$ for 3D potential problems can be expanded as follows [Liu (2009); Nishimura (2002); Shen and Liu (2007a)]:

$$\begin{aligned} G(\mathbf{x}, \mathbf{y}) &= \frac{1}{4\pi r(\mathbf{x}, \mathbf{y})} \\ &= \frac{1}{4\pi} \sum_{n=0}^{\infty} \sum_{m=-n}^{n} \overline{S_{n,m}}(\mathbf{x} - \mathbf{y}_c) R_{n,m}(\mathbf{y} - \mathbf{y}_c), \quad |\mathbf{y} - \mathbf{y}_c| < |\mathbf{x} - \mathbf{y}_c|, \end{aligned} \tag{197}$$

where $\mathbf{y}_c$ is the expansion center close to the field point $\mathbf{y}$, and $\bar{()}$ indicates the complex conjugate. The two functions $R_{n,m}$ and $S_{n,m}$ are called solid harmonic functions. These are:

$$R_{n,m}(\mathbf{x}) = \frac{1}{(n+m)!} P_n^m(\cos(\theta)) e^{im\phi} \rho^n, \tag{198}$$

$$S_{n,m}(\mathbf{x}) = (n-m)! P_n^m(\cos(\theta)) e^{im\phi} \frac{1}{\rho^{n+1}}, \tag{199}$$

where ρ, θ, ϕ are coordinates of $\mathbf{x}$ in a spherical coordinate system, and P_n^m is the associated Legendre function.

Applying expansions in Eq. (197), one can evaluate the G integral in the BIE on ∂B_c (a subset of ∂B that is away from source point $\mathbf{x}$) as follows:

$$\begin{aligned} &\int_{\partial B_c} G(\mathbf{x}, \mathbf{y}) q(\mathbf{y}) dS(\mathbf{y}) \\ &\quad = \frac{1}{4\pi} \sum_{n=0}^{\infty} \sum_{m=-n}^{n} \overline{S_{n,m}}(\mathbf{x} - \mathbf{y}_c) M_{n,m}(\mathbf{y}_c), \quad |\mathbf{y} - \mathbf{y}_c| < |\mathbf{x} - \mathbf{y}_c|, \end{aligned} \tag{200}$$

where $M_{n,m}$ are the *multipole moments* centered at $\mathbf{y}_c$ and defined as:

$$M_{n,m}(\mathbf{y}_c) = \int_{\partial B_c} R_{n,m}(\mathbf{y} - \mathbf{y}_c) q(\mathbf{y}) dS(\mathbf{y}). \tag{201}$$

When the multipole expansion center is moved from $\mathbf{y}_c$ to $\mathbf{y}_{c'}$, one applies the following *M2M translation*:

$$\begin{aligned} M_{n,m}(\mathbf{y}_{c'}) &= \int_{\partial B_c} R_{n,m}(\mathbf{y} - \mathbf{y}_{c'}) q(\mathbf{y}) dS(\mathbf{y}) \\ &= \sum_{n'=0}^{n} \sum_{m'=-n'}^{n'} R_{n',m'}(\mathbf{y}_c - \mathbf{y}_{c'}) M_{n-n',m-m'}(\mathbf{y}_c). \end{aligned} \tag{202}$$

The *local expansion* for the G kernel integral on ∂B_c is given as follows:

$$\int_{\partial B_c} G(\mathbf{x}, \mathbf{y}) q(\mathbf{y}) dS(\mathbf{y}) = \frac{1}{4\pi} \sum_{n=0}^{\infty} \sum_{m=-n}^{n} R_{n,m}(\mathbf{x} - \mathbf{x}_L) L_{n,m}(\mathbf{x}_L), \tag{203}$$

where the local expansion coefficients $L_{n,m}(\mathbf{x}_L)$ are given by the following *M2L translation*:

$$\begin{aligned} L_{n,m}(\mathbf{x}_L) = (-1)^n &\sum_{n'=0}^{\infty} \sum_{m'=-n'}^{n'} \overline{S_{n+n',m+m'}} \\ &\times (\mathbf{x}_L - \mathbf{y}_c) M_{n',m'}(\mathbf{y}_c), \quad |\mathbf{x} - \mathbf{x}_L| < |\mathbf{y}_c - \mathbf{x}_L|, \end{aligned} \tag{204}$$

in which $\mathbf{x}_L$ is the local expansion center.

The local expansion center can be shifted from $\mathbf{x}_L$ to $\mathbf{x}_{L'}$ using the following *L2L translation*:

$$L_{n,m}(\mathbf{x}_{L'}) = \sum_{n'=n}^{\infty} \sum_{m'=-n'}^{n'} R_{n'-n,m'-m}(\mathbf{x}_{L'} - \mathbf{x}_L) L_{n',m'}(\mathbf{x}_L). \tag{205}$$

The multipole expansion and related translations for the F kernel integral and integrals in the HBIE can be derived similarly for 3D potential problems [Liu (2009)].

Detailed discussions on the fast multipole BEM for potential, elasticity, Stokes flow, and acoustics, in both 2D and 3D, can be found in the textbook [Liu (2009)]. Sample computer codes are also available in this textbook for readers to develop their own fast multipole BEM codes for solving other problems.

4.3.4. *Numerical examples*

The computational efficiencies of the fast multipole BEM as compared with the conventional BEM are demonstrated with a few examples in this section.

A comparison of the conventional BEM and fast multipole BEM. A 2D potential problem in a cylindrical region is first used as an example to compare the computational efficiency and accuracy of the conventional BEM and the fast

multipole BEM. The cylindrical region has an inner radius of $a = 1$ and outer radius of $b = 2$. On the inner boundary the potential ϕ is given and on the outer boundary the normal derivative q is given. Both boundaries are discretized using the same number of elements. For the fast multipole BEM, the tolerance for convergence of the solution is set to 10^{-8}.

Figure 30 shows the computed results of the potential on the outer boundary and normal derivative of the potential on the inner boundary with the two BEM approaches. Both the conventional BEM and the fast multipole BEM converge quickly for this problem and their accuracies are equivalent. The CPU times used for both approaches are plotted in Fig. 31, which shows significant advantage of the fast multipole BEM compared with the conventional BEM. For example, for the largest model with 9,600 elements, the fast multipole BEM used less than 17 s, while the conventional BEM used about 7,500 s of CPU time on a laptop PC with a Pentium IV 2.4 GHz CPU.

A fuel cell model. The next example is that of a solid oxide fuel cell with nine cells used for thermal analysis (Fig. 32). There are 1,000 small holes on the inner and outer surfaces of each cylindrical cell, with a total of 9,000 holes for the entire stack. Due to the extremely complicated geometry, the FEM can only model one cell on a PC with 1 GB RAM. For the fast multipole BEM, however, multi-cell models can be handled readily, such as the 9-cell stack modeled successfully with 530,230 elements and solved on a desktop PC with 1 GB RAM.

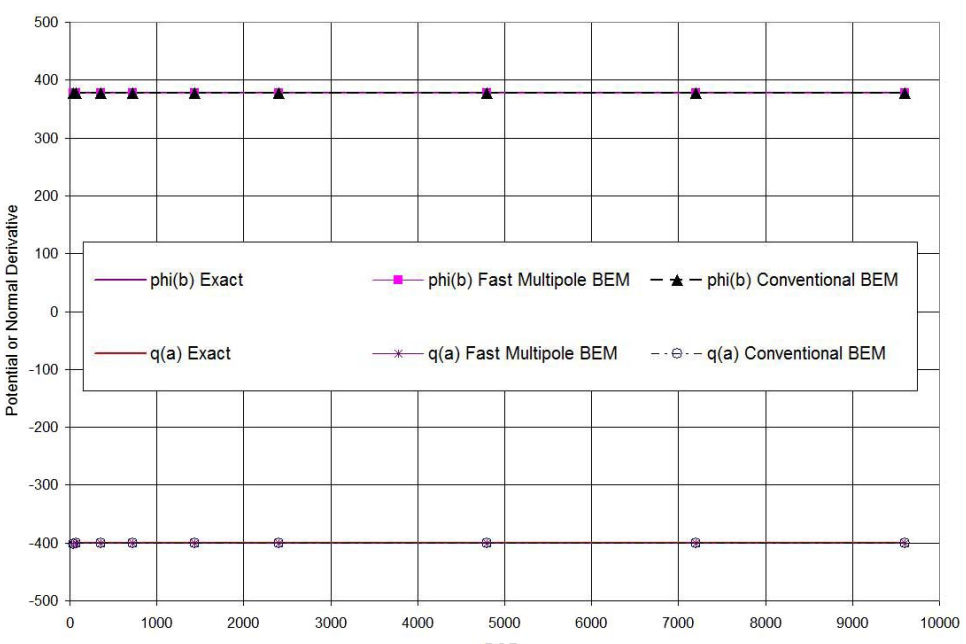

Fig. 30. Computed results from the conventional BEM and fast multipole BEM.

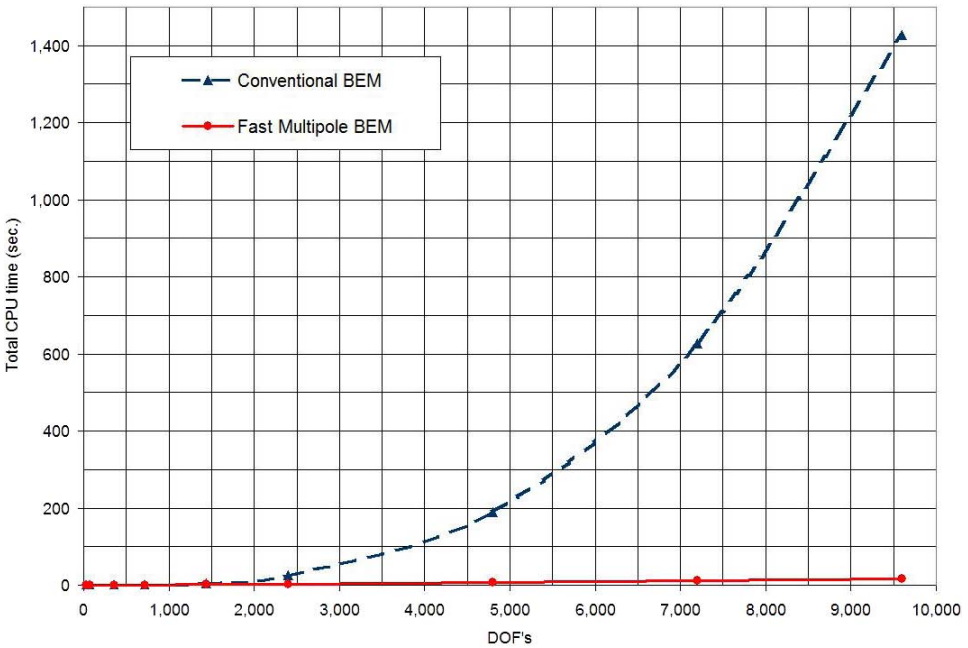

Fig. 31. (Color online) CPU time used by conventional BEM and fast multipole BEM (from Liu [2009]).

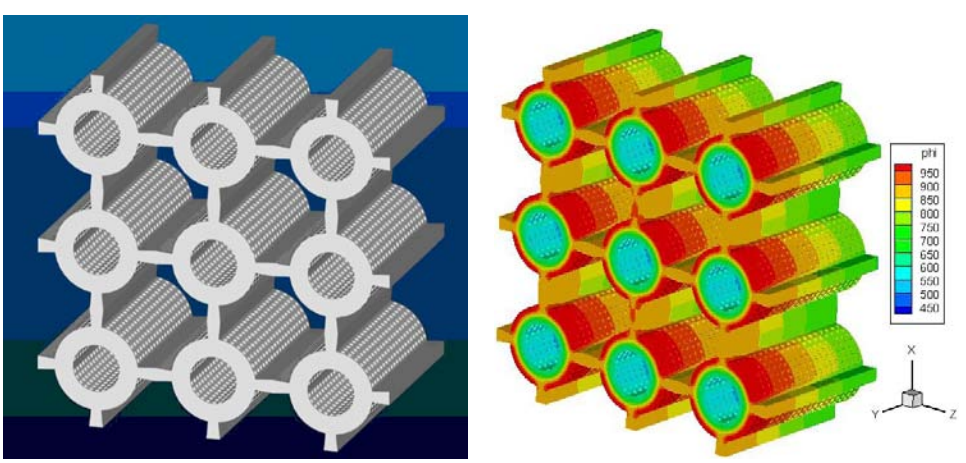

(a) (b)

Fig. 32. (Color online) A fuel cell model for thermal analysis with 530,230 DOF.

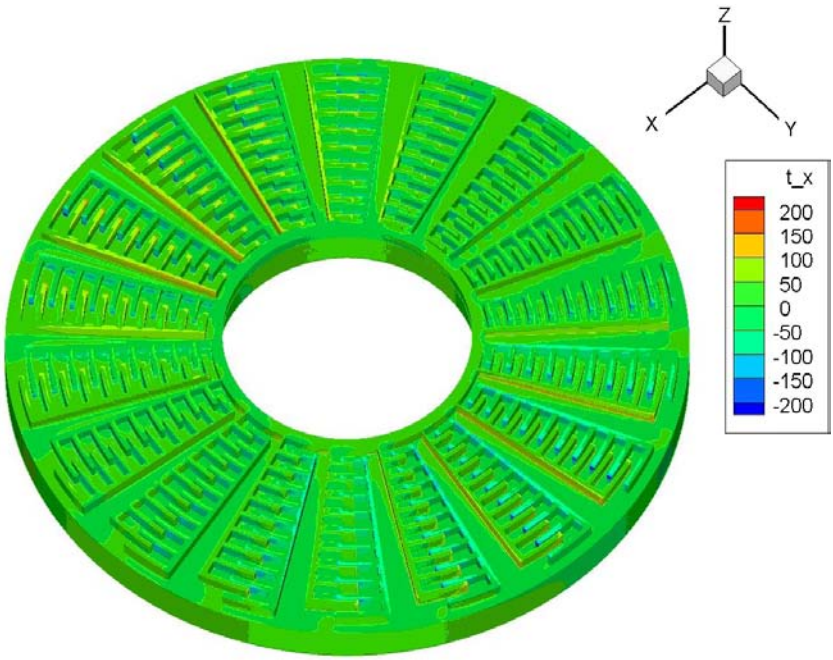

Fig. 33. (Color online) A MEMS torsional accelerometer model using the BEM with 1,087,986 DOF — drag force in the x direction.

A MEMS model. Figures 33 and 34 show a model for a MEMS torsional accelerometer with a total of 1,087,986 DOF. This is an exterior Stokes flow problem used to study the drag forces in the device. For the boundary conditions, the substrate is fixed and the rotor (moving part) has an angular velocity applied to it. A 3D Stokes flow fast multipole BEM code is used to calculate the drag forces on this MEMS device. Figure 33 is a plot of the drag force in the x direction and Fig. 34 of the drag force in the z direction. This large BEM model with 1,087,986 DOF was solved on a desktop PC.

Acoustic waves scattered from a human head. The last example is one in acoustic wave analysis using the fast multipole BEM. Figure 35 shows a human head discretized (meshed) using 87,340 constant boundary elements (Fig. 35(a)). The sound pressure field (Fig. 35(b)) on the model surface was computed using the fast multipole BEM solver with a plane incident wave coming in the x direction at 11 kHz. The problem was solved in 20 min on a desktop PC. It is interesting to notice that both ears on the illuminated side (left ear) and the shadow side (right ear) register higher sound pressures, besides the area between the two lips. The same phenomena were observed in models at other frequencies and with waves coming in other directions.

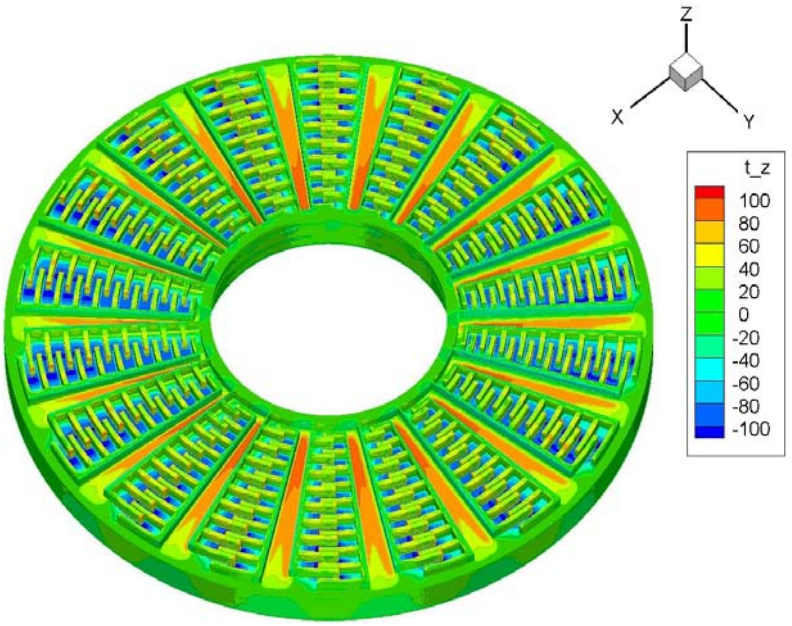

Fig. 34. (Color online) A MEMS torsional accelerometer model using the BEM with 1,087,986 DOF — drag force in the z direction.

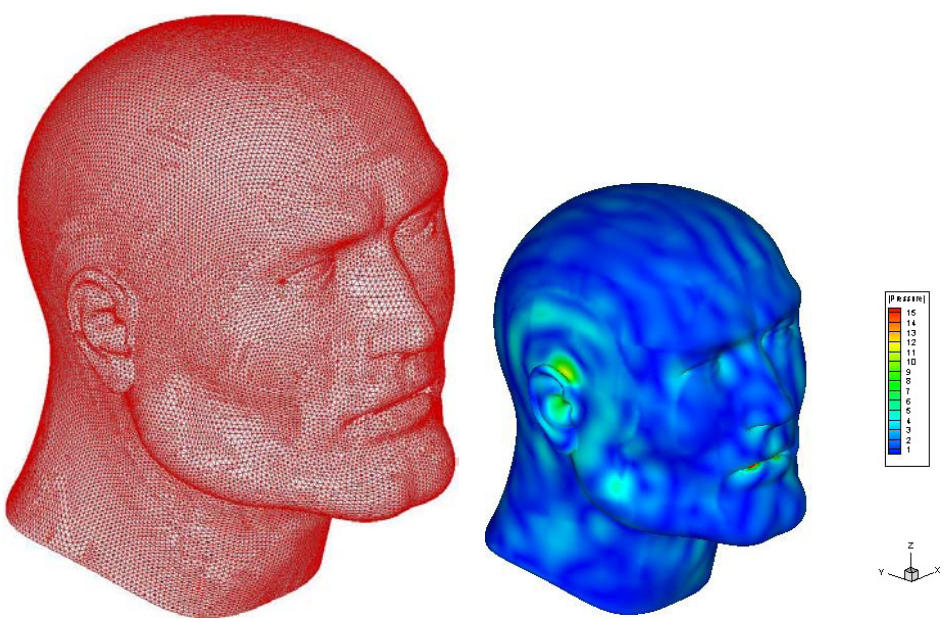

(a) (b)

Fig. 35. (Color online) A human head model for acoustic wave analysis with 87,340 DOF (from Liu [2009]).

More examples demonstrating the accuracy, efficiency and applications of the fast multipole BEM can be found in the published literature. Examples are [Liu and Nishimura (2006); Shen and Liu (2007a); Liu (2006); Liu and Shen (2007)] for potential problems, [Liu *et al.* (2005a); Liu (2005); Liu *et al.* (2005b); Liu (2008a)] for elasticity problems, [Liu (2008b)] for 2D Stokes problems, and [Liu (2009); Shen and Liu (2007b); Bapat *et al.* (2009); Liu *et al.* (2009)] for acoustic wave problems.

Acknowledgments

The first author (SM) acknowledges NSF support to Cornell University through the grant CMS-0508466. He also acknowledges the research contributions of his former students Zhongping Bao, Mandar Chati, Glaucio Paulino and Srinivas Telukunta, former Cornell graduate student Xiaolan Shi, and his wife Yu Mukherjee.

The second author (YJL) would like to acknowledge NSF support through the grant CMS-0508232. He also thanks Dr. Milind Bapat and Mr. Bo Bi for their work used in the last two examples.

Both the authors gratefully acknowledge the careful reading of and very useful feed-back on this work by Professor Romesh Batra at Virginia Tech.

References

Aluru, N. R. and Li, G. [2001] "Finite cloud method: A true meshless technique based on a fixed reproducing kernel approximation," *Int. J. Numer Meth. Eng.* **50**, 2373–2410.

Aluru, N. R. and White, J. [1997] "An efficient numerical technique for electromechanical simulation of complicated microelectromechancial structures," *Sensors Actuators A* **58**, 1–11.

Atluri, S. N. and Shen, S. [2002] *The Meshless Local Petrov-Galerkin* (*MLPG*) *Method* (Tech Science Press, Encino, CA).

Banerjee, P. K. [1994] *Boundary Element Methods in Engineering* (McGraw-Hill Europe, Maidenhead, Berkshire, UK).

Bao, Z. and Mukherjee, S. [2004] "Electrostatic BEM for MEMS with thin conducting plates and shells," *Eng. Anal. Boundary Elements* **28**, 1427–1435.

Bao, Z. and Mukherjee, S. [2005] "Electrostatic BEM for MEMS with thin beams," *Comm. Numer Meth. Eng.* **21**, 297–312.

Bapat, M. S., Shen, L. and Liu, Y. J. [2009] "Adaptive fast multipole boundary element method for three-dimensional half-space acoustic wave problems," *Eng. Anal. Bound. Elem.* **33**, 1113–1123.

Batra, R. C. and Porfiri, M. [2008] "Analysis of rubber-like materials using meshless local Petrov-Galerkin (MLPG) method," *Comm. Numer Meth. Eng.* **24**, 1781–1804.

Batra, R. C. and Spinello, D. [2009] "Analysis of adiabatic shear bands in heat-conducting elastothermoviscoplastic materials by the meshless local Bubnov-Galerkin method," *Comm. Numer Meth. Eng.* **25**, 1019–1040.

Becker, A. A. [1992] *The Boundary Element Method in Engineering* (McGraw-Hill, NY).

Belytschko, T., Lu, Y. Y. and Gu, L. [1994] "Element-free Galerkin methods," *Int. J. Numer Meth. Eng.* **37**, 229–256.

Belytschko, T., Krongauz, Y., Organ, D., Fleming, M. and Krysl, P. [1996] "Meshless methods: An overview and recent developments," *Comput. Meth. Appl. Mech. Eng.* **139**, 3–47.

Belytschko, T., Liu, W. K. and Moran, B. [2000] *Nonlinear Finite Elements for Continua and Structures* (Wiley, Chichester, UK).

Bobaru, F. and Mukherjee, S. [2001] "Shape sensitivity analysis and shape optimization in planar elasticity using the element-free Galerkin method," *Comput. Meth. Appl. Mech. Eng.* **190**, 4319–4337.

Bobaru, F. and Mukherjee, S. [2002] "Meshless approach to shape optimization of linear thermoelastic solids," *Int. J. Numer Meth. Eng.* **53**, 765–796.

Bonnet, A. [1999] *Boundary Element Equation Methods for Solids and Fluids* (Wiley, Chichester, UK).

Brebbia, C. A., Telles, J. C. F. and Wrobel, L. C. [1984] *Boundary Element Techniques*: *Theory and Applications in Engineering* (Springer, Berlin, Heidelberg, Germany).

Burton, A. J. and Miller, G. F. [1971] "The application of integral equation methods to the numerical solution of some exterior boundary-value problems," *Proc. Royal Soc. London A* **323**, 201–210.

Chandra, A. and Mukherjee, S. [1997] *Boundary Element Methods in Manufacturing* (Oxford University Press, NY).

Chati, M. K. and Mukherjee, S. [2000] "The boundary node method for three-dimensional problems in potential theory," *Int. J. Numer Meth. Eng.* **47**, 1523–1547.

Chati, M. K., Mukherjee, S. and Mukherjee, Y. X. [1999] "The boundary node method for three-dimensional linear elasticity," *Int. J. Numer Meth. Eng.* **46**, 1163–1184.

Chati, M. K., Paulino, G. H. and Mukherjee, S. [2001a] "The meshless standard and hypersingular boundary node methods-applications to error estimation and adaptivity in three-dimensional problems," *Int. J. Numer Meth. Eng.* **50**, 2233–2269.

Chati, M. K., Mukherjee, S. and Paulino, G. H. [2001b] "The meshless hypersingular boundary node method for three-dimensional potential theory and linear elasticity problems," *Eng. Anal. Bound. Elem.* **25**, 639–653.

Chen, H. and Mukherjee, S. [2006] "Charge distribution on thin conducting nanotubes — Reduced 3d model," *Int. J. Numer Meth. Eng.* **68**, 503–524.

Chen, H., Mukherjee, S. and Aluru, N. [2008] "Charge distribution on thin semiconducting silicon nanowire," *Comput. Meth. Appl. Mech. Eng.* **197**, 3366–3377.

Chen, W. and Tanaka, M. [2002] "A meshless, integration-free, boundary-only RBF technique," *Comput. Math. Appl.* **43**, 379–391.

Chuyan, S.-W., Liao, Y.-S. and Chen, J.-T. [2005] "Computational study of the effect of finger width and aspect ratios for the electrostatic levitating force of MEMS comb drive," *J. Microelectromech Syst.* **14**, 305–312.

Cruse, T. A. [1969] "Numerical solutions in three-dimensional elastostatics," *Int. J. Solids Struct.* **5**, 1259–1274.

Cruse, T. A. and Richardson, J. D. [1996] "Non-singular somigliana stress identities in elasticity," *Int. J. Numer Meth. Eng.* **39**, 3273–3304.

Das, K. and Batra, R. C. [2009a] "Pull-in and snap-through instabilities in transient deformations of microelectromechanical systems," *J. Micromech. Microeng.* **19**, 035008, 1–19.

Das, K. and Batra, R. C. [2009b] "Symmetry breaking, snap-through, and pull-in instabilities under dynamic loading of microelectromechanical shallow arch," *Smart Mat. Struct.* **18**, 115008, 1–15.

De, S. and Bathe, K. J. [2001a] "The method of finite spheres with improved numerical integration," *Comput. Struct.* **79**, 2183–2196.

De, S. and Bathe, K. J. [2001b] "Displacement/pressure mixed interpolation in the method of finite spheres," *Int. J. Numer Meth. Eng.* **51**, 275–292.

De, S. K. and Aluru, N. R. [2004] "Full-Lagrangian schemes for dynamic analysis of electrostatic MEMS," *J. Microelecromech. Syst.* **13**, 737–758.

Frangi, A. and diGioa, A. [2005] "Multipole BEM for evaluating damping forces on MEMS," *Comput. Mech.* **37**, 24–31.

Fu, Y., Klimkowski, K. J., Rodin, G. J., Berger, E., Browne, J. C., Singer, J. K., Geijn, R. A. V. D. and Vemaganti, K. S. [1998] "A fast solution method for three-dimensional many-particle problems of linear elasticity," *Int. J. Numer Meth. Eng.* **42**, 1215–1229.

Ghosh, N. and Mukherjee, S. [1987] "A new boundary element method formulation for three dimensional problems in linear elasticity," *Acta Mech.* **67**, 107–119.

Gilbert, J. R., Legtenberg, R. and Senturia, S. D. [1995] "3D coupled electromechanics for MEMS: Applications of cosolve-em," *Proc. IEEE MEMS*, 122–127.

Gilhooley, D. F., Xiao, J. R., Batra, R. C., McCarthy, M. A. and Gillespie, J. W. Jr. [2008] "Two-dimensional stress analysis of functionally graded solids using the MLPG method with radial basis functions," *Comput. Mat. Sc.* **41**, 467–481.

Gomez, J. E. and Power, H. [1997] "A multipole direct and indirect BEM for 2D cavity flow at low reynolds number," *Eng. Anal. Bound. Elem.* **19**, 17–31.

Gowrishankar, R. and Mukherjee, S. [2002] "The "pure" boundary node method for potential theory," *Comm. Numer Meth. Eng.* **18**, 411–427.

Greengard, L. F. [1988] *The Rapid Evaluation of Potential Fields in Particle Systems* (The MIT Press, Cambridge, MA).

Greengard, L. F. and Rokhlin, V. [1987] "A fast algorithm for particle simulations," *J. Comput. Physics* **73**, 325–348.

Harrington, R. F. [1993] *Field Computation by Moment Methods* (IEEE, Piscataway, New Jersey).

Hayt, W. H. and Buck, J. A. [2001] *Engineering Electromagnetics* (McGraw Hill, London).

Hughes, T. J. R. [2000] *The Finite Element Method*: *Linear Static and Dynamic Finite Element Analysis* (Dover, Mineola, NY).

Kaplan, W. [1984] *Advanced Calculus*, 3rd edition (Addison-Wesley, Reading, MA).

Kitipornchai, S., Liew, K. M. and Cheng, Y. [2005] "A boundary element-free method (BEFM) for three-dimensional elasticity problems," *Comput. Mech.* **36**, 13–20.

Ko, S. C., Kim, Y. C., Lee, S. S., Choi, S. S. and Kim, S. R. [2003] "Micromachined piezoelectric membrane acoustic device," *Sensors Actuarors A* **103**, 130–134.

Kothnur, V., Mukherjee, S. and Mukherjee, Y. X. [1999] "Two-dimensional linear elasticity by the boundary node method," *Int. J. Solids Struct.* **36**, 1129–1147.

Kress, R. [1985] "Minimizing the condition number of boundary integral operators in acoustic and electromagnetic scattering," *Quart. J. Mech. Appl. Math.* **38**, 323–341.

Krishnasamy, G., Rizzo, F. J. and Liu Y. J. [1994] "Boundary integral equations for thin bodies," *Int. J. Numer Meth. Eng.* **37**, 107–121.

Lancaster, P. and Salkauskas, K. [1981] "Surfaces generated by moving least squares methods," *Math. Comput.* **37**, 141–158.

Li, G. and Aluru, N. R. [2002] "Boundary cloud method: A combined scattered point/boundary integral approach for boundary-only analysis," *Comput. Meth. Appl. Mech. Eng.* **191**, 2337–2370.

Li, G. and Aluru, N. R. [2003] "A boundary cloud method with a cloud-by-cloud polynomial basis," *Eng. Anal. Bound. Elem.* **27**, 57–71.

Liu, G. R. [2002] *Mesh-free Methods*: *Moving Beyond the Finite Element Method* (CRC Press, Boca Raton, FL).

Liu, W. K., Chen, Y., Uras, R. A. and Chang, C. T. [1996a] "Generalized multiple scale reproducing kernel particle methods," *Comput. Meth. Appl. Mech. Eng.* **139**, 91–157.

Liu, W. K., Chen, Y., Jun, S., Belytschko, T., Pan, C., Uras, R. A. and Chang, C. T. [1996b] "Overview and applications of the reproducing kernel particle methods," *Archives Comput. Meth. Eng.* **3**, 3–80.

Liu, Y. J. [1998] "Analysis of shell like structures by the boundary element method based on 3D elasticity: Formulation and verification," *Int. J. Numer Meth. Eng.* **41**, 541–558.

Liu, Y. J. [2000] "On the simple-solution method and non-singular nature of the BIE/BEM — A review and some new results," *Eng. Anal. Bound. Elem.* **24**, 787–793.

Liu, Y. J. [2005] "A new fast multipole boundary element method for solving large-scale two-dimensional elastostatic problems," *Int. J. Numer Meth. Eng.* **65**, 863–881.

Liu, Y. J. [2006] "Dual BIE approaches for modeling electrostatic MEMS problems with thin beams and accelerated by the fast multipole method," *Eng. Anal. Bound. Elem.* **30**, 940–948.

Liu, Y. J. [2008a] "A fast multipole boundary element method for 2D multi-domain elastostatic problems based on a dual BIE formulation," *Comput. Mech.* **42**, 761–773.

Liu, Y. J. [2008b] "A new fast multipole boundary element method for solving 2D stokes flow problems based on a dual BIE formulation," *Eng. Anal. Bound. Elem.* **32**, 139–151.

Liu, Y. J. [2009] *Fast Multipole Boundary Element Method — Theory and Applications in Engineering* (Cambridge University Press, Cambridge, UK).

Liu, Y. J. and Chen, S. H. [1999] "A new form of the hypersingular boundary integral equation for 3D acoustics and its implementation with C^0 boundary elements," *Comput. Meth. Appl. Mech. Eng.* **173**, 375–386.

Liu, Y. J. and Nishimura, N. [2006] "The fast multipole boundary element method for potential problems: A tutorial," *Eng. Anal. Bound. Elem.* **30**, 371–381.

Liu, Y. J. and Rizzo, F. J. [1992] "A weakly-singular form of the hypersingular boundary integral equation applied to 3D acoustic wave problems," *Comput. Meth. Appl. Mech. Eng.* **96**, 271–287.

Liu, Y. J. and Rizzo, F. J. [1997] "Scattering of elastic waves from thin shapes in three dimensions using the composite boundary integral equation formulation," *J. Acoust. Soc. America* **102**(2, Part 1), 926–932.

Liu, Y. J. and Rudolphi, T. J. [1991] "Some identities for fundamental solutions and their applications to weakly-singular boundary element formulations," *Eng. Anal. Bound. Elem.* **8**, 301–311.

Liu, Y. J. and Rudolphi, T. J. [1999] "New identities for fundamental solutions and their applications to non-singular boundary element formulations," *Comput. Mech.* **24**, 286–292.

Liu, Y. J. and Shen, L. [2007] "A dual bie approach for large-scale modelling of 3D electrostatic problems with the fast multipole boundary element method," *Int. J. Numer Meth. Eng.* **71**, 837–855.

Liu, Y. J., Nishimura, N., Otani, Y., Takahashi, T., Chen, X. L. and Munakata, H. [2005a] "A fast boundary element method for the analysis of fiber-reinforced composites based on a rigid-inclusion model," *ASME J. Appl. Mech.* **72**, 115–128.

Liu, Y. J., Nishimura, N. and Otani, Y. [2005b] "Large-scale modeling of carbon-nanotube composites by the boundary element method based on a rigid-inclusion model," *Comput. Mat. Sci.* **34**, 173–187.

Liu, Y. J., Shen, L. and Bapat, M. S. [2009] "Development of the fast multipole boundary element method for acoustic wave problems," in *Recent Advances in the Boundary Element Methods*, eds. G.M.a.D. Polyzos (Springer-Verlag, Berlin), pp. 287–303.

Lucy, L. B. [1977] "A numerical approach to the testing of the fusion hypothesis," *Astro. J.* **82**, 1013–1024.

Lutz, E. D., Ingraffea, A. R. and Gray, L. J. [1992] "Use of 'simple solutions' for boundary integral equation methods in elasticity and fracture analysis," *Int. J. Numer Meth. Eng.* **35**, 1737–1751.

Mammoli, A. A. and Ingber, M. S. [1999] "Stokes flow around cylinders in a bounded two-dimensional domain using multipole-accelerated boundary element methods," *Int. J. Numer Meth. Eng.* **44**, 897–917.

Mantič, V. [1993] "A new formula for the C-matrix in the somigliana identity," *J. Elasticity* **33**, 191–201.

Martin, P. A. and Rizzo, F. J. [1996] "Hypersingular integrals: How smooth must the density be?" *Int. J. Numer Meth. Eng.* **39**, 687–704.

Martin, P. A., Rizzo, F. J. and Cruse, T. A. [1998] "Smoothness relaxation strategies for singular and hypersingular integral equations," *Int. J. Numer Meth. Eng.* **42**, 885–906.

Monaghan, J. J. [1982] "Why particle methods work," *SIAM J. Sci. Stat. Comput.* **3**, 422–433.

Monaghan, J. J. [1988] "An introduction to SPH," *Comput. Physics Comm.* **48**, 89–96.

Monaghan, J. J. [1992] "Smooth particle hydrodynamics," *Annual Rev. Astro. Astrophys.* **30**, 543–574.

Most, T. and Bucher, C. [2005] "A moving least squares weighting function for the element-free Galerkin method that almost fullfills essential boundary conditions," *Struct. Eng. Mech.* **21**, 315–322.

Mukherjee, S. [1982] *Boundary Element Methods in Creep and Fracture* (Applied Science Publishers, London, UK).

Mukherjee, S. [2000] "Finite parts of singular and hypersingular integrals with irregular boundary source points," *Eng. Anal. Bound. Elem.* **24**, 767–776.

Mukherjee, Y. X. and Mukherjee, S. [1997a] "The boundary node method for potential problems," *Int. J. Numer Meth. Eng.* **40**, 797–815.

Mukherjee, Y. X. and Mukherjee, S. [1997b] "On boundary conditions in the element-free Galerkin method," *Comput. Mech.* **19**, 264–270.

Mukherjee, S. and Mukherjee, Y. X. [1998] "The hypersingular boundary contour method for three dimensional linear elasticity," *ASME J. Appl. Mech.* **65**, 300–309.

Mukherjee, Y. X. and Mukherjee, S. [2001] "Error analysis and adaptivity in three dimensional linear elasticity by the usual and hypersingular boundary contour method," *Int. J. Solids Struct.* **38**, 161–178.

Mukherjee, S. and Mukherjee, Y. X. [2005] *Boundary Methods — Elements, Contours and Nodes* (CRC Press, Taylor and Francis, Boca Raton, FL).

Mukherjee, S., Chati, M. K. and Shi, X. [2000b] "Evaluation of nearly singular integrals in boundary element, contour and node methods for three-dimensional linear elasticity," *Int. J. Solids Struct.* **37**, 7633–7654.

Mukherjee, Y. X., Mukherjee, S., Shi, X. and Nagarajan, A. [1997] "The boundary contour method for three-dimensional linear elasticity with a new quadratic boundary element," *Eng. Anal. Bound. Elem.* **20**, 35–44.

Mukherjee, S., Shi, X. and Mukherjee, Y. X. [1999] "Surface variables and their sensitivities in three-dimensional linear elasticity by the boundary contour method," *Comput. Meth. Appl. Mech. Eng.* **173**, 387–402.

Mukherjee, S., Shi, X. and Mukherjee, Y. X. [2000a] "Internal variables and their sensitivities in three-dimensional linear elasticity by the boundary contour method," *Comput. Meth. Appl. Mech. Eng.* **187**, 289–306.

Nabors, K. and White, J. [1991] "Fastcap: A multi-pole accelerated 3D capcacitance extraction program," *IEEE Trans. Comput. Aided Design* **10**, 1447–1459.

Nagarajan, A. and Mukherjee, S. [1993] "A mapping method for numerical evaluation of two-dimensional integrals with $1/r$ singularity," *Comput. Mech.* **12**, 19–26.

Nagarajan, A., Mukherjee, S. and Lutz, E. D. [1996] "The boundary contour method for three-dimensional linear elasticity," *ASME J. Appl. Mech.* **63**, 278–286.

Nayroles, B., Touzot, G. and Villon, P. [1992] "Generalizing the finite element method: Diffuse approximation and diffuse elements," *Comput. Mech.* **10**, 307–318.

Nishimura, N. [2002] "Fast multipole accelerated boundary integral equation methods," *Appl. Mech. Rev.* **55**, 299–324.

Nishimura, N., Yoshida, K. and Kobayashi, S. [1999] "A fast multipole boundary integral equation method for crack problems in 3D," *Eng. Anal. Bound. Elem.* **23**, 97–105.

Oden, J. T., Duarte, C. A. M. and Zienkiewicz, O. C. [1998] "A new cloud based *hp* finite element method," *Comput. Meth. Appl. Mech. Eng.* **153**, 117–126.

París, F. and Cañas, J. [1997] *Boundary Element Methods*: *Fundamentals and Applications* (Oxford University Press, Oxford, UK).

Peirce, A. P. and Napier, J. A. L. [1995] "A spectral multipole method for efficient solution of large-scale boundary element models in elastostatics," *Int. J. Numer Meth. Eng.* **38**, 4009–4034.

Phan, A.-V., Mukherjee, S. and Mayer, J. R. R. [1998] "The hypersingular boundary contour method for two-dimensional linear elasticity," *Acta Mech.* **130**, 209–225.

Rizzo, F. J. [1967] "An integral equation approach to boundary value problems of classical elastostatics," *Quart. Appl. Math.* **25**, 83–95.

Rokhlin, V. [1985] "Rapid solution of integral equations of classical potential theory," *J. Comput. Phys.* **60**, 187–207.

Roman, M. and Aubry, N. [2003] "Design and fabrication of electrostatically actuated synthetic microjets," *AMD ASME* **259**, 517–524.

Saad, Y. and Schultz, M. H. [1986] "GMRES: A generalized minimal residual algorithm for solving nonsymmetric linear systems," *SIAM J. Sci. Stat. Comput.* **7**, 856–869.

Schenck, H. A. [1968] "Improved integral formulation for acoustic radiation problems," *J. Acoust. Soc. America* **44**, 41–58.

Senturia, S. D., Harris, R. M., Johnson, B. P., Kim, S., Nabors, K., Shulman, M. A. and White, J. K. [1992] "A computer aided design system for microelectromechanical systems (MEMCAD)," *J. Microelectromech. Syst.* **1**, 3–13.

Seybert, A. F., Soenarko, B., Rizzo, F. J. and Shippy, D. J. [1985] "An advanced computational method for radiation and scattering of acoustic waves in three dimensions," *J. Acoust. Soc. America* **77**, 362–368.

Shen, L. and Liu, Y. J. [2007a] "An adaptive fast multipole boundary element method for three-dimensional potential problems," *Comput. Mech.* **39**, 681–691.

Shen, L. and Liu, Y. J. [2007b] "An adaptive fast multipole boundary element method for three-dimensional acoustic wave problems based on the Burton-Miller formulation," *Comput. Mech.* **40**, 461–472.

Shi, F., Ramesh, P. and Mukherjee, S. [1995] "Simulation methods for micro-electro-mechanical structures (MEMS) with applications to microtweezer," *Comput. Struct.* **56**, 769–783.

Shi, F., Ramesh, P. and Mukherjee, S. [1996] "Dynamic analysis of micro-electro-mechanical systems," *Int. J. Numer Meth. Eng.* **39**, 4119–4139.

Sladek, J., Sladek, V. and Atluri, S. N. [2000] "Local boundary integral equation (LBIE) method for solving problems of elasticity with nonhomogeneous material properties," *Comp. Mech.* **24**, 456–462.

Strouboulis, T., Babuška, I. and Copps, K. [2000] "The design and analysis of the generalized finite element method," *Comput. Meth. Appl. Mech. Eng.* **181**, 43–69.

Sukumar, N., Möes, N., Moran, B. and Belytschko, T. [2000] "Extended finite element method for three-dimensional crack modeling," *Int. J. Numer Meth. Eng.* **48**, 1549–1570.

Sukumar, N., Moran, B., Semenov, A. Y. and Belytschko, T. [2001] "Natural neighbour Galerkin methods," *Int. J. Numer Meth. Eng.* **50**, 1–27.

Sutradhar, A., Paulinio, G. H. and Gray, L. J. [2008] *Symmetric Galerkin Boundary Element Method* (Springer-Verlag, Berlin, Germany).

Telukunta, S. and Mukherjee, S. [2004] "An extended boundary node method for modeling normal derivative discontinuities in potential theory across edges and corners," *Eng. Anal. Bound. Elem.* **28**, 1099–1110.

Telukunta, S. and Mukherjee, S. [2005] "The extended boundary node method for three-dimensional potential theory," *Comput. Struct.* **83**, 1503–1514.

Timoshenko, S. P. and Goodier, J. N. [1970] *Theory of Elasticity*, 3rd edition (McGraw Hill, NY).

Yang, T. Y. [1986] *Finite Element Structural Analysis* (Prentice-Hall, Englewood Cliffs, NY).

Zhang, J. M., Yao, Z. H. and Li, H. [2002] "A hybrid boundary node method," *Int. J. Numer Meth. Eng.* **53**, 751–763.

Zhou, S. J., Cao, Z. Y. and Sun S. X. [1999] "The traction boundary contour method for linear elasticity," *Int. J. Numer Meth. Eng.* **46**, 1883–1895.

Zhu, T., Zhang, J. D. and Atluri, S. N. [1998] "A local boundary integral equation (LBIE) method in computational mechanics, and a meshless discretization approach," *Comput. Mech.* **21**, 223–235.

Zienkiewicz, O. C. and Taylor, R. L. [1994] *The Finite Element Method*, Vols. 1, 2, 4th edition (McGraw Hill, Berkshire, UK).